SCUOLA DI DOTTORATO
UNIVERSITÀ DEGLI STUDI DI MILANO-BICOCCA

Dipartimento di / Department of

FISICA G. Occhialini

Dottorato di Ricerca in / PhD program Fisica e Astrofisica Ciclo / Cycle XXX
Curriculum in (se presente / if it is) Fisica sperimentale

TITOLO TESI / THESIS TITLE

Search for anomalous production of high energy photon events with the CMS
detector at the LHC and prospects for HL-LHC

Cognome / Surname Pigazzini Nome / Name Simone

Matricola / Registration number 726826

Tutore / Tutor: Prof. Tommaso Tabarelli di Fatis

Cotutore / Co-tutor:
(se presente / if there is one)

Supervisor:
(se presente / if there is one)

Coordinatore / Coordinator: Prof. Marta Calvi

ANNO ACCADEMICO / ACADEMIC YEAR

2016/2017

Abstract

Although the Standard Model of particle physics (SM) describes with extreme success the fundamental interactions of matter it does not provide a solution for open questions of modern physics. The nature of cosmological dark matter, a quantum description of gravity and the hierarchy problem cannot included in the framework of the SM.

For this reason several extensions have been proposed throughout the years to address these open problems. The beyond the standard model (BSM) frameworks often predict the existence of additional particles, either arising from additional symmetries introduced by the model or by the inclusion of gravity. Part of the parameter space of these models can be covered by experiments at LHC, since the predicted particles can have masses in the TeV range.

The diphoton resonant production is sensitive to spin-0 and spin-2 BSM resonances. These can be originated by wrapped extra dimensions or extension of the Higgs sector which are typically included in BSM models. The excellent energy resolution achieved with the CMS electromagnetic calorimeter (ECAL) and the clean signature of the diphoton events makes this channel very attractive as a tool for the search of exotic resonances. The sensitivity of the search in the diphoton channel is subordinated to the ECAL energy resolution and the precision on the location of the interaction vertex. The search presented in this work has been conducted on data collected by the CMS experiment at LHC with proton-proton collisions at a center-of-mass energy of 13 TeV, for a total integrated luminosity of 35.9fb^{-1}. No significant deviation from the Standard Model prediction has been highlighted by the analysis, thus exclusion limits on the graviton production cross-section have been established in the context of the Randall-Sundrum extra dimensions model. The limits varies between 6 fb and 0.1 fb depending on the mass and coupling of the resonance in the $0.5 < m < 4.5$ TeV and $0.01 < \kappa < 0.2$ ranges.

The LHC program foresees an high luminosity phase starting from 2026 (HL-LHC), during which the instantaneous luminosity will reach the record value of 7.5×10^{34}cm^{-2}s^{-1}, five times the current one. On one hand higher instantaneous luminosity will bring benefits to the physics analysis by providing a dataset 10 times larger than what will be available during the LHC phase but, on the other hand will pose severe challenges to the event reconstruction given the high number of overlapping collisions. CMS is already planning various actions and detector upgrades to match the physics goal of HL-LHC. Among those the introduction of time into the event reconstruction will require the installation of a completely new detector. Technologies suitable for the measurement of charged particles time with a precision of 30 ps have been identified through a series of tests with particles beam. In the same tests the intrinsic time resolution of the ECAL has been proved to be better than 20 ps for electrons and photons of at least 25 GeV. The R&D campaign has been coupled to simulation studies to quantify the expected gain in performance provided by a time-aware event reconstruction. The simulation studies show a general improvement for observable of interest for the HL-LHC physics program.

Contents

Chapter 1

Introduction

This thesis revolves around measurements involving a two photon final state. The diphoton decay channel has been one of the two decay modes that led to the first observation of the Higgs boson [1]. The same final state provides a probe to test models describing new physics such as quantum gravity effective theories based on extra dimensions or Super Symmetry (SUSY) models with an extended Higgs sector. The nature of the photon restricts the particles that can decay to a two photon system to bosons with either spin equal to zero or spin strictly greater than one [2, 3]. A search for beyond the standard model (BSM) resonances, performed with p-p collision data collected by the CMS experiment, is presented in Chapter 4 together with the description of the calibration procedure (Chapter 3) of the detector component that contributes the most to the detection of photons in CMS (i.e. the electromagnetic calorimeter).

Measurements involving a diphoton system in the final state also include the measurement of the Higgs boson self coupling through di-Higgs production in p-p collisions. This standard model process is extremely rare, thus its observation is only possible with a large (thousands of fb^{-1}) dataset of p-p collisions. Such dataset will be produced during the high luminosity phase of LHC (HL-LHC), in Chapter 5 the major goals and challenges of the HL-LHC are described together with the preliminary studies to incorporate the time information into the event reconstruction of CMS as a way to meet the performance needed to fully exploit data collected in the high luminosity phase.

In the following sections the theoretical framework of fundamental interactions is briefly introduced. The main focus is to describe the standard model, the phenomenology of hadronic collisions and the models which gives rise to a BSM resonant diphoton production.

1.1 The standard model of particle physics

During the 20th century the development of new technologies enabled experimental physicists to explore matter at the atomic and sub-atomic levels. At these levels is possible to explore the building blocks of matter and the interactions between them.

A theory has been constructed during the past century which describes and predicts a large part of the natural processes that are know today. The Standard Model of particle physics (SM) describes in coherent way three types of interactions between sub-atomic particles: the behavior of electromagnetic, weak and strong interaction at a quantum level is addressed by the SM. The SM in fact allows us to describe a variety of phenomena with a single mathematical framework.

The SM is build upon a relativistic quantum field theory. The constituents of matter are particles with half-integer spin that follow the Fermi-Dirac statistic while the interactions are mediated by integer spin particles which follow Bose-Einstein statistic. It is common to refer at the first group as fermions and to the second as bosons. Tables 1.1 and 1.2 show the fermions and bosons described by the SM and their main properties.

	1^{st} gen.		2^{nd} gen.		3^{rd} gen.		Q	Colour Charge
leptons	ν_e	~ 0	ν_μ	~ 0	ν_τ	~ 0	0	0
	e	511keV/c^2	μ	105.7MeV/c^2	τ	1.777GeV/c^2	-1	0
quarks	u	$1.7 - 3.1\text{MeV/c}^2$	c	$1.29^{+0.05}_{-0.11}\text{GeV/c}^2$	t	$172.9^{+1.1}_{-1.1}\text{GeV/c}^2$	2/3	r, g, b
	d	$4.1 - 5.7\text{MeV/c}^2$	s	$100^{+30}_{-20}\text{MeV/c}^2$	b	$4.19^{+0.18}_{-0.06}\text{GeV/c}^2$	-1/3	r, g, b

Table 1.1: Spin-$\frac{1}{2}$ fermions masses, electric charges (in units of the positron charge) and color charges [4].

	Mass (GeV)	Q	Colour Charge
Photon (γ)	0	0	0
Gluon (g)	0	0	r, g, b
W	80.385 ± 0.015	± 1	0
Z^0	91.188 ± 0.002	0	0

Table 1.2: Spin-1 bosons masses and charges [4].

Fermions differ from each other by mass and coupling to the force carriers. A charge is associated to each interaction so a total of four values is used to identify a fermion: three charges and one mass. Fermions with non-null color charge are named quarks and interact strongly with each other through the exchange of gluons, the strong force carriers. The other fermions, called leptons, that are insensitive to the strong force interacts only electroweakly.

At the core of the SM there is the concept of gauge invariance. Since Maxwell's unification of electric and magnetic interactions, gauge invariance has played a strategic role in the description of the fundamental interaction of matter. The requirement of a symmetry in the Lagrangian of a theory accounts for invariance of charges, via the Noether's theorem. The mediators of the interaction are introduced to preserve the conservation of the free particle Lagrangian under the gauge transformation of the type $\psi \rightarrow e^{i\alpha}\psi$, where ψ is a generic fermion field.

In these terms the SM is based on a group of three symmetries $SU_C(3) \times SU_L(2) \times U_Y(1)$. The interactions between the particles described above arise from the request of local gauge invariance of the Lagrangian related to the three symmetries.

$SU_C(3)$ is related to the strong interaction mediated by massless gluons. It conserves the colour charge carried by quarks and gluons which appear as colour triplets under $SU_C(3)$ transformation. The experimental evidence is that coloured particles cannot propagate freely. Quarks and gluons are only observed in bound states as mesons $q\bar{q}$ and barions qqq. This behaviour is known as asymptotic freedom, i.e. the coupling is asymptotically weaker as energy increases and distance decreases and conversely it becomes stronger at larger distances.

The $SU(2)_L \times U(1)_Y$ group is associated to electroweak interactions, which allows a

unified description of electromagnetism and weak interactions. The long-range electromagnetic interaction is mediated by the massless photon (A_μ field), while the short-range weak force carriers are the massive W^+, W^- and Z^0 bosons. Unlike the gluons, the electroweak mediators are not the direct fields introduced to preserve the gauge invariance but instead are combinations of them. In particular the W^3_μ and B_μ introduced respectively for the $SU_L(2)$ and $U_Y(1)$ symmetries are mixed to obtain the physical A_μ and Z_μ fields:

$$W^\pm_\mu = \frac{1}{\sqrt{2}}\left(W^1_\mu \mp iW^2_\mu\right)$$
$$\begin{pmatrix} A_\mu \\ Z_\mu \end{pmatrix} = \begin{pmatrix} \cos\theta_W & \sin\theta_W \\ -\sin\theta_W & \cos\theta_W \end{pmatrix} \begin{pmatrix} B_\mu \\ W^3_\mu \end{pmatrix} \quad ,$$

where Weinberg mixing angle (θ_W) has been measured at the Z-pole at LEP as $sin^2(\theta_W) = 0.23153 \pm 0.00016$.

The mixing is also reflected in the conserved charges for which the following relation holds:

$$Q = T_3 + \frac{Y}{2}$$

where Q is the electric charge, Y the $U_Y(1)$ hypercharge and T_3 is the third component of the weak isospin T conserved by the $SU_L(2)$ symmetry.

The $W^\pm$ bosons couple only to the left-handed components ψ_L of the fermion fields, while the Z^0 and γ bosons couple to both ψ_L and ψ_R, thus leading to the observed parity-violation phenomena of weak interactions. The asymmetry between right and left handed fermions also forbids the inclusion of a Yukawa mass terms into the standard model Lagrangian since such a term would not be invariant under $SU_L(2)$ transformation. This fact has a remarkable consequence: the three generations of leptons and quarks summarized in Table 1.1 are identical from the perspective of the strong and electroweak interactions since they only differ for their masses. Table 1.3 summarizes the charges for all known fermions families:

	T	T_3	Y	Q		T	T_3	Y	Q
l_L	1/2	−1/2	−1	−1	q^{down}_L	1/2	−1/2	1/3	−1/3
ν^l_L	1/2	1/2	−1	0	q^{up}_L	1/2	1/2	1/3	2/3
l_R	0	0	−2	−1	q^{down}_R	0	0	4/3	2/3
ν^l_R	0	0	0	0	q^{up}_R	0	0	−2/3	−1/3

Table 1.3: Charges (quantum numbers) of leptons (left) quarks (right).

Notably the right-handed neutrino is sterile in the standard model, i.e. it does not couple to any of the three forces carriers.

Bosons and fermions in the theory outlined above are all massless. This is in evident contradiction with the observation of masses that vary across several orders of magnitude from the almost massless neutrinos to the heaviest quark. The spontaneous electroweak symmetry breaking mechanism (EWSB) of a local gauge symmetry was proposed to solve this issue by Englert, Brout [5], Higgs [6] and others and it is shortly outlined in the following. It can be applied to any renormalizable quantum field theory, such as the Standard Model. The mass of the gauge bosons can be generated by a scalar field. The

chosen doublet of complex scalar fields ($SU_L(2)$) is of the form:

$$\phi = \frac{1}{\sqrt{2}} \begin{bmatrix} \sqrt{2}\phi^+ \\ \phi^0 + ia^0 \end{bmatrix}$$

with ϕ^0 and a^0 being the CP-even and CP-odd neutral components, and ϕ^+ being the complex charged component of the Higgs doublet. The standard model Lagrangian is extended with to include the so-called Higgs scalar potential:

$$V(\phi) = \mu^2\phi^\dagger\phi + \frac{\lambda}{2}(\phi^\dagger\phi)^2$$

with the real parameter μ^2 and quartic coupling λ, the Higgs self-coupling parameter. The electroweak symmetry is then said to be spontaneously broken as the SM Lagrangian stays invariant under the symmetry, but the ground state $< \phi >= \frac{1}{\sqrt{2}} \begin{bmatrix} 0 \\ \nu \end{bmatrix}$ of the Higgs potential does not. With $\nu = \frac{\sqrt{2}|\mu|}{\lambda}$ being the vacuum expectation value, its value is a parameter of the model and, although it cannot be directly measured, is constrained to to be $\sim$ 246 GeV [4] by measurements of SM observables (i.e. the W boson mass, the Fermi constant and the week isospin coupling). Gauge bosons acquire mass through the spontaneous symmetry breaking mechanism while for fermions the mass derives from Yukawa interaction with the Higgs scalar field. The mass of the Higgs boson is a free parameter of the theory and was measured experimentally by ATLAS and CMS to be $m_H = \lambda \cdot \nu = 125.09 \pm 0.21(stat) \pm 0.11(syst)$ GeV [4]. Till now all the measured properties (spin and couplings) do not show any significant discrepancy with respect to the standard model prediction.

The standard model described above has proven over the years to be remarkably accurate in describing and predicting the interaction of matter at the quantum level. However there is a number of processes observed in Nature that cannot be explained by the otherwise complete model:

- Cosmological dark matter.
- Matter-antimatter asymmetry.
- Neutrinos oscillations and masses.

To name some of them. Furthermore the SM lacks a quantum description of gravity and also requires a "fine tuning" (more later) of some of its parameters.

These issues are addressed by several models extending the SM, most of them predicts the existence of new particles (arising from the same gauge invariance request explained above) that could be observed either through the products of their decay or from virtual interference with standard model interactions. In both cases hadronic collision offers a unique way to test such models providing both the possibility to produce them or infer their existence from precise measurement of the standard model parameters.

1.2 Proton-proton collisions

The precise measurement of the electroweak sector at the LEP and SLC electron-positron colliders and the discovery of the top quark at Tevatron proton-antiproton collider, the yet to be observed Higgs boson and the search for BSM physics led to the construction of the Large Hadron Collider (LHC).

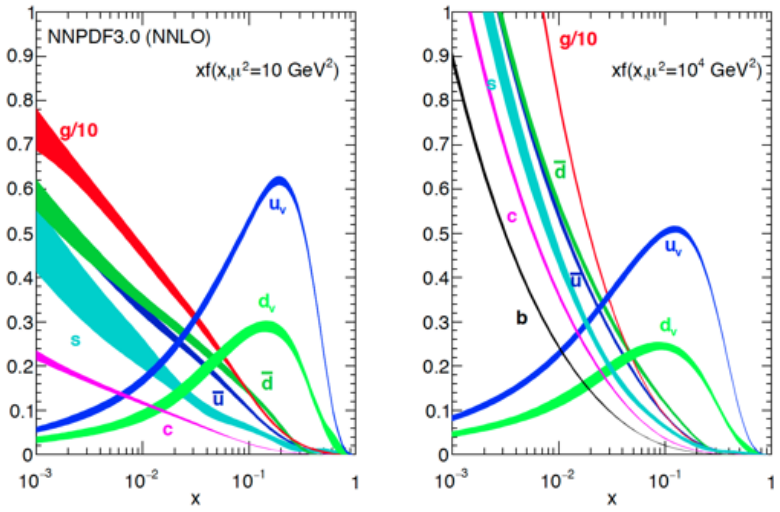

Figure 1.1: Distributions of x-times the unpolarized parton distribution function $f(x)$ obtained in the NNPDF 3.0 global analysis at the scales of $\mu^2 = 10\text{GeV}^2$ (left) and 10^4GeV^2 (right) at $\alpha_s(M_Z) = 0.118$ [11].

Hadron colliders, in the context of high energy physics, are great tools for discoveries since protons are composite particles and thus both the hard scattering energy and its nature are not restricted by the machine parameters but covers a wide range of possibilities. The inner structure of the proton has been extensively studied in recent years at the electron-proton collider HERA at DESY [7]. The proton, as all other barions, is made of three "valence" quarks surrounded by a "sea" of gluons and quark-antiquark pairs. Quarks and gluons in this context are referred to as partons. This qualitative description is translated into a quantitative description by the DGLAP equations using perturbative quantum chromodinamics (QCD) [8, 9, 10]. The probability to find a parton carrying a fraction "x" of the total proton momentum is described by the parton density functions (PDFs). As shown in Figure 1.1 the valence quark dominates over the sea partons for $x > 0.1$. The PDFs depend on the momentum transferred in the scattering process, in particular for larger values of momentum transfer μ^2 the gluon PDFs dominates over the valence quark. For this reason "gluon-fusion" initiated processes dominate at LHC.

The perturbative QCD well describes the hard part of the hadronic collisions and the emission of energetic quark and gluons as initial and final state radiation, while the description of the formation of bounded QCD states from bare quark and gluons involves non-perturbative, low μ^2 processes generally called "hadronization".

The hadronization of quarks and gluons coming from high μ^2 processes (hard scattering) gives rise to a jet of collimated hadrons , which are usually reconstructed in collider experiments as energy clusters. The kinematic of a jet is directly linked to the one of the original quark or gluon, allowing the reconstruction of the hard scattering.

An hard scattering usually only involves a parton from each colliding proton, the other partons interact at low μ^2 (soft interactions) giving rise to the so called "underlying event" i.e. particles of low transverse momentum produced in conjunction with the boosted products of the hard interaction.

1.3 Extra dimensions and the hierarchy problem

The hierarchy problem is a common way to, within the high energy physics community, refer to the large discrepancy arising between the effective value of a constant and the fundamental value it has in the Lagrangian that describes the dynamics of the model under consideration

An example in SM is given by higher order corrections to the Higgs boson mass. These includes loops of massive particles which for one fermion give a correction expressed as:

$$\Delta m_H^2 = \frac{\lambda_f^2}{4\pi^2}(\Lambda^2 + ...)$$

If one imposes a cutoff at a scale Λ close to the Planck mass ($M_{Pl} \sim 10^{19}$GeV) a cancellation of the radiative correction for this fermion loops occurs for $(m_H/\Lambda)^2 \sim 10^{-34}$ (here m_H the fundamental Higgs boson mass equal to the vacuum expectation value for the Higgs field and ΔM_H represent the correction that gives the observed Higgs boson mass).

Is evident that such a small value of $(m_H/\Lambda)^2$ represents a "fine-tuning" of the theory which otherwise would give rise to an incredibly huge Higgs boson mass (compared to all other particles in the standard model). The "fine-tuning" cannot be explained within the framework of the SM alone, however extra dimension models offer a solution to this fine tuning.

Extra dimension models (ED) were introduced by Kaluza-Klein [12] in attempt to unify the electromagnetism with the description of gravity given by Einstein's general relativity. The general idea is the existence of a multidimensional space-time with at least 4 space dimensions and one time dimension. This space-time is an extension of the four-dimensional Minkowsky space and the weakness of the gravity interaction is explained by its propagation through the extra dimensions.

Extra dimensions as solution for the hierarchy problems was first proposed by Arkani, Dimopoulos and Dvali (thus the name ADD model) [13]. The existence of n additional spatial dimensions, compactified with average radius R, produces an effective Planck mass in our four-dimensional world that is related to the true Planck Mass by: $M_{Pl}^2 \sim M_{Pl(4_n)}^{n+2} R^n$. It is therefore possible, with appropriate values for n and R, that the true value of the Planck scale ($M_{Pl(4_n)}$) could be on the order of the electroweak scale, thus solving the SM hierarchy problem, while still producing the much larger apparent Planck scale that we observe in our four-dimensional world.

Randall and Sundrum (RS) proposed an alternative model [14], with just one additional dimension that has a warped geometry, described by curvature parameter k. The extra dimension y is wrapped, meaning that it is curled up to a circle with a finite radius r_c and curvature parameter k. The five-dimensional space-time metric is given by:

$$ds^2 = e^{-2ky}\eta_{\mu\nu}dx^\mu dx^\nu + d^2y \tag{1.1}$$

Imposing the boundary conditions of $y = 0$ and $|y| = \pi r_c = L$. The two boundary conditions determine the warp factor of Equation 1.3:

$$\frac{e^{-k|y(L)|}}{e^{-k|y(0)|}} = e^{-2kr_c}$$

The RS model in contrast to ADD one only requires one extra dimension with $r_c \sim 15$ to solve the hierarchy problem thanks to the wrapped geometry of the extra dimension.

1.4 Extra dimension signatures in proton-proton collisions

In both the ADD and RS models the perturbative KK expansion of the five-dimensional metric gives origin to an infinite number of four-dimensional spin-2 fields (gravitons). Together with the massless spin-2 boson associated to gravity an infinite number of massive gravitons are predicted to exist at masses that are of the order of the TeV. In the ADD model the four-dimensional massive states are closely spaced and thus produce a degenerate spectrum when they decay into SM particles. RS model instead predicts the existence of well separated mass states of which only the first one has a mass within the energy reach of LHC.

The RS-like models can be further categorized depending on how much the SM fields propagates into the five-dimensional space-time. In the "bulk" scenario the SM fields propagates in the five-dimensional space as the graviton field does while in the RS1 they are confined to the four-dimensional world. In the bulk scenario the gravitons coupling to SM particles is proportional to the mass of the SM particle, for this reason the primary search channel are final states with two gauge or Higgs bosons (Figure 1.2, left). In the RS1 scenario instead the branching ratio for the decay into a photon pair is comparable to those to the gauge bosons, jets and leptons (Figure 1.2, right). The clear signatures of a final state with two photons and the excellent energy resolution of the electromagnetic calorimeters of the LHC experiments makes the decay to two photons an interesting search channel for RS1 gravitons. The search described in Chapter 4 thus focus on the RS1 model graviton.

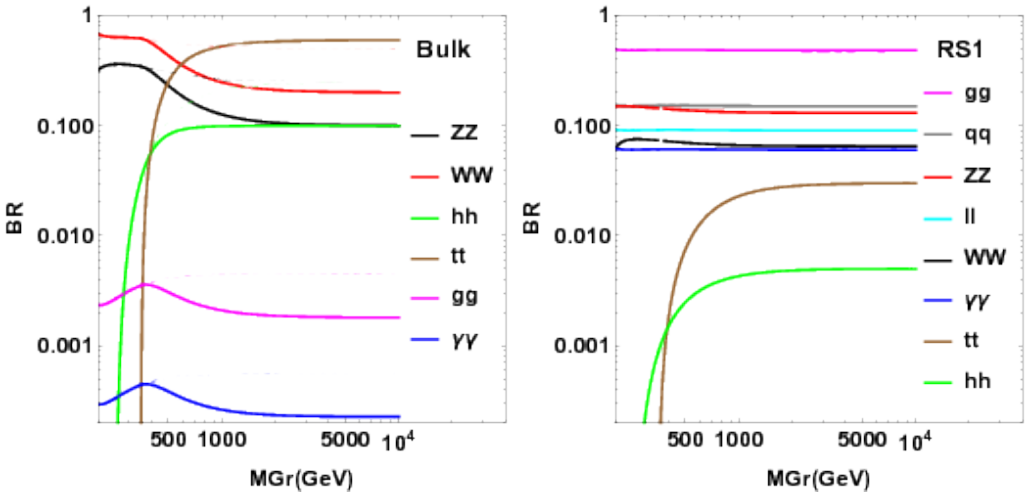

Figure 1.2: KK graviton branching fractions. Left: Bulk scenario. Right RS1 scenario. The symbol q stands for the sum of light quarks (u,d,s,c,b), while l represents the sum of the three flavors of leptons (e,μ,τ) or neutrinos [15].

Several searches have been performed at collider experiments searching for both ADD and RS like graviton production. At Tevatron the CDF and D0 experiment graviton masses up to 500 GeV[16, 17] were excluded. The 95% exclusion limits were extended to the TeV range by ATLAS and CMS already with data from 8 TeV LHC collisions [18, 19].

The diphoton final state is also sensitive to spin-0 resonances such as those predicted by SUSY models. SUSY models introduce an additional symmetry to explain the large difference between the electroweak and planck scales, this leads to the prediction of the existence to a partner to each of the known SM particles and also to an extend Higgs

sector. A popular model is the so called two-Higgs-Doublet-Model (2HDM) [20, 21], this was chosen as benchmark for spin-0 signal in the search for diphoton resonances.

1.5 Standard model diphoton production

The main background for the search of BSM resonances decaying to two photons is the standard model production of photon pairs. Photon pairs production is possible through leading order processes involving two initial state quarks $q\bar{q} \to \gamma\gamma$ (Figure 1.3). Higher order terms in perturbative QCD also contribute to the total production cross section as well as final state quark fragmentation, the corresponding Feynman diagrams are illustrated in Figure 1.4. Given the importance of gluon initiated processes at LHC the "box" diagram diphoton production through gluon-fusion also has a large contribution in the SM diphoton production (Figure 1.5).

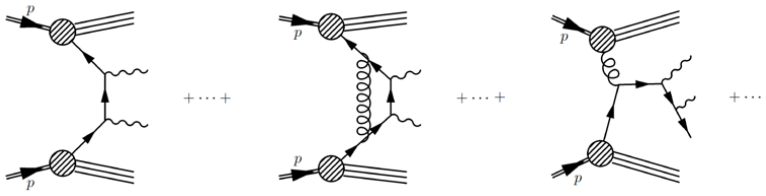

Figure 1.3: Feynman diagrams of the diphoton production processes, with the LO Born process $q\bar{q} \to \gamma\gamma$ (left), and the NLO contributions $q\bar{q} \to \gamma\gamma$ (middle) and $q\bar{q} \to \gamma\gamma q$ (right) and associated virtual corrections [22].

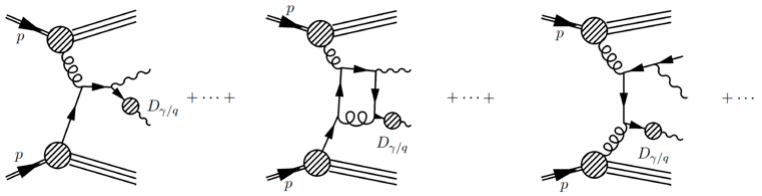

Figure 1.4: Examples of diphoton production processes with one photon being produced via quark fragmentation [22]

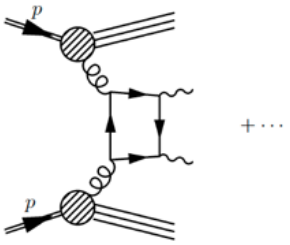

Figure 1.5: Feynman diagram of the NNLO 'Box' diphoton production process [22].

Chapter 2

The LHC complex and the CMS detector

In this Chapter a brief description of the Large Hadron Collider and of the CMS detector are presented in order to contextualize the physics analyses that are described in the following chapters. In particular, the CMS subdectors are described, since they are fundamental for the reconstruction of particles, such as photons and products of partons hadronization.

2.1 The Large Hadron Collider

The Large Hadron Collider (LHC) is the largest and most energetic collider machine ever built to study matter at the subatomic scale. It is operated by CERN and is located at the boarder between France and Switzerland close to Geneve. It collides protons up to a center of mass energy of 13 TeV.

The LHC is located underground ($\sim$ 100 m below the surface) and has a total length of about 27 km. The tunnel that houses the LHC was previously occupied by the Large proton electron collider (LEP) that played a crucial role in investigating the properties of the Z and W bosons.

The primary goal of LHC has been to study the electroweak simmetry breaking through first search for the Higgs boson and the later precision measurements of the its properties. The energies explored by the collisions at LHC allow to probe the standard model up to scales of few TeV where interactions not described by the SM could be observed in various production and decay processes. The same machine is also used to accelerate and collide protons with ions or ions with ions.

The design of the LHC aims to reach a center of mass energy of 14 TeV and an istantaneous luminosity ($\mathcal{L}$) of $10^{34} cm^{-2} s^{-1}$ for $p-p$ collisions. The scientific program span several decades, in the current phase it will deliver to the experiments about $300\,\mathrm{fb}^{-1}$ of integrated luminosity by 2023, while it will reach $3000\,\mathrm{fb}^{-1}$ during the dacade starting in 2026 (Figure 2.1).

2.2 LHC properties

The high beam intensities necessary for reaching the design luminosity makes the use of two separate proton beams necessary. The collision of two beams of equally charged particles requires opposite magnet dipole fields in both beams. The LHC is therefore

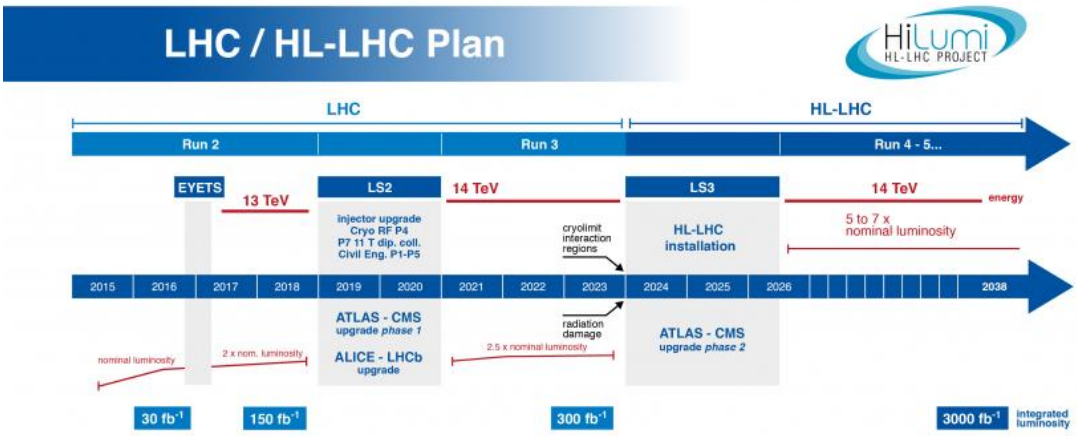

Figure 2.1: Illustration of the foreseen LHC schedule, the current phase ends with long shutdown 3 (LS3). The high luminosity phase (HL-LHC) starts after LS3 and will last for a decade. LHC standard operation includes running periods during spring, summer and fall and a technical stop for small upgrades and mantainance during winter. Larger upgrades are carried out during long shutdowns (LS), a major one will be the upgrade of the LHC and of the experiments during LS3.

designed as a proton-proton collider with separate magnet fields and vacuum chambers in the main arcs, with common sections only at the insertion regions where the experiments are located. The choice to reach at regime centre of mass energies of 14 TeV has forced to have a mag- netic field of ~ 8.3 T, requiring 1232 liquid Helium cooled superconducting magnets made of a Niobium-Titanium compound at a temperature of 1.9 K, by means of super-fluid Helium. Figure 2.2 shows all the acceleration steps the particles have to perform in order to reach 14 TeV energies.

To reach the nominal luminosity, up to 2808 bunches per beam, with about 1.1×10^{11} protons each, are collided every 25 ns. On the LHC ring four main experiments are located: ATLAS [23], CMS [24], LHCb [25] and ALICE [26]. CMS and ATLAS are general purpose experiments, with complementary features and detector choices. CMS is described in detail in the next sections. The LHCb collaboration aim to perform precision measurements on CP violation and rare decays of B-mesons, in order to reveal possible indications for new physics phenomena. ALICE is dedicated to heavy ions physics and the goal of the experiment is the investigation of the behaviour of the strongly interacting hadronic matter resulting from high energy lead nuclei collisions. In those extreme energy densities the formation of a new phase of matter, the quark-gluon plasma, is expected.

The LHC cycle consists of several phases: the machine is filled with protons while the energy is kept at 450 GeV, once the machine is full the beams are accelerated, squeezed and set on colliding orbits. The instantaneous luminosity is maximized in ATLAS and CMS while in ALICE and LHCb it is kept at lower values. Each cycle is called a “fill”.

2.3 The CMS experiment

The CMS experiment is a general purpose detector for particle physics. The detector includes several subsystems symmetrically centered around the fifth interaction point of LHC. The detector is 22 m long and 15 m wide and is depicted in Figure 2.3. It consists

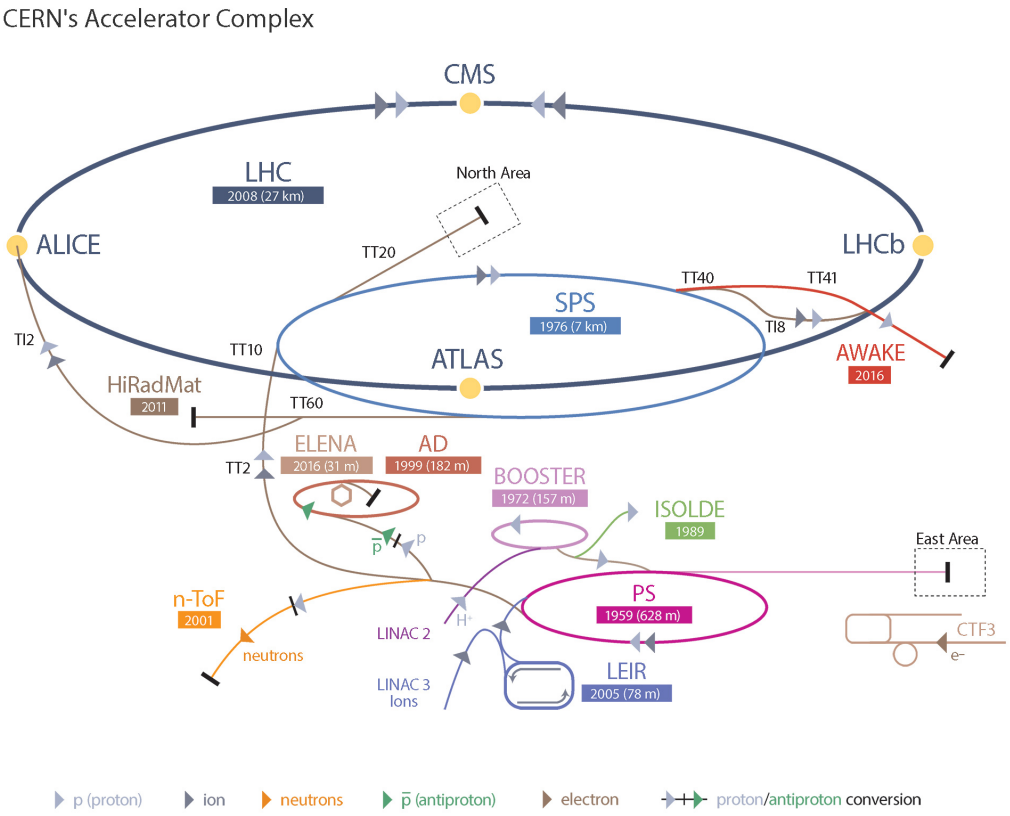

Figure 2.2: The CERN accelerators complex. Protons are first extracted from a hydrogen tank and accelerated up to 50 MeV by a linear accelerator (Linac 2). The Proton synchrotron booster (BOOSTER) and Proton synchrotron (PS) push the energy up to 1.4 GeV and 25 GeV respectively. Protons are then transfered to the Super proton synchrotron (SPS) where they are accelerated to 450 GeV and injected into the LHC. Others machines are present at CERN complex to provide dedicated beams to various experiments. Furthermore both from the PS and the SPS, the proton or ion beam is sent to a fixed target to provide secondary beams of pions, muons and electrons to several areas dedicated to fixed target experiments or R&D projects.

of a central part, "barrel", and two forward regions, the "endcaps", which detect particles at small deflection angles. The main detector component is the superconducting solenoid that generates a magnetic field of 3.8 T. The tracking and calorimeter systems are contained within the solenoid. This design benefits the particle reconstruction as it minimizes the probability for a particle to generate a shower before reaching the calorimeters while traversing the dense material of the solenoid. Most of the detector is supported by a steel skeleton which serves also as the return yoke for the magnetic field of 1.8 T present outside the solenoid volume. The muon detection system is placed outside the solenoid and inside the return yoke. The CMS detector has a weight of about 12500 tonnes, mainly due to the steel skeleton and the solenoid.

The origin of the right-handed coordinate system of CMS is the central collision point, with the z-axis oriented in the anticlockwise-beam direction. The x-axis is oriented towards the center of the LHC accelerator ring, the y-axis points upwards.

The azimuthal angle (ϕ) lies in the x-y plane and is measured from the x-axis. A

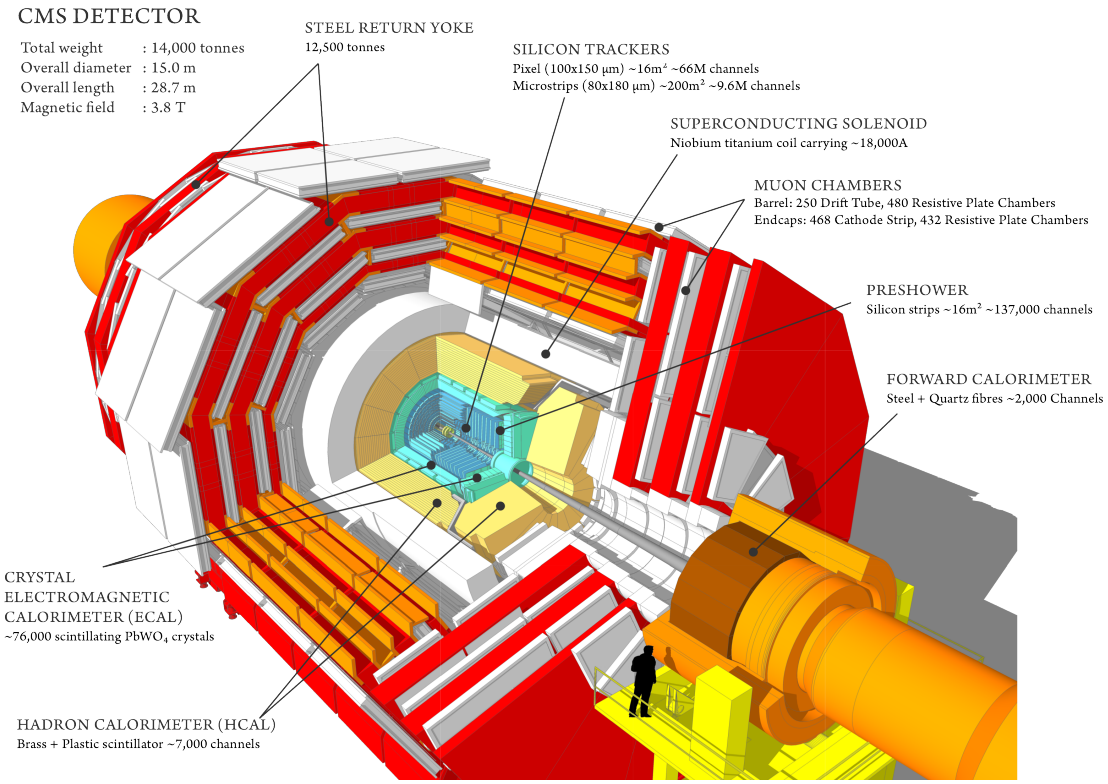

Figure 2.3: Sketch of the Compact Muon Solenoid detector [27].

slice of the CMS detector in this x-y plane is shown in Figure 2.4. The polar angle (θ) is directed upwards from the z-axis. With the polar angle, the pseudorapidity (η) can be defined:

$$\eta = -ln(tan(\frac{\theta}{2}))$$

The particle mass m, momentum in the transverse plane p_T and its η and ϕ rappresent a convinient set of variables to describe the particles produced in hadronic $p-p$ collisions where the fraction of momentum carried by each of the colliding parton is in principle unknown.

2.3.1 The tracking system

The tracking detector surrounds the beampipe, the innermost layer is installed about 4 cm from the interaction point (IP). It has a length of 5.8 m, a diameter of 2.6 m, and covers a range of $|\eta| < 2.5$ with an area of over 200 m^2 active silicon sensors, its layout is shown in Figure 2.5. It is designed to measure the trajectories of charged particles as highlighted in Figure 2.4. As such, it has to provide a high spatial resolution and a fast signal readout while withstanding a fluence of about 10^6 particles/(cm^2 s) (at a distance of 8 cm from the IP). The core of the tracking system, the silicon pixel detector, is made of 66 million pixels with a size of $100 \times 150 \mu m^2$, enabling the reconstruction of primary and secondary vertices with a precision that ranges between 100 μm to 1 mm in the z direction and of few tens of μm in the x and y directions. The silicon pixel detector is followed by a silicon strip detector with coarser granularity. The track recognition is

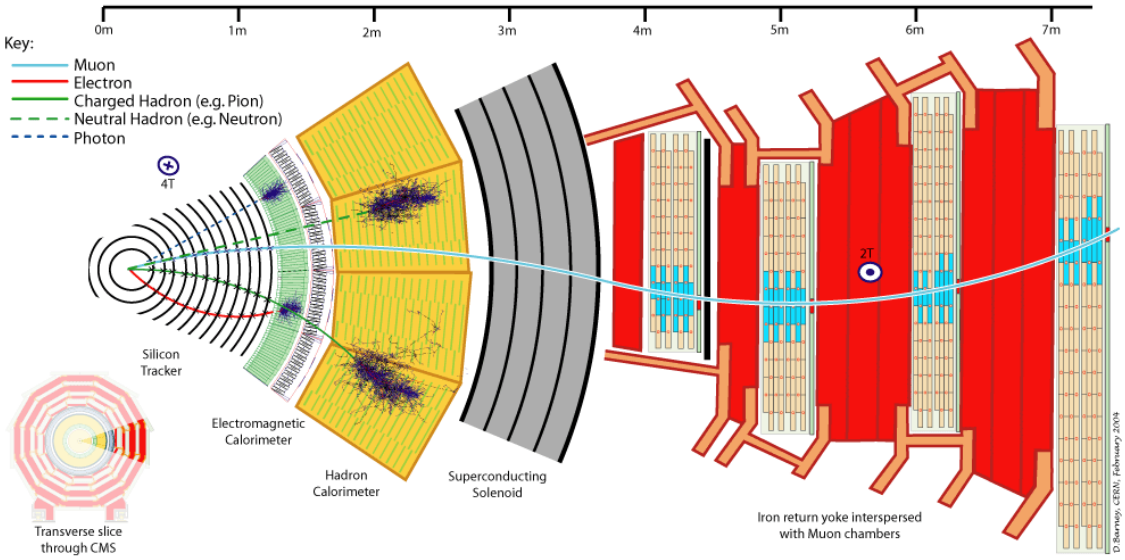

Figure 2.4: A slice of the CMS detector in the x-y plane. Various particle type detection are depicted, the details of each system are given in the text.

performed by about 15200 highly sensitive modules containing 10 million detector strips. The tracking detector has a radiation length (X_0) of 0.4 at $\eta = 0$, which increases at larger η to approximately 1.8 X_0 at $|\eta| = 1.4$ as visible from Figure 2.6.

2.3.2 The calorimeter system

The calorimeter system is divided in two sections: the electromagnetic part ECAL which measures the energy of electrons and photons and the hadronic part (HCAL) dedicated to the measurement of the energy of charged and neutral hadrons. The two detectors differ both in purpose and technology.

The ECAL is an homogeneous and hermetic calorimeter, made of scintillating lead tungstate crystals. The chosen crystal is suitable for operation at LHC due to its fast emission (80% of the scintillation light is emitted within 25 ns) and its resilience to irradiation. Moreover, thanks to crystal short radiation length ($X_0 = 0.89$ cm) and small Molière radius ($r_M = 21.9$ mm), most of an electron or photon energy can be collected within a matrix of 25 crystals.

As the other CMS sub-detectors the ECAL is divided in two main sections:

- Barrel (EB): it covers the region $|\eta| < 1.4442$ with 61200 crystals arranged in 170 rings of 360 crystals each.

- Endcap (EE): it covers the region $1.556 < |\eta| < 3.0$ with 14648 crystals arranged in 4 Dees of 3662 crystals each.

All the crystals are mounted with a tilt of 3°, both η and ϕ projections, in a quasi-projective geometry to avoid gaps aligned with the particles trajectories. The EB is located at $R = 1.3$ m from the IP while the endcaps are installed at $z = \pm 3.10$ m Figure 2.7. The crystal front face measures $22 \times 22\text{mm}^2$ corresponding to a $\Delta\eta \times \Delta\phi$ granularity of 0.0175×0.0175 in the barrel and outer endcap while it grows up to about 0.05×0.05 in the endcap regions closer to the beams.

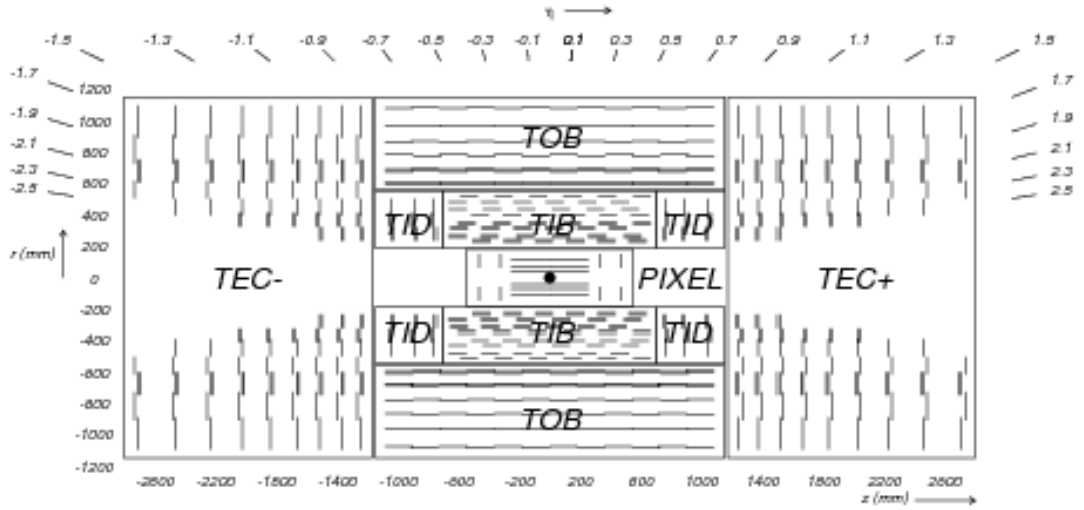

Figure 2.5: Schematic section of the CMS tracker in the r-z plane. Each line-element represents a detector module. Closely spaced double line-elements indicate back-to-back silicon strip modules, in which one module is rotated through a "stereo" angle, to permit the reconstruction of the hit positions in three dimensions. Within a given layer, each module is shifted slightly in r or z with respect to its neighbouring modules, which allows them to overlap, thereby avoiding gaps in the acceptance [28].

The relatively low light yield of $\sim 30\gamma$/MeV makes the use of intrinsic high-gain photodetectors necessary, capable of operating in an high magnetic field. Avalanche PhotoDiodes (APDs) are used to collect light in barrel crystals while Vacuum PhotoTriodes (VPTs) are used in the endcaps. Two APDs are glued on the crystals rear face and their signals are summed before reaching the front-end electronics. In the endcaps only one VPT is used for each crystal.

APDs have a gain of 50 at nominal operation bias voltage, while the relative gain variation due to changes in the bias voltage is of $\Delta G/\Delta V = 3.1\%/V$. The APDs gain also depends on temperatures as $\Delta G/\Delta T = -2.4\%/C^\circ$.

VPTs are more radiation resilient and thus were chosen as photodectors in the endcap regions but have a gain variation of about 25% across the endcaps.

ECAL operates at a temperature of 18 C° which is maintained by a dedicated cooling system. The temperature dependence of the crystal light yield (-2% C°) and of the APD gain demand a precise temperature stabilization at the level of 0.05 C° in the EB. In the endcaps, the dependence of the VPT response on the temperature is negligible, so a stabilization at the level of 0.1 C° is sufficient. These specifications limit the contribution of temperature variation to the constant term of the energy resolution to be less than 0.2%.

The ECAL system is complemented by a pre-shower (ES) placed in front of each of the ECAL endcaps. The ES is made of two layers of silicon strips with 1.9 mm pitch alternated with passive layers of lead radiators ($2X_0$ and $1X_0$) that extend from η 1.6 to 2.8. The ES is used to discriminate between collimated photons coming from decays of neutral hadrons and real photons. The performance of the ECAL are further discussed in Chapter 3.

The HCAL measures the energy of hadrons by stopping them within its hermetic vol-

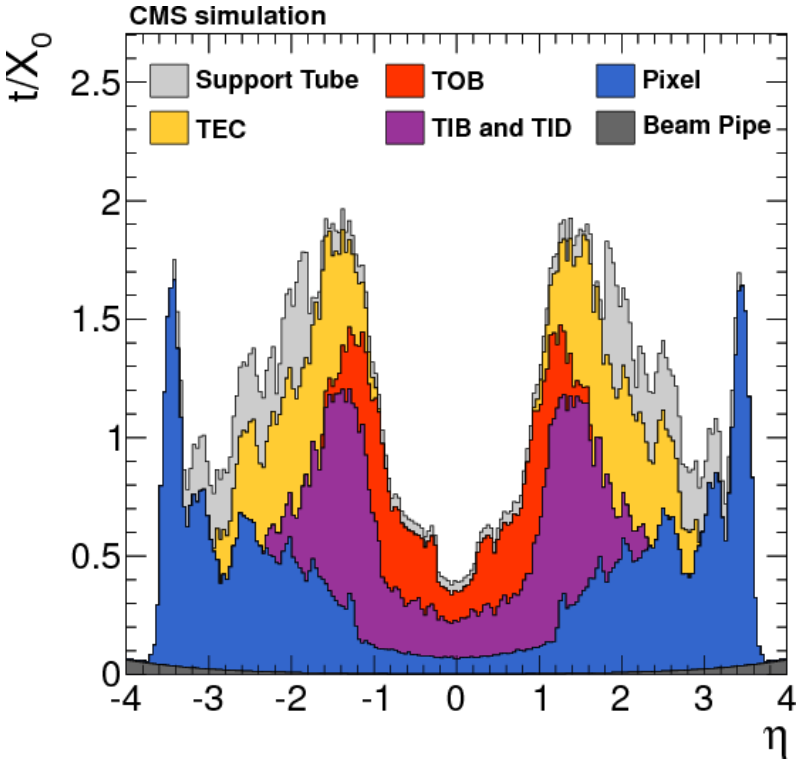

Figure 2.6: Total thickness t of the tracker material traversed by a particle produced at the nominal interaction point, as a function of pseudorapidity η, expressed in units of radiation length X_0. The contribution to the total material budget of each of the subsystems (Figure 2.5) that comprise the CMS tracker is shown, together with contributions from the beam pipe and from the support tube that surrounds the tracker [28]. The configuration shown in the picture reflects that of the CMS tracker prior the upgrade of the pixel detector in 2017, that significantly reduces the material budget in forward region.

ume and reading out the deposited energy. Its dimensions (Figure 2.8) are constrained by the ECAL ($R = 1.77$ m) and the surrounding magnet coil ($R = 2.95$ m). The chosen design is the one of a sampling calorimeter with brass absorbers and scintillating tiles for the energy measurement. The readout is performed via optical fibers by hybrid photodiodes.

The HCAL effective thickness increases with polar angle as $1/cos\theta$ in the barrel, it varies from 5.82 interaction length at $\eta = 0$ to 10.6 at $\eta = 1.3$ while it is costant at about 10 interaction length in the endcap regions. An additional small hadron calorimeter is placed behind the solenoid to capture very high energetic hadrons showers not contained with the inner calorimeters and the magnetic coil. This additional component of the HCAL is used to reduce the mis-identification of hadronic jets as muons. The granularity in the barrel region ($|\eta| < 1.3$) is $\Delta\eta \times \Delta\phi = 0.087 \times 0.087$, while in the endcap regions ($1.3 < |\eta| < 3.0$) it is $\Delta\eta \times \Delta\phi = 0.17 \times 0.17$. The forward region ($3.0 < \eta < 5.2$) is covered by a Cherenkov-based calorimeter (HF), the absorber is made of steel while the active medium are quartz fibers. This forward calorimeter is placed at a distance in z of 11.2 m from the IP and it has been designed to withstand 10 MGy of absorbed dose and is expected to last for ten years during the LHC operation.

The HCAL is primarily used in the reconstruction of hadronic jets originated by the fragmentation and hadronization of final state quarks and gluons. To achieve the best energy resolution on jets the reconstruction combines the measurements from the

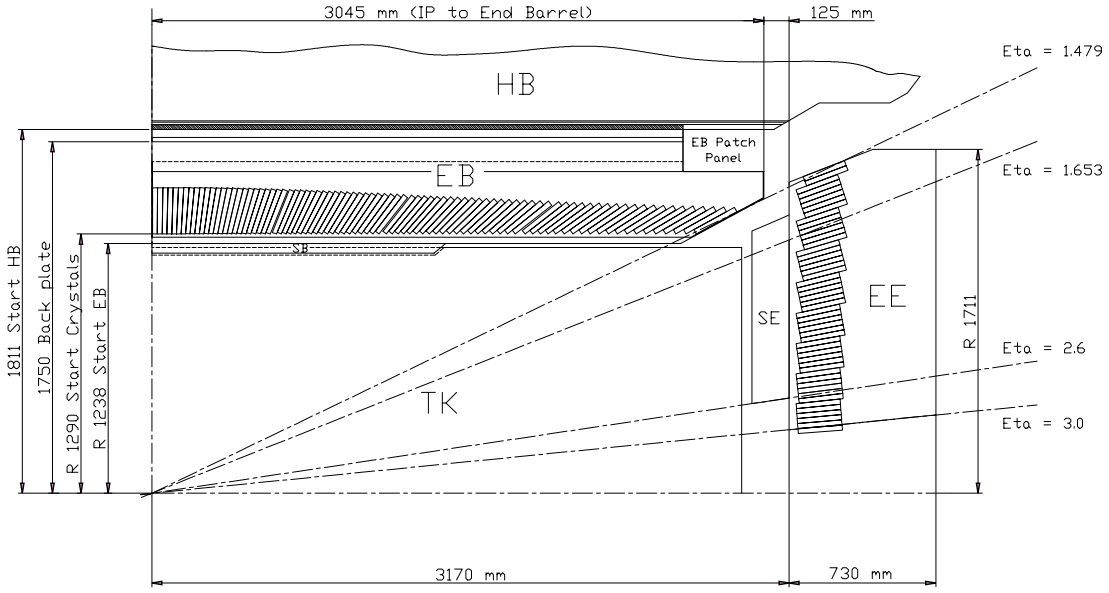

Figure 2.7: Schematic view in the r-z plane of the CMS electromagnetic calorimeter and pre-shower. Only one fourth of the entire system is shown. Only the $PbWO_4$ crystals are drawn, without the supporting frame, cooling and readout electronic boards [29].

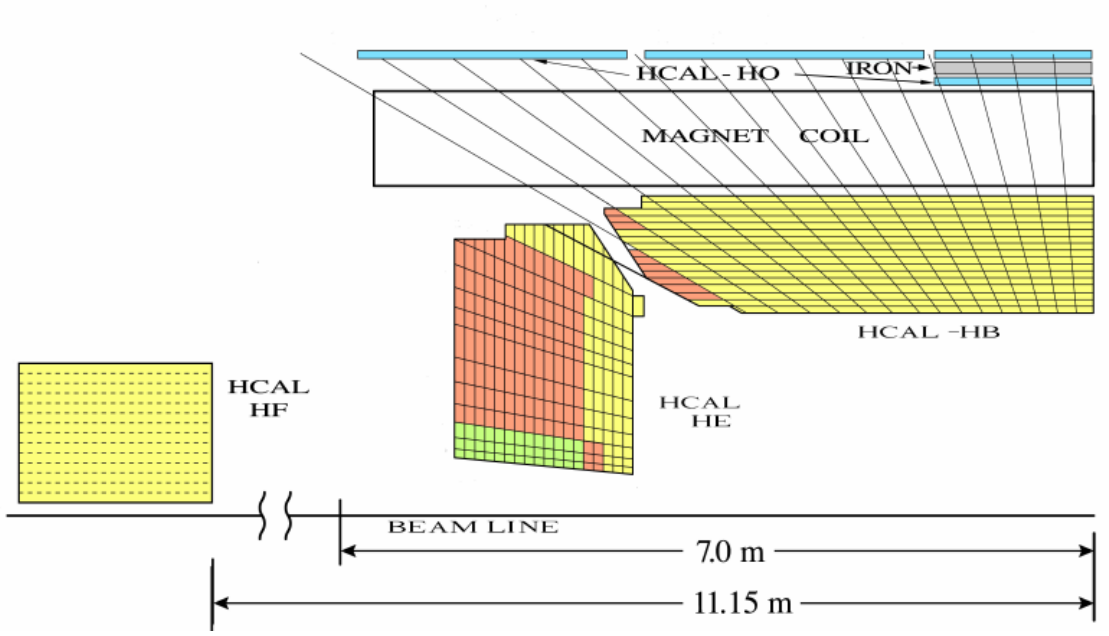

Figure 2.8: Schematic view in the r-z plane of the CMS hadronic calorimeter. Only one fourth of the entire system is shown. All four partitions are visible: the barrel and endcaps parts (HB and HE), the tail catcher installed outside the CMS solenoid and the forward calorimeter.

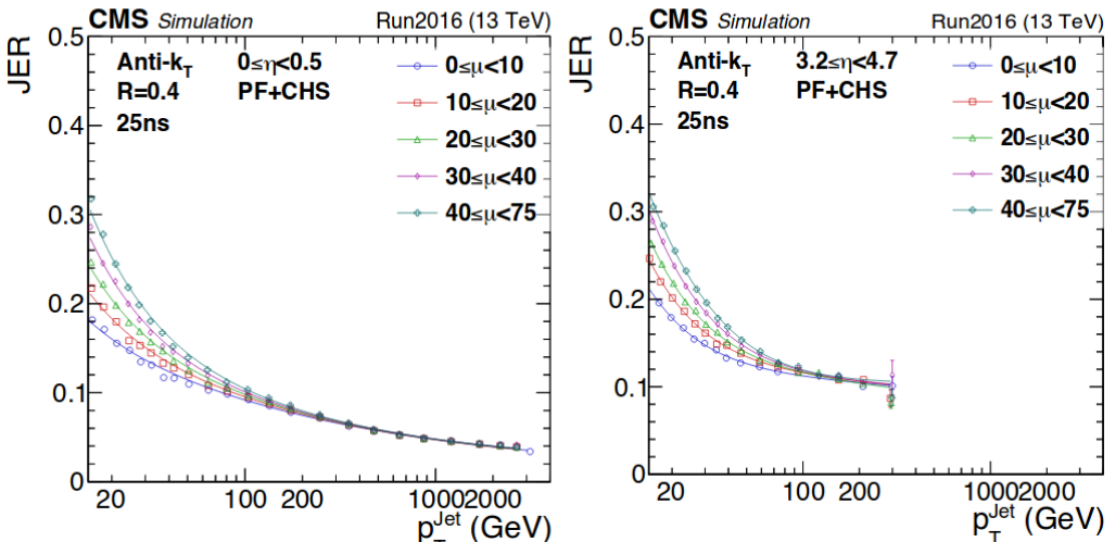

Figure 2.9: Jet energy resolution measured in simulation for jets in the CMS barrel (left) and endcap (right) as a function of the jet transverse momentum. A Gaussian function is fit to the ratio distribution of the reconstructed over generator level energy and the fitted standard deviation of the Gaussian function is quoted as jet energy resolution [30].

tracker, ECAL and HCAL systems. For charged particles with transverse momentum $p_T < 10$ GeV the tracker outperforms the HCAL, thus the energy measurement used in the jet reconstruction is that of the tracker while at higher transverse momentum the measurement of the HCAL is used. Figure 2.9 shows the combined performance of the CMS detectors measured in a simulation with the detector response tuned to match that of the 2016 data-taking period. Charged particles not compatible with the event primary interaction vertex are not included in the jet clustering.

2.3.3 The muon system

The CMS muon system [31] provides full geometric coverage for muon measurement up to $|\eta| = 2.4$. The detectors are embedded in the magnet return yoke, so that muon momentum and charge measurements can also exploit the strong return magnetic field (Figure 2.10). This is particularly important for muons with transverse momentum in the ~ 1 TeV range, for which the complementary tracker measurements degrade.

The CMS muon spectrometer exploits three different detector tecnologies; the need of a fast response to generate a muon trigger and that of high spatial resolution for excellent momentum determination could not be satisfied by a unique technology. Both in the barrel ($|\eta| < 1.2$) and endcaps $0.9 < |\eta| < 2.4$ resistive-plate-chambers (RPC) are used to signal the presence of high energy muons at trigger level (up to $|\eta| < 2.1$). Drift-tube (DT) and catode-strip-chambers (CSC) based detectors provide the momentum measurement in the barrel and endcaps respectively. The angular resolution in ϕ is of about 1 mrad.

The RPC and DT detectors are alternated in concentric rings at a radius between 4 and 7 m from the IP in the barrel region. The rings are arranged in a way that avoids geometrical gaps in the ϕ projection, gaps in the η one are avoided by placing the detectors parallel to the z-axis. In the endcaps the CSC are alternated to the RPC detectors in six consecutive disc on each side of the IP, the CSC detectors inner region is placed at a

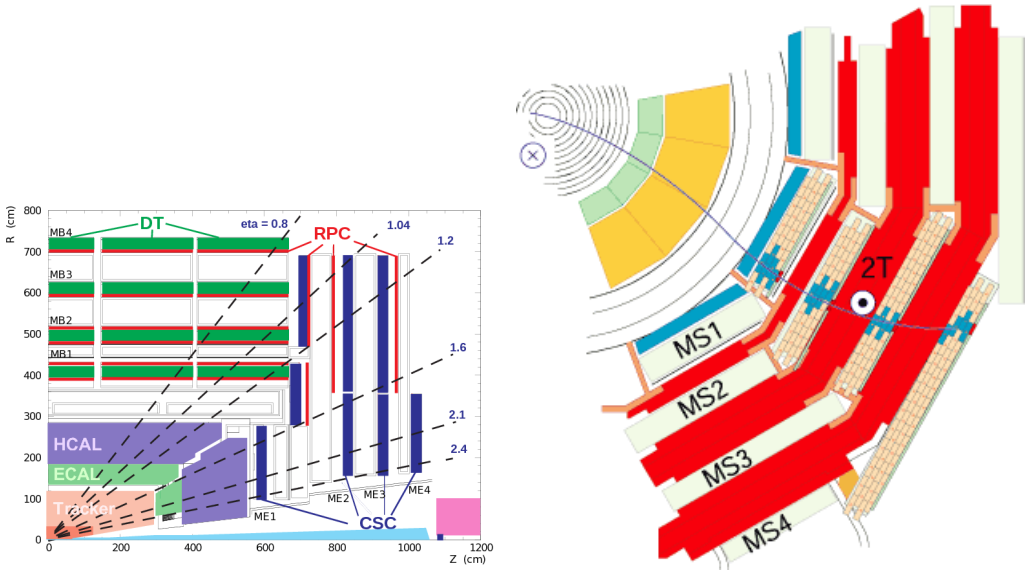

Figure 2.10: Layout of one quadrant of CMS in the longitudinal (left) and transverse (right) planes. The four DT stations in the barrel (MB1-MB4, green), the four CSC stations in the endcap (ME1-ME4, blue), and the RPC stations (red) are shown.

radius of 1 m from the beamline.

2.3.4 The trigger system

The collision rate (40 MHz) is higher than the rate at which event can be recorded and stored for offline processing (1 kHz). A two stage trigger system has been implemented to select events containing a potentially interesting hard scattering within the tens of concurrent collisions happening at each bunch-crossing.

The first level (Level-1 trigger) is hardware implemented in the readout electronics of each sub-system except for the tracker. The hardware used is based on custom chips programmed with a dedicated firmware. The Level-1 triggers involve the calorimetry and muon systems, as well as some correlation of information between these systems. The Level-1 decision is based on the presence of trigger primitive objects such as photons, electrons, muons, and jets above adjustable transverse energy thresholds. It also employs the global sum of $E_T = \sqrt{m^2 + p_T^2}$ and E_T^{miss} [32]. Reduced-granularity and reduced-resolution data are used to reconstruct trigger candidates. The Level-1 trigger reduces the event rate to 100 kHz.

The second level (high level trigger or HLT) reduces the rate to 1 kHz and performs a simplified and faster version of the final event reconstruction. The main idea is to run the event reconstruction on demand in cascade for different types of objects such that non-interesting events can be discarded without running the whole event reconstruction. The HLT runs on commercial CPUs, a set of different trigger algorithms are implemented such that the events are classified accordinlgy to their topology (i.e. events with a muon pair, electron pair, large E_T^{miss}, ...).

In addition to triggers where all events that satisfies the requirements are saved (unprescaled triggers), a set of utility triggers, whose rate would be too high due to band saturation, have been developed, where a good event is saved every N times (prescaled triggers, with a prescale parameter N). These trigger paths are used for detector studies

and to study kinematical regions of object reconstruction, such as low p_T leptons.

2.3.5 The event reconstruction

Events selected by the HLT trigger are stored and analyzed on a world-wide network of computers. Events can be reconstructed several times if a better calibration of the detector or reconstruction algorithm is developed. The CMS event reconstruction core is the so called particle-flow algorithm (PF) [33]. The PF main idea is to combine information coming from the different systems, for instance charged hadrons are detected both in the tracker as tracks and by the HCAL as energy deposit. Combining the momentum measurement of the tracker with the energy measurement of the HCAL improves the overall energy resolution on hadronic jets. Electrons and photons are primarly reconstructed as energy clusters in the ECAL, the tracker information is used to discriminate electrons from photons. A clustering algorithm is used to recover energy loss by bremsstrahlung or photon conversion. Jets of charged and neutral hadrons are clustered using various algorithms accordingly to the particular needs of an analysis. Leptons and photons are distinguished from jets by requiring isolation criteria. Finally the missing transverse energy is calculated as:

$$E_T^{mis} = -\Sigma \vec{E_T^{miss}}$$

where the sum runs over all the objects reconstructed by combining all the system information using the PF algorithm.

Chapter 3

ECAL energy reconstruction and calibration

In this chapter the reconstruction and calibration of the energy measured by the ECAL is presented. Photons are detected only by the ECAL and the analysis sensitivity strongly depends on the ECAL energy resolution. Furthermore some of the variables used to discriminate photons from jets (see Section 4.4) also relies on ECAL information and the stability over the whole data-taking of such variables is important to ensure an optimal selection efficiency.

3.1 Energy reconstruction

A photon or electron entering the ECAL produces a shower of secondary particles in the $PbWO_4$ crystals. The energy of these electromagnetic showers is deposited in crystal matrices. On average the electrons/photons leave 94% of their total energy in a 3×3 crystal matrix and 97% of their total energy in a 5×5 crystal matrix surrounding the crystal hit by the particle. Electrons are reconstructed combining ECAL and tracker measurements [34], while the photon reconstruction relies only on the ECAL [35].

Since the electromagnetic shower generated by a photon or electron span more than one crystal, the energy reconstruction involves both the measurement of the scintillation light in the crystals the clustering of signals originated by the same particle. The clustering takes into account also bremsstrahlung and photon conversion processes that take place in the tracker and which, due to the intense magnetic field, spread the energy deposition along ϕ. The clustering algorithm [36] begins first with the formation of "basic clusters": crystals with an energy above few hundreds MeV are grouped together, the energy threshold depends on the detector conditions (noise and pileup) and varies between 100 MeV and 1 GeV. The basic clusters are then merged together to form a "supercluster", which is extended in ϕ, to recover the radiated energy. The different geometric arrangement of the crystals in the barrel and endcap regions implies that a different clustering algorithm is used for two regions. The algorithms do not make any hypothesis as to whether the particle originating from the interaction point is a photon or an electron, consequently electrons from $Z \rightarrow e^+e^-$ events can provide excellent measurements of the photon reconstruction and identification efficiencies, and of the photon energy scale and resolution. The clustering algorithms achieve a rather complete ($\sim 95\%$) collection of the energy of photons and electrons, even those that undergo conversion and bremsstrahlung

in the material in front of the ECAL. The energy in a supercluster can be expressed as:

$$E_{e,\gamma} = F_{e,\gamma} \cdot \left[G \cdot \sum_i (S_i(t) \cdot C_i \cdot A_i) + E_{ES} \right]. \quad (3.1)$$

The sum runs over the crystals composing the supercluster and the terms represent:

- A_i: the signal amplitude in ADC count estimated with the method explained in Section 3.1.1.
- C_i: the intercalibration coefficient which equalizes relative differences in the crystals response.
- $S_i(t)$: the time dependent correction for the loss of transparency explained in Section 3.2.
- G: the scale coefficient to convert the digital scale measured in ADC count to energy scale expressed in GeV. It has two values: one for the EB and one for the EE set comparing the scale between data and simulation in Z $\rightarrow e^+e^-$ events.
- E_{ES}: Only for electrons or photons in the acceptance region of the ECAL preshower the energy measured by the ES is summed to that of the ECAL supercluster.
- $F_{e,\gamma}$: supercluster energy correction. Several effect like shower non-containment, pile-up and loss of energy in the tracker are corrected with a regression technique trained on simulation. The factor also takes into account the slightly different shower development of electron and photons.

3.1.1 Signal reconstruction

The scintillation light, emitted by $PbWO_4$, is measured by the photo-detectors as explained in Section 2.3.2 and read out as an analog signal by the front-end electronics. The signal is pre-amplified, shaped and processed by a multi-gain amplifier. A dynamic range spanning from approximately 50 MeV to 3 TeV [37] is achieved thanks to three amplifiers that process the signal in parallel: the amplifiers gains are 1, 6 and 12. For very high energy photons, the ECAL readout electronic system saturates. The dynamic range limit is reached when the energy deposit in a single crystal has a value of about 1.7(2.8) TeV in the barrel (endcaps) and for non irradiated crystals. The highest, non-saturated signal among the three amplifiers is then digitized by a 12-bit ADC operating at 40 MHz, ten consecutive samples are read out by the front-end electronics.

The signal amplitude is reconstructed from the set of ten samples measured for each channel at each event. The method developed for collisions at 13 TeV and LHC bunch spacing of 25 ns estimates the in-time signal amplitude and up to nine out-of-time amplitudes for each signal pulse by a χ^2-minimization via the non-negative-least-squares technique to the ten digitized samples [38]. The signal shape used to estimate the contribution of each energy deposit to each sample is assumed to be the same regardless of when the energy is deposited with respect the in-time one. The goal of such approach is to suppress the contributions from out-of-time (OOT) energy deposits to the measurement of the interesting signals. The OOT amplitudes correspond to energy deposits coming from five bunch crossings that precede the in-time one and four that follow it. Two examples of a fitted pulse shape for a simulated event are shown in Figure 3.1 for the EB and

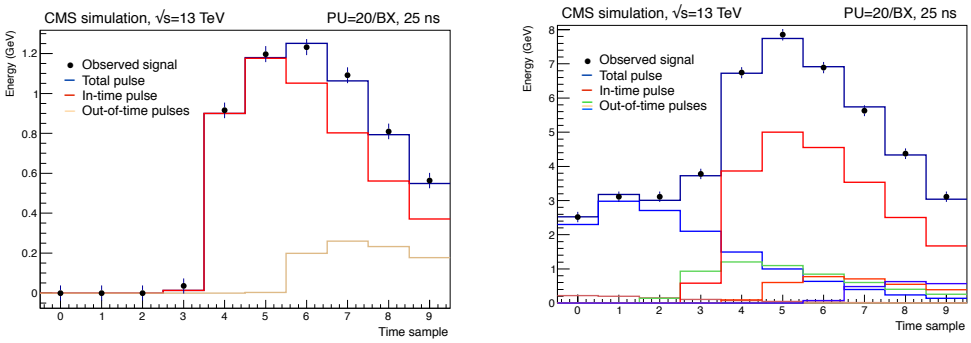

Figure 3.1: Example of fitted pulses for simulated events with 20 average pileup interactions and 25 ns bunch spacing, for a signal in the barrel in two events with one (left) and four (right) OOT energy deposits. Dots represent the 10 digitized samples, the red distributions (other light colors) represent the fitted in-time (out-of time) pulses with positive amplitude. The dark blue histograms represent the sum of all the fitted contributions [38].

the EE category, respectively. This method is not used when at least one of the samples is read-out through either the gain 6 or gain 1 amplifiers since a known non-linearity of electronics (slew-rate) introduces a distortion in the signal shape and therefore bias the estimation of the in-time and out-of-time amplitudes. In such cases since the in-time signal is usually much larger than the out-of-time ones, the amplitude of the sixth sample is taken as measurement of the in-time energy deposit.

3.2 The laser monitoring system

The optical transmission within crystals at the scintillation wavelengths is affected by the production of color centers under ionizing electromagnetic radiation. This transparency loss process is not permanent, in fact spontaneous annealing of the colour centers occurs also at room temperature and leads to a transmission recovery, which is evident when the crystals are not irradiated, such as during machine-fill gaps or winter stops. Permanent damage can be induced by hadrons traversing the crystals, its impact on the ECAL energy resolution is expected to be below the design limits up to $500\,\mathrm{fb}^{-1}$.

Crystals produced for the ECAL are optimized to reduce the relative variations in light transmission during an LHC collision running period to less than 6% for the barrel crystals (dose rates of 0.15 Gy/h) and less than 20% for the endcaps at $|\eta| = 2.5$ (dose rates of 1.9 Gy/h) [39].

The laser light pulses are directed to individual crystals via a multi-level optical-fibre distribution system. The basic operations for the barrel are the following: laser pulses transported via an optical fibre are injected at a fixed position at the crystal's front face. Then the injected light is collected, with the pair of APDs glued to the crystal's rear face, as for scintillation light from an electromagnetic shower. Although the optical light path is different from that taken by shower scintillation photons, this design guarantees that the light transmission is measured in the relevant region of the light spectrum. The underlying principle is similar for ECAL endcaps; however, due to mechanical constrains, the laser light is injected at a corner of each endcap crystal's rear face, and the light is collected (as for scintillation) via a VPT glued on the crystal's rear face. The intensity of the injected laser is monitored through a set of PN diodes, the ratio between the APDs

amplitude and the one measured with the PN diode is used to monitor the transparency variation. Each PN diode monitors a region composed by 100 to 200 crystals (Figure 3.2).

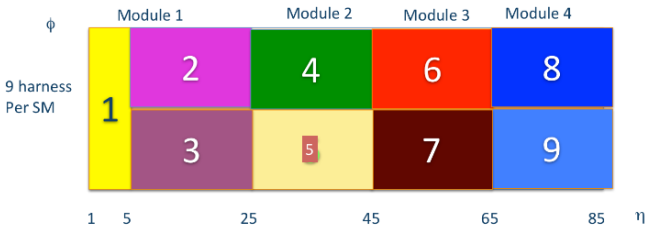

Figure 3.2: PN monitoring regions within an ECAL barrel supermodule. Supermodules in the barrel covers half of the pseudorapidity barrel acceptance and 20° degree in ϕ with a total of 20 crystals. The supermodules are further split in smaller mechnical structure called "modules".

The energy correction factor extracted by means of the laser monitoring system depends on the light collection mechanisms of both electromagnetic showers and injected laser. It is possible to define from first principles a relation between the APD signal amplitude of a electromagnetic shower (S) and the one for injected laser light (R) [62]. The demonstration begins considering the average light optical path (Λ) and the average light attenuation coefficient (λ), which is directly related to the light transmission. If we consider a shower, with ideal amplitude S_0 , which goes through the crystal, the measured amplitude S is:

$$S = S_0 e^{-\frac{\Lambda_S}{\lambda_S}}$$

a similar relation holds for laser light, although the parameters differ since the optical paths for scintillation light and laser light are different:

$$R = R_0 e^{-\frac{\Lambda_R}{\lambda_R}}$$

On average the scintillation light production is isotropic and thus the scintillation light travels a longer path in the crystal before reaching the photo-detector than the injected laser light, the relation between the two can be empirically written as:

$$\frac{S}{S_0} = \left(\frac{R}{R_0}\right)^{\alpha} \tag{3.2}$$

where $\alpha = \frac{\Lambda_S \lambda_R}{\Lambda_R \lambda_S}$ is an empiric parameter.

The laser light is injected regularly during the CMS data-taking either during periods between LHC fills or during the abort gap (a series of several empty bunch crossings during which the special magnets are turned on to dump the beam), the response is monitored with a granularity of about 40 minutes. Three laser wavelength are available: blue (447 nm), green (527nm) and infrared. The blue laser is preferred since it is the closest one to the scintillation spectrum.

Following Equation 3.2, the correction for the transparency loss is computed as:

$$LC(t) = \left(\frac{R(t)}{R(t_0)}\right)^{\alpha}$$

The reference response $R(t_0)$ is currently set to the one measured at the beginning of 2011 and its history is reported in Figure 3.3. The response $R(t)$ is computed as the ratio

between the APDs signal and the PN signal ($APD(t)/PN(t)$). As described above a PN diode is used to monitor the intensity of the injected light to avoid response variations due to laser instabilities. Since the absolute intensity of the laser light injected in each crystal is unknown and may vary from channel to channel (different fibers length, imperfect mechanical and optical matching, ...) it is impossible to estimate the value of α with a single measurement. Furthermore the value of α depends on the absolute transparency of the crystal, which varies under irradiation. The average value of α both for barrel and endcaps crystals was determined thanks to a series of measurement perform at beam test before the CMS installation and in-situ during the first years of data-taking. The limited set of data available allowed only to determine the average value for the EB and the EE, which were measured to be 1.52 and 1.16 respectively. These values are currently used in the energy reconstruction. The majority of the ECAL crystals were produced in Russia by BCTP while a minor fraction was produced in China by SIC, for these last crystals the value of α was measured to be 1. From the same studies the spread of the value of α among crystals of the same producer is known to be around 10%. An in-situ measurement of α for each single crystal, obtained with data collected during 2016, is reported in Section 3.3.3.

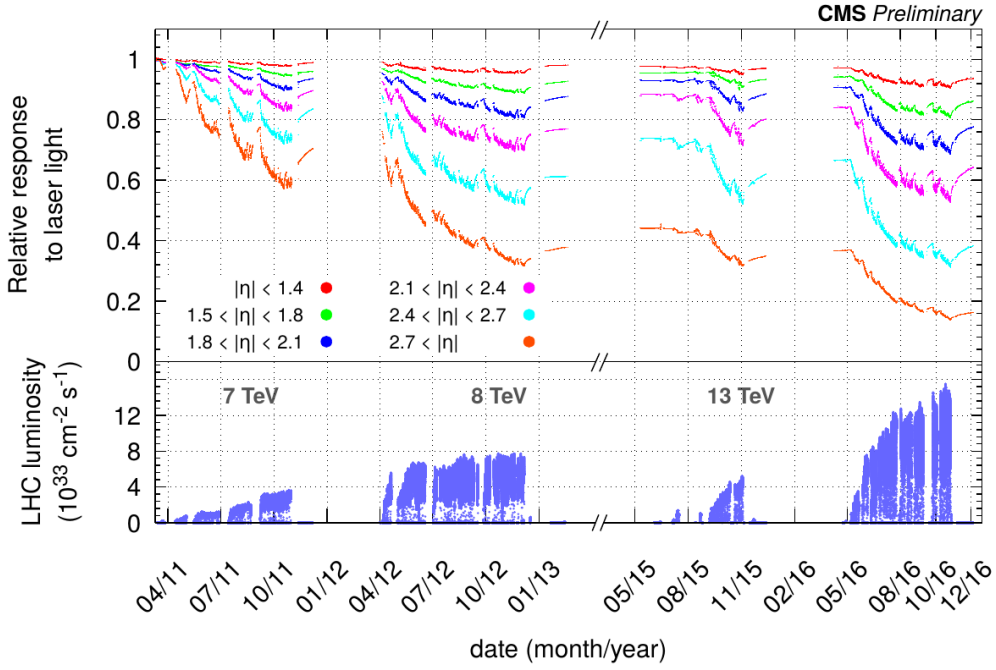

Figure 3.3: Relative response to laser light (440 nm in 2011 and 447 nm from 2012 onward) injected in the ECAL crystals, measured by the ECAL laser monitoring system, averaged over all crystals in bins of pseudorapidity, for the 2011, 2012, 2015 and 2016 data taking periods, with magnetic field at 3.8 T. The response change observed in the ECAL channels is up to 10% in the barrel and it reaches up to 50% at $\eta \sim 2.5$, the limit of the tracker acceptance. The response change is up to 90% in the region closest to the beam pipe [40].

3.3 ECAL single channel intercalibration and response monitoring

The electromagnetic calorimeter of CMS has been specifically designed to provide optimal energy resolution for photons coming from Higgs boson decays, so that the advantages of such a narrow resonance are maintained. The ECAL energy resolution is parametrized by:

$$\frac{\sigma_E}{E} = \frac{A}{\sqrt{E(GeV)}} \oplus \frac{B}{E(GeV)} \oplus C \tag{3.3}$$

the values of the stochastic and noise terms are respectively $A \simeq 2.8\%$ and $B \simeq 12\%$. It follows that the energy resolution for electrons or photons with $E_{e,\gamma} > 50$GeV is dominated by the constant term C (see Figure 3.4). This last term, whose target value in CMS is 0.55%, depends on the non-uniformity of the longitudinal light collection, the energy leakage from the rear face of the crystals (addressed with the supercluster energy correction), instabilities in the operation of ECAL and the intercalibration constants accuracy. This last two aspects are the focus of this section and of the current calibration work performed by the ECAL collaboration.

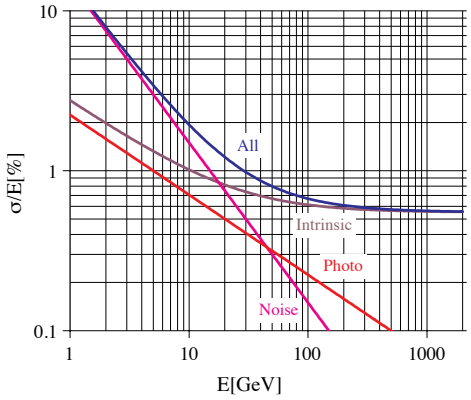

Figure 3.4: Different contributions to the energy resolution of the CMS $PbWO_4$ electromagnetic calorimeter. The noise, photo and intrinsic component depicted in the figure correspond to the A, B and C factors in Equation 3.3

The laser monitoring system provides a way to equalize the response over time but does not allow to correct for absolute response differences among the ECAL channels. The crystal-by-crystal response variation for crystals at the same η ($\eta - ring$) are minimized by means of three techniques, all exploiting collision data:

- Φ-symmetry: this method is based on the assumption that for a large sample of soft interaction events (zero-bias) the total deposited transverse energy ($\sum E_T$) is the same for all the crystals in a η-ring, any observed asymmetry is attributed to a difference in the response of the crystals. Intercalibration in ϕ is performed by comparing the $\sum E_T$ deposited in one crystal with the total transverse energy collected by crystals at the same value of η ($\sum_{\eta-ring} E_T$).

- Intercalibration with π_0 and η mesons: In order to take advantage of the high rate of π_0 decays, a specialized HLT trigger stream has been developed. In addition, a

separate calibration stream has been implemented to select also $\eta \to \gamma\gamma$ decays. An iterative procedure is used to determine the intercalibration constants. The π_0/η invariant mass distribution is fitted with a Gaussian function, for the signal, and a fourth-order polynomial for the background. Then the intercalibration constants are updated iteratively to correct the fitted mass value in each channel.

- Intercalibration with isolated electrons: this method selects high energy electrons coming from the decay of W and Z bosons. As the previous method it uses an iterative algorithm [36] that minimizes the difference $E/p - 1$, where E is the energy measured by the ECAL while p is the momentum measured with the tracker. The crystals belonging to each electron supercluster are inter-calibrated during the iterative procedure.

The $\Phi - symmetry$ method is bounded by definition to provide intercalibration coefficients that average to unity over an η-ring, for the other two methods instead this requirements is imposed after the intercalibration is completed. Ring-by-ring response variations are corrected using Z $\to e^+e^-$ events, for each electron/positron the most energetic crystal in the supercluster determines to which $\eta - ring$ the supercluster belongs to. The ring response is adjusted by fitting the dielectron invariant mass distribution around the Z peak selecting electrons pairs belonging to different η-rings.

The three methods have different properties mainly arising from the different energy spectrum used to intercalibrate the ECAL channel responses. The $\Phi - symmetry$ method profits from the very large sample of soft collisions and allows to derive a set of intercalibration constants with just a few hundreds pb^{-1} but given the low energy of the particles used for the calibration (in the 1-10 GeV range) it is also affected by a larger uncertainty when compared with the other two methods. The uncertainty arises from the presence of ϕ asymmetric material in front of ECAL (the tracker system and its services), for these reason the main use of the Φ-symmetry in the context of intercalibration is to compute correction factors to adjust the intercalibration values over time for effects such the imprecise knowledge of the α parameter. In this case the effect of the material cancels out since it does not change with time. A notable exception is when a change in the center of mass energy of the collisions occurs as explained in Section 3.3.2.

The method exploiting π_0 and η is less affected by the presence of material in front of ECAL and still counts on a large data sample but has a poor selection efficiency in the endcaps due to pile-up.

Finally the intercalibration with electrons from W and Z bosons decays although limited by the cross section of the decay processes is much less affected by systematic effects and has the best precision over the whole η range.

All three methods are also used to monitor the ECAL energy response during the data-taking. The monitored quantities are:

- Φ-symmetry: the ratio of the intercalibration coefficient at a given time over the reference value ($IC(t)/IC(t_0)$).
- π_0/η: the peak of the π_0 invariant mass distribution.
- Isolated electrons: the E/p ratio.

The last two can have a very thin time granularity (several points for each LHC fill) but a spatial granularity of no less than 200 crystals (the same granularity of the PN diode in the barrel). The monitoring Φ-symmetry instead provides a measurement of each crystal IC every $400\,\mathrm{pb}^{-1}$ corresponding typically to one or two days of data-taking.

3.3.1 The Φ-symmetry method

In this section the Φ-symmetry intercalibration method is presented in details together with the results achieved during the LHC Run 2 (at 13 TeV center-of-mass energy).

The Φ-symmetry intercalibration method profits from the feature of the CMS trigger that provides the possibility to record events at a higher rate than that allowed for standard physics data by storing only a fraction of the information coming from the detector. For the purpose of the ECAL intercalibration only the signals coming from ECAL channels with an amplitude over a configurable threshold are stored. The threshold is set to a value that is, on average, equal to 10 times the RMS of the electronic noise. The noise level depends on the level of radiation damage in the APDs while is constant for crystals read by VPTs. The corrections for the transparency loss are not applied at this stage, for this reason the thresholds raises with time and η for channels in the EB (Figure 3.5, top left) while is constant in the EE (Figure 3.5, bottom left).

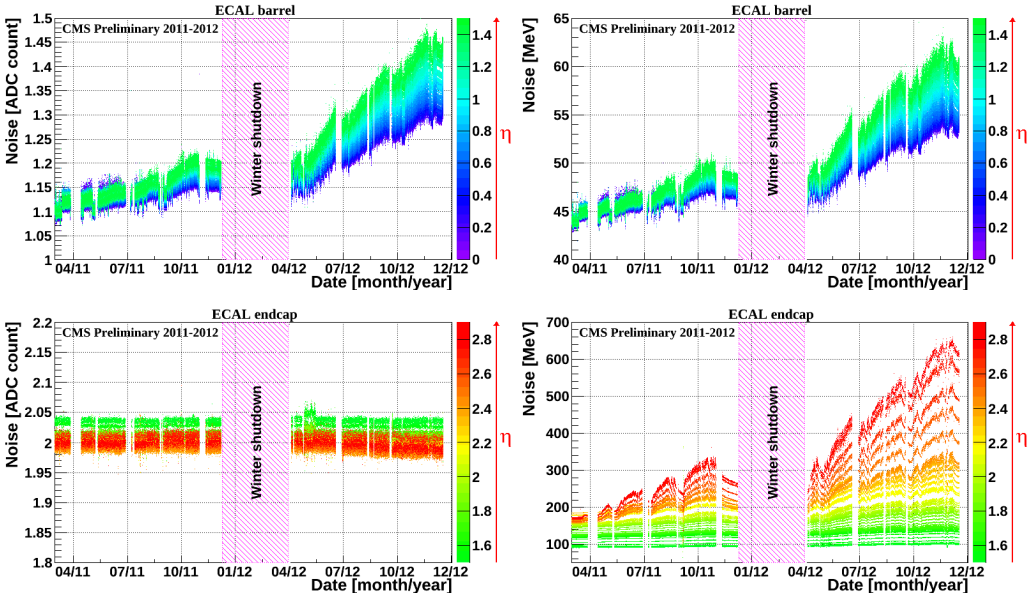

Figure 3.5: Single channel noise measured on the pre-samples of the laser events taken during standard monitoring sequences in 2011 and 2012. The left plot shows the noise in ADC count prior the correction for the response loss measured with the laser system while the right one the noise in MeV after the correction. Top (bottom) plots includes channels of the ECAL barrel (endcaps) [41].

During 2015 and 2016 the calibration stream recorded events at a variable rate between 1 and 3 kHz with peaks of 20 kHz during commissioning periods. The rate is kept under control by pre-scaling zero-bias events (whose rate is almost 40 MHz).

The loss of transparency occurring in the crystals increases the equivalent noise (expressed in GeV) since the signal amplitude in ADC count is multiplied by the transparency correction derived with the laser system. For this reason the events used in the intercalibration process are required to have an energy above a thresholds (E_{min}) that takes into account both the noise level and the loss of transparency and to have a transverse energy not grater then $E_{min}/cosh(\eta) + 1$ GeV. This higher bound avoids that the energy sum used in the intercalibration is biased along a certain ϕ direction by energetic deposit coming from hard scatterings which might not be ϕ-symmetric. The E_{min} depends on

the level of irradiation ad was set to 0.8 GeV in 2015 and 0.9 GeV in 2016, these values were optimized to avoid noise induced distortions of the spectrum while keeping the amount of data needed to derive an intercalibration close to that recorded in a typical LHC fill. Selecting only deposits in a fixed energy window overestimates any response mis-calibration. This effect in taken into account by introducing a scaling parameter (k) in the intercalibration formula to correct the ratio $\sum E_T / \sum_{\eta-ring} E_T$:

$$IC = \left(\frac{\sum E_T}{\sum_{\eta-ring} E_T} \cdot \frac{1}{k} \right)^{-1}$$

The sum over one $\eta - ring$ is also computed on a truncated spectrum. The effect of the truncation on the $\sum_{\eta-ring} E_T$ is just a scale factor common to all crystal in the $\eta - ring$ which is absorbed by rescaling the IC such that the average in each $\eta - ring$ is one before deriving the ring-to-ring intercalibration. The k parameter is estimated by multiplying the reconstructed energy of each hit by ten known mis-calibration values ($m_{true} \in [0.9, 1.1]$), the observed mis-calibration is computed as:

$$m_{obs} = \frac{\sum E_T(m_{true})}{\sum E_T}$$

and the k parameter is finally extracted as the slope of the linear fit to the distribution of m_{obs} versus m_{true}. The k parameter depends on the shape of the E_T spectrum so it is computed each time a set of intercalibration is derived and for each ECAL channel independently, in this way variation of the spectrum induced by the different transparency conditions are taken into account. Typical values for the k parameter are within 2 and 2.5. A preliminary intercalibration is applied in the reconstruction of the events used to derive the ICs, for this reason the ICs are correction factors to be applied to the original intercalibration coefficients in order to obtain a new set of coefficients.

The statistical precision on the intercalibration values is estimated by dividing the dataset by even and odd event number and by computing the IC for each channel with the two separate sub-dataset. The RMS of the crystals $(IC_{even} - IC_{odd})/(IC_{even} + IC_{odd})$ distribution divided by $\sqrt{2}$ is quoted as statistical uncertainty on the IC obtained with the full dataset (the uncertainty value is common for all crystals in the EB and EE). Typically a new set of IC is derived for each LHC fill (1-2 days) with a relative statistical uncertainty of about 0.4%.

The Φ-symmetry method extensively uses data driven techniques since the large dataset collected from soft collisions at LHC and the variable condition of the detector are hardly reproducible with the simulation.

3.3.2 Energy calibration of the ECAL in 2015

After two years of long shutdown LHC resumed operation in 2015 with a higher beam energy 6.5 TeV (instead of 4 TeV) resulting in 13 TeV of center of mass energy for the p-p collisions. The single channel response of the ECAL, although corrected for the response variation measured with the laser system, has been corrected with a new set of intercalibration coefficients derived combining the three intercalibration methods. The Φ-symmetry method is used to derive "transport factors" of the intercalibration coefficients, the assumption behind this proedure is that variation not correct for using the laser system appears as a discrepancy between the ICs measured with the Φ-symmetry in 2012 and 2015. The choice of computing "transport factors" instead of using the

set of ICs to correct the intercalibration coefficients comes from the large impact that the tracker material as well gaps between the ECAL crystal have on the ICs derived with the Φ-symmetry method. By taking the ratio these effects cancel out so that the combination of laser corrections and transport factors can be used to adjust the set of intercalibration coefficients optimezed for the 2012 data-taking to the 2015 conditions. The transport factors are computed with the following procedure: the correction factors (IC) are derived separately on two periods (one at the end 2012 and the other in 2015) using the same seet of intercalibration coefficients for the energy reconstruction. The set was derived with the 2012 detector conditions to optimize the ECAL performance in 2012 data and was also used as preliminary set for the 2015 data-taking by correcting it for the response variation between 2012 and 2015 measured with the laser system only. The "transport factors" are then computed per-channel as the ratio between the two set of IC.

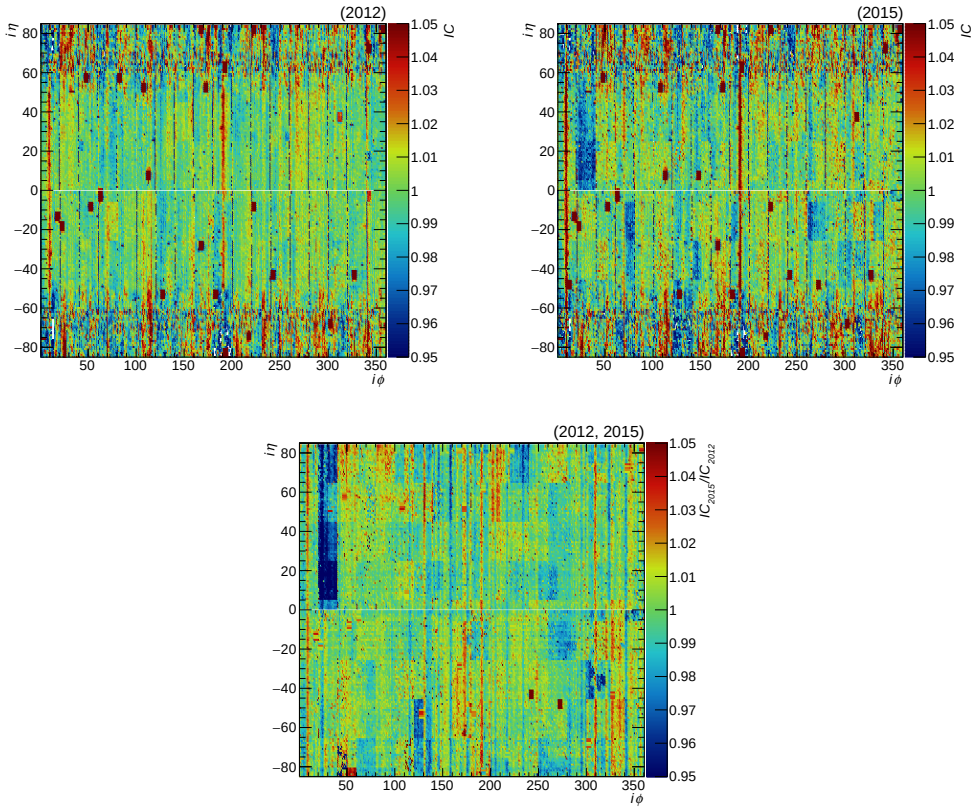

Figure 3.6: Distribution of the correction factor IC obtained with Φ-symmetry for the last period of 2012 (left) and the first of 2015 (right). The IC values are displayed as a function of the η and ϕ position of the crystals. In this and following figures instead of the absolute η and ϕ coordinates the crystal indices $i\eta$ and $i\phi$ are used, this notation allows to identify easily the boundaries of the ECAL barrel partitions (modules and supermodules). The IC variation from unity is in general less in 2012 since the intercalibration coefficient used in the energy reconstruction were derived with the same dataset, therefore the IC shown in the left figure represent the residual mis-calibration observed with Φ-symmetry. The "transport factors" values are shown in the bottom plot. White regions represent dead channels: either single faulty channels or entire malfunctioning 5×5 read-out regions.

As explained in Section 3.3.1 the IC values derived with the Φ-symmetry method are

affected by a large systematic uncertainty due to the presence of material in front of the ECAL, such effect cancels when taking the ratio of two sets of IC computed with data collected at different times. This cancellation however does not occur when the two set of IC are derived with collisions at a different center-of-mass energy. The effect of the material on the IC is clearly visible in Figure 3.6: the presence of support structures and services absorbs part of the particle energy. This translates into a lower than average $\sum E_T$, and consequently higher IC value, for the ECAL crystals installed behind those structures. The material is however uniform along η for crystals within the same tracker partitions (barrel and endcaps), so corrections for the impact of material are computed averaging over η the measured IC values at same ϕ but for two regions in the EB ($|\eta| < 1$ and $1 < |\eta| < 1.4442$). The IC values are scaled for the average supermodule IC and the correction for the $j-th$ ϕ-row is defined as:

$$C_j = \frac{1}{IC_{<\eta>}}$$

The corrections derived in this way are assumed to correct only for crystal-by-crystal variations introduced by the presence of material in front of ECAL and not for real channel response variations. The assumption is tested comparing the correction values derived separately for $\eta < 0$ (C_j^+) and $\eta > 0$ (C_j^-) (Figure 3.8) and checking that the pull distribution $(C_j^+ - C_j^-)/\sqrt{\sigma_j^{+2} + \sigma_j^{-2}}$ has a standard deviation equal to 1 (Figure 3.9). This confirms that the observed variations are independent of η (in the two region defined above) within uncertainties while a channel mis-calibration would appear as a systematic variation of the pull. In total 720 correction values are computed (360 ϕ-row for two η regions) The corrections computed in this way also correct for gaps in the ϕ direction present at the boundary of the ECAL barrel supermodules (Figure 3.7). Crystals in supermodules installed in the positive and negative η sides of the barrel have opposite tilt angles, for this reason the effect of the gaps is on the last crystal of a supermodule for the positive side while on the first one in negative side. Gaps along η are also present as shown in Figure 3.7 but are irrelevant when computing the IC whose average along an η-ring is forced to be equal to one.

The same material induced effects are observed in the endcaps but, given that crystals in the endcaps are arranged in the $x-y$ instead of $\phi-\eta$ plane, no way to factorize it from real channel-to-channel variations has been found and a larger uncertainty has thus been attributed to the IC values derived with Φ-symmetry.

The corrected barrel IC values are shown in Figure 3.10, the channel-by-channel ratio of the two IC set used as "transport factor" are also shown. The "transport factors" values varies across barrel following a patter that matches that of the laser monitoring partitions from no correction up to 5% of the IC value.

To obtain the final channels intercalibration for EB channels the IC values from the three methods are combined, the final values for each channel is the weighed average of the three. The weight used for the combination is the uncertainty on the IC measured by each method and is estimated for each η-ring by computing the variance of the IC difference for each pair of methods. These variances are assumed to be to sum in quadrature of each method uncertainty consequently, the precision of each intercalibration set is extracted by solving three simultaneous equations for the three the uncertainties. The results on the uncertainties are reported in Figure 3.11. Taking advantage of the small statistical uncertainty and the reduced impact of the material the IC derived with Φ-symmetry has the best precision in all η-rings. The intercalibration with electrons precision is dominated by the statistical uncertainty which is smaller at smaller η.

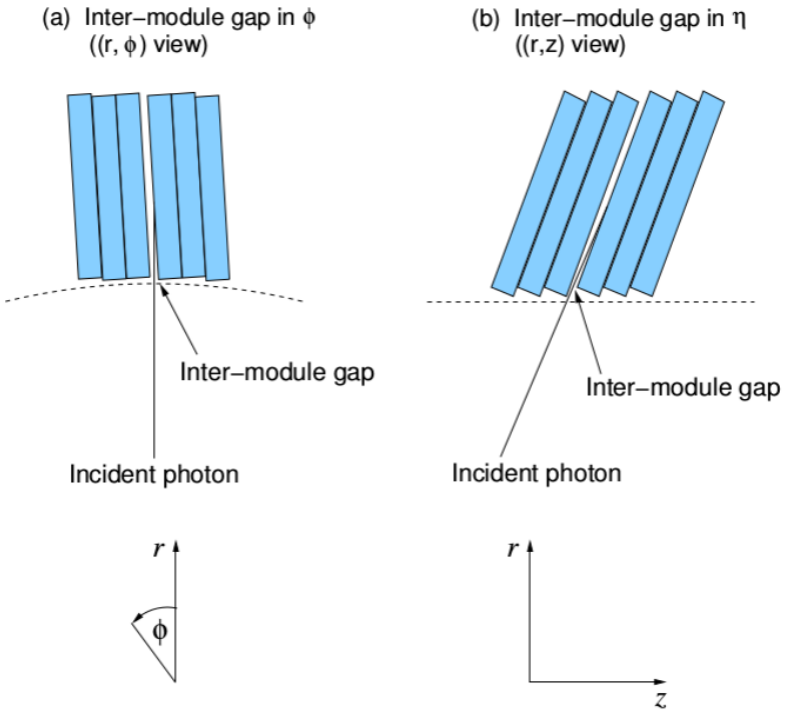

Figure 3.7: Illustration of the effect of the presence of supermodule (left) and module (right) gaps. Due to the 3° off-pointing arrangement, crystals installed at module or supermodules boundaries receive energy flux not only from the front face but also from the face exposed to the gap Such crystals therefore receive more hits than other crystals at the same η.

In the endcaps only intercalibration values from Φ-symmetry and electrons were available and they were combined without weights.

The energy resolution achieved with final intercalibration, including the ring to ring correction derived with the method described in Section 3.3, is shown in Figure 3.12. The resolution σ_E/E is extracted from an unbinned likelihood fit to Z $\rightarrow e^+e^-$ events, using a Breit-Wigner function convolved with a Gaussian as description of the Z boson invariant mass peak. The resolution is affected by the amount of material in front of the ECAL and is degraded in the vicinity of the cracks along the η direction between ECAL modules (indicated by the vertical lines in the plot) The resolution, especially in the barrel, improves significantly after a dedicated calibration by using the transported calibrations derived in 2012 and combining them with the calibrations obtained from the 2015 CMS dataset (blue points), compared to the prompt reconstruction using only the unmodified 2012 calibrations (black points). The resolution in the central barrel reaches the level achieved in Run1, while in the endcaps the resolution is still significantly affected by the statistical precision of the calibration (derived with a dataset equivalent to 2.6 fb^{-1}).

The residual differences between data and simulation are due to the statistical uncertainties (endcaps) and other systematic effects described in [44]. Part of these effects are variations of the response over time that are not corrected using the laser monitoring system data. During 2016 thanks to a larger dataset these effects have been investigated in more details as described in the next section.

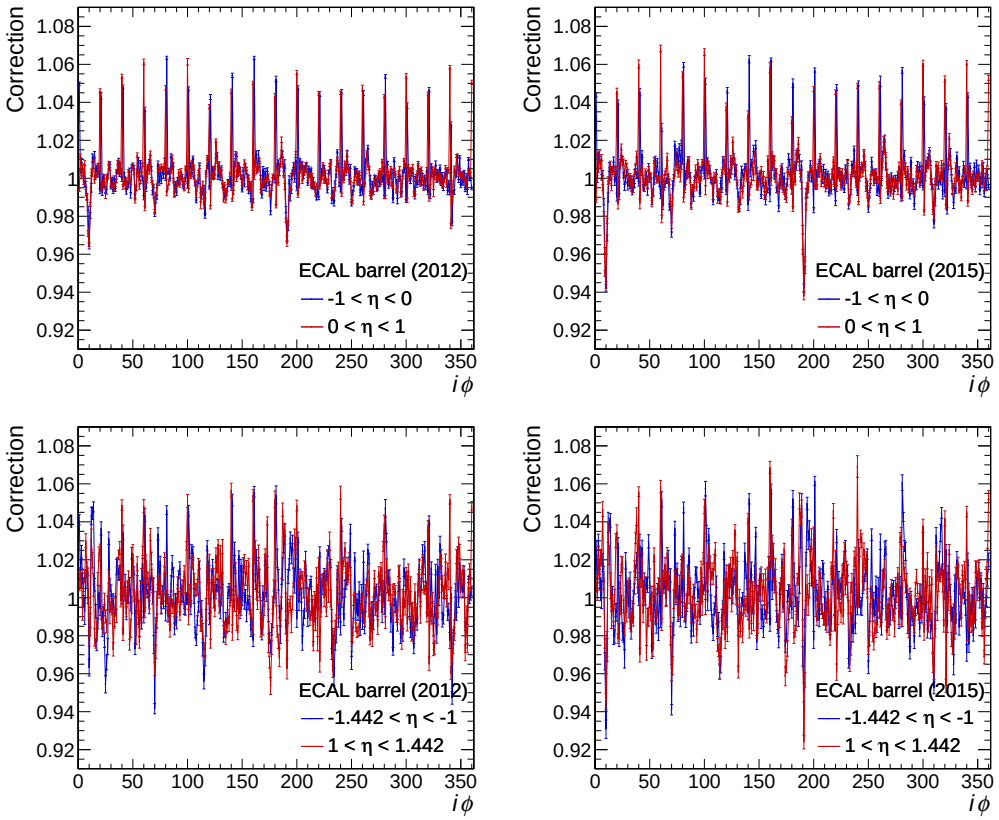

Figure 3.8: Material effect corrections for the barrel inner ($|\eta| < 1$, $i\eta < 60$, top row) and outer ($1 < |\eta| < 1.4442$, bottom row) regions described in the text, the blue (red) curve refers to the negative (positive) η side of the barrel. Plots on the left(right) side show the corrections for the 2012(2015) IC. Supermodules gaps affect the IC of the first or last crystal in the supermodule if it is located on the negative or positive η side respectively. The correction for gaps can be seen in plot as positive correction of about 6% every 20 ϕ-rows while. The magnitude of the correction for material effect the larger for 13 TeV collisions (2015) than for 8 TeV ones, this can be clearly observed in crystals located behind the main tracker support structures located at the 10-th and 190-th ϕ-rows. The correction for gaps at the supermodule boundaries are on the other end independent of the collisions energy since they only depend on the acceptance variation induced by the gaps.

3.3.3 ECAL energy response monitoring in 2016

Given the relative short break between the two data-taking periods (compared to the LS1) the calibration obtained with data in 2015, corrected for the response variation due to transparency gain observed with the laser system, was used as baseline for the energy reconstruction during the 2016 data-taking period. The energy reconstruction algorithm described in Section 3.1 was found to depend on both the crystal-by-crystal noise level and signal shape used in the fitting procedure, thus a monitoring and prompt adjustment of both quantities was developed during the data-taking. The energy calibration process described in this section is based on data reconstructed with the updated and time-dependent reconstruction.

A drift over time of the energy scale was however observed during the year as variation

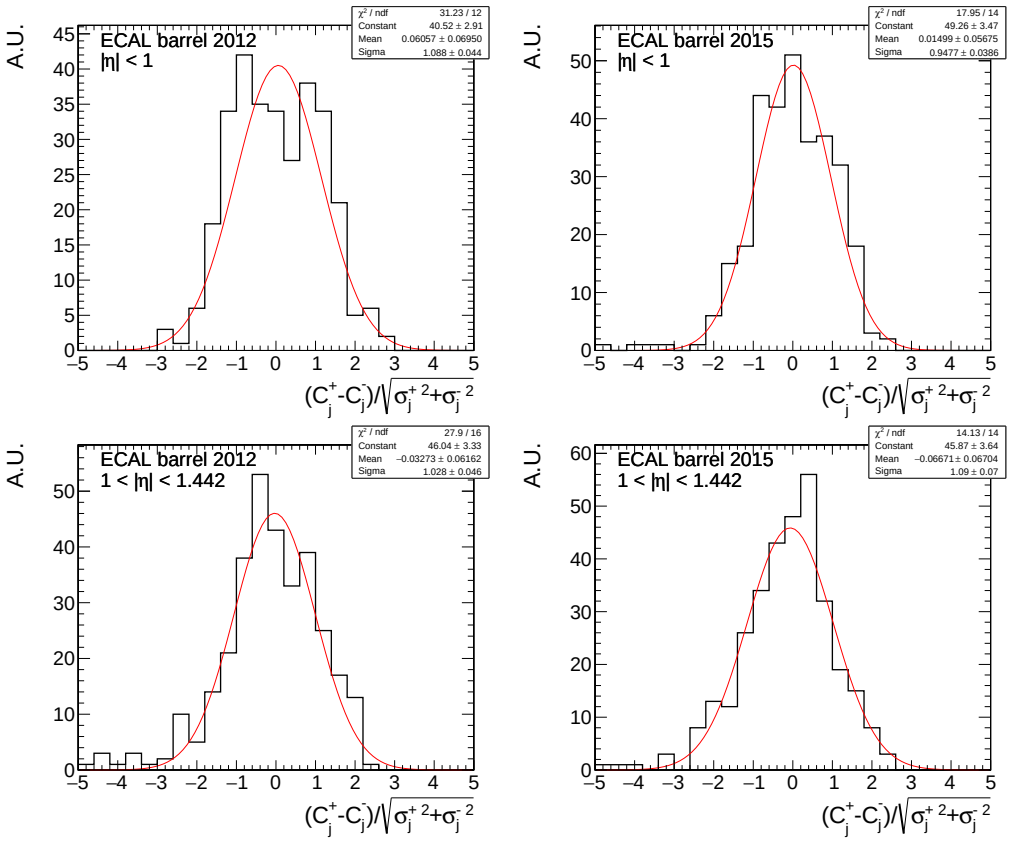

Figure 3.9: Pull distribution of the correction difference between the positive and negative η side of the ECAL barrel. Plots in the top and bottom row show the pull for inner ($|\eta| < 1$, top row) and outer ($1 < |\eta| < 1.4442$ respectively. Left (right) side refers to corrections for 2012 (2015) *IC* set. Crystals located at supermodule boundaries are excluded from the pull since the gaps are, in principle, unrelated between the positive and negative barrel side.

of the Z boson invariant mass peak in the dielectron spectrum, together with a constant worsening of the resolution. As explained in Section 3.2, the transparency variation observed with the laser system differs from the one affecting the scintillation light collection by an exponential factor α.

The per-crystal α parameter can be measured using the same low energy particles from soft collisions uses for the Φ-symmetry intercalibration method. The measurement is performed by minimizing the χ^2:

$$\chi^2 = \sum_{t=0}^{n} \left(\frac{F(t) \cdot \left(\frac{R(t)}{R(t_0)} \right)^{\Delta\alpha}}{\sigma_{F(t)}} \right)^2 \tag{3.4}$$

where $R(t)/R(t_0)$ is the relative response variation to laser light described in Section 3.2, $F(t)$ is the ratio defined in Equation 3.3.3 and $\sigma_{F(t)}$ is the uncertainty on $F(t)$. The $F(t)$ ratio contains the same truncated transverse energy sum used to intercalibrate with the Φ-symmetry method, thus the k parameter used to translate the observed mis-

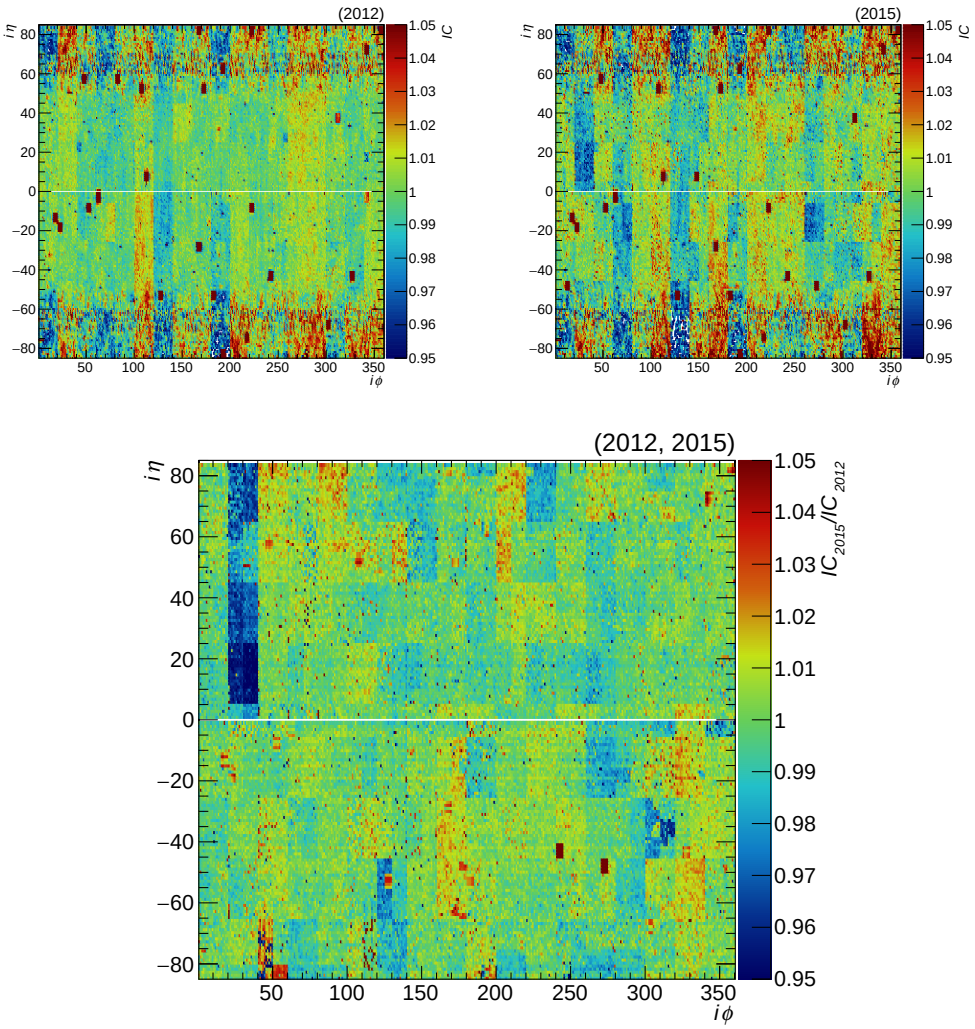

Figure 3.10: Single channel IC (top) for the 2012 (left) and 2015 (right) periods used in the calibration process with Φ-symmetry. Transport factors derived after applying the correction for material effect to the two separate sets of IC (bottom).

calibration into the real one is also applied here:

$$F(t) = \frac{\frac{\sum E_T(t)}{\sum_{EB} E_T(t)} \cdot \frac{1}{k(t)}}{\frac{\sum E_T(t_0)}{\sum_{EB} E_T(t_0)} \cdot \frac{1}{k(t_0)}} \tag{3.5}$$

where $\sum E_T$ is the the same sum used for the intercalibration procedure while $\sum_{EB} E_T$ is the sum over the chosen period of time of all the transverse energy deposited in the EB. Since the uncertainties on $\sum_{EB} E_T$ and $\sum_{\eta-ring} E_T$ are both negligible with respect to the crystal $\sum E_T$, the uncertainty $\sigma_{F(t)}$ is set to equal to the precision on the IC estimated by dividing the data in each calibration period t in even and odd events (about 0.4%, see Section 3.3.2).

The χ^2 (3.4) is minimized with respect to the $\Delta\alpha$ parameter which is the difference between the "true" crystal α and the average value used in the standard reconstruction. The $\sum_{EB} E_T$ normalization chosen to compensate for variations in the instantaneous

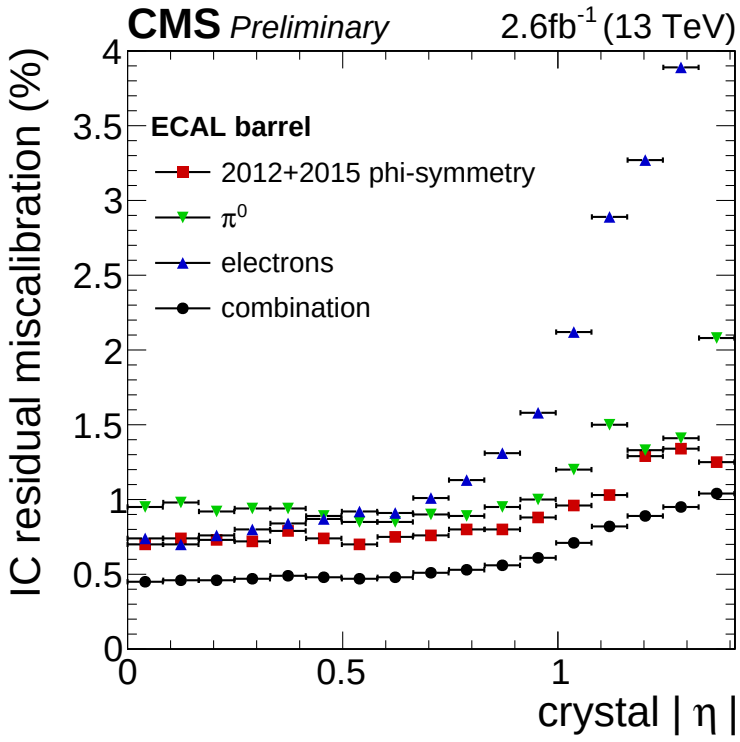

Figure 3.11: Residual mis-calibration of the ECAL Barrel (EB) channel intercalibration, as a function of pseudo-rapidity with the dataset recorded during 2015. The red squares refer to the intercalibrations derived with Run1 data, extrapolated to 2015 using the laser monitoring system, and corrected using the ϕ-symmetry of the low energy deposits in the 2015 dataset. The green points refer to intercalibration constants obtained using photons from $\pi_0 \to \gamma\gamma$ decays, while the blue points to that obtained using electrons from W and Z decay .The black points represent the residual mis-calibration of the combination of the three methods (weighted average). The precision of the Φ-symmetry and π_0 calibrations is at the level of the systematic errors. The precision of the electron calibration is dominated by the statistical errors with the dataset recorded in 2015 (2.6 fb^{-1}) [42].

luminosity or trigger rate, also absorbs variation common to all crystals in the barrel, thus preventing the possibility of measuring a coherent variation of α among all crystals in the ECAL barrel or a global scale variation of ECAL. The $F(t)$ variation over time together with the value of $1/LC(t)$ and the $F(t)$ derived with the fitted crystal α are shown in Figure 3.13 for two crystals in the ECAL barrel.

The fit results are shown in Figure 3.14, the precision on the value of $\Delta\alpha$ extracted from the fit varies between 1.8% and 2%. The measured relative variation of the crystal-by-crystal α varies between $\pm$20% for the majority of the barrel crystals. A notable exception is represented by crystals produced by the SIC company for which an α value of one was measured at the pre-installation beam tests, the value extracted from the fit with 2016 data is on average 1.4. The same fit has been performed also for crystals in the ECAL endcaps but due to the different injection point of the laser light, which makes the response to laser and scintillation light more similar, and the convolved effect of the VPT aging the uncertainty is larger (10%) and the results compatible with the constant α used in the standard reconstruction.

The measured $\Delta\alpha$ values present block patterns in the η-ϕ plane (Figure 3.14 bottom)

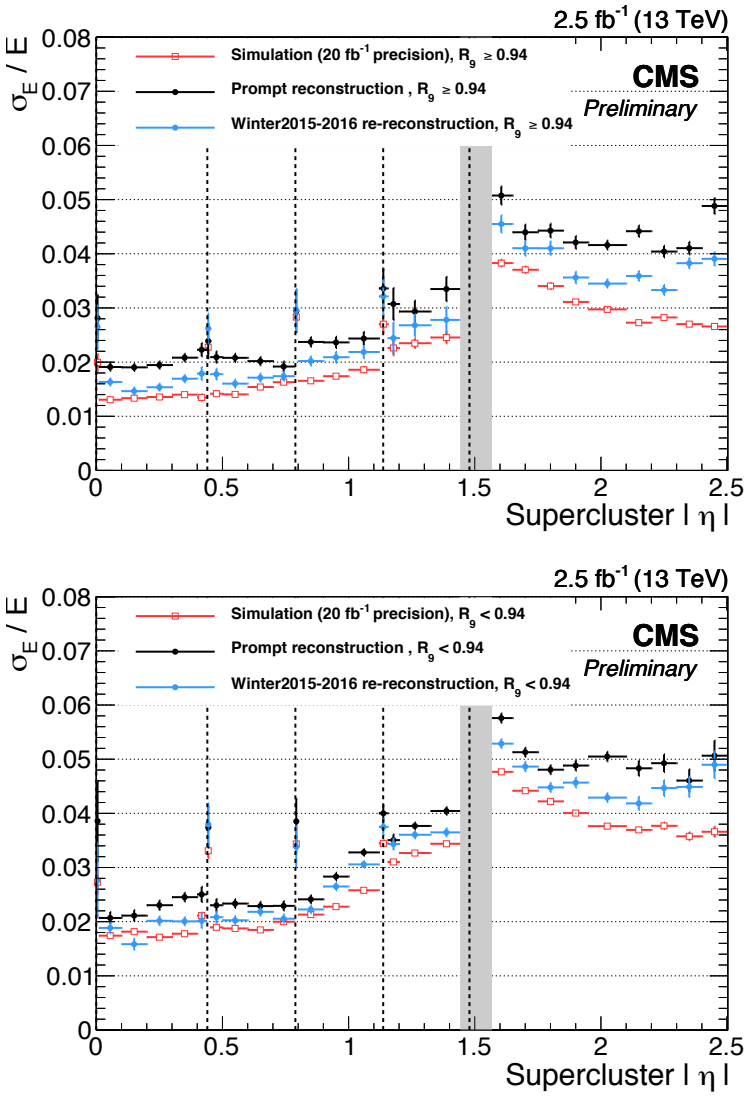

Figure 3.12: Relative electron (ECAL) energy resolution unfolded in bins of pseudo-rapidity η for the barrel and the endcaps [43]. Electrons from $Z \rightarrow e^+e^-$ decays are used. The vertical dashed lines indicate module boundaries while the grey band around $\eta = 1.5$ denotes the transition between barrel and endcaps. The simulated detector calibration reflects that that can be achieved with 20 $fb^{-1}$of data, while the one used for the Prompt reconstruction is was derived in 2012 and adjusted for the transparency variation measured with the laser sustem only while the Winter2015-2016 results are obtained with the optimized calibration described in the text. The resolution is shown for low (top plot) and high (bottom plot) bremsstrahlung electrons, the categorization is based on the R_9 variable ($R9 = E_{3x3}/E_{SC}$, where E_{3x3} is the energy deposited in the most energetic crystal in the cluster and the 8 surrounding ones while E_{SC} is the total supercluster energy as expressed in Equation 3.1)

compatible with the granularity of the PN sensors described in the Section 3.3, with a variation of α within such blocks much smaller than the block to block variations. The observed behaviour is compatible with a linear drift of the PN electronics response and thus unrelated to the crystal α. The effect has been investigated also using electrons from

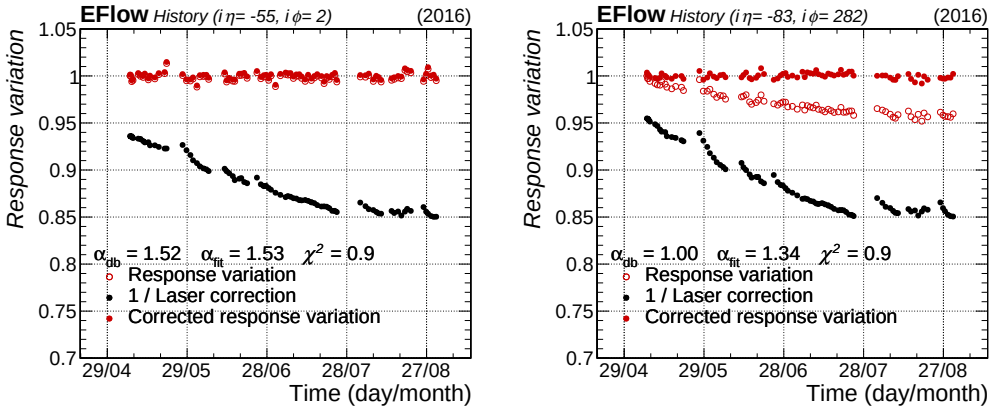

Figure 3.13: Example of $F(t)$ variation over time for two crystals in the ECAL barrel, produced by BTCP (left) and SIC (right). The open red dots are the $F(t)$ values obtain with the constant α value (reported as α_{db} in the figures), while the full red dots are the $F(t)$ values computed using the per-crystal α obtained from the fit described in the text (reported as α_{fit}). The inverse of the correction for laser response variation is also shown (black full dots). For the BTCP crystal the α_{db} gives a stable response while the SIC crystal response varies up to 5% with respect the average ECAL barrel response. The corrected response is reported as closure test of the procedure.

Z and W boson decays, highlighting the same block pattern and an overall coherent drift of the barrel scale, to which the $F(t)$ is insensible for the reason explained above. For this reason an effective correction to each PN block response has been preferred for the final 2016 reconstruction. The correction was derived using the measured average α value of 1.4 for the SIC crystals and by performing a linear fit to the E/p peak variation as a function of time with a granularity of one LHC fill. An example fit for one PN block is shown in Figure 3.15, the measured drifts are equivalent to a scale variation between 0.1%/30days and 0.2%/30days depending on the average $|\eta|$ of the PN block, with larger drift at larger $|\eta|$.

The final energy scale stability and resolution are shown in Figure 3.16: although a good stability on the energy scale is achieved (better than 0.5%) the resolution still get worse during the data-taking period, underlining a residual channel-to-channel response variation.

3.4 Summary

The ECAL energy response is subject to evolution over time mainly due to the loss of transparency of the crystals following irradiation. Although a powerful monitoring system based on the injection of laser light allows to correct for the transparency loss, a residual mis-calibration affects the energy measurement. A new ECAL calibration was derived in 2015 after a two years long LHC shutdown combining the three intercalibration methods developed during the first collision period of LHC, resulting in an energy resolution at the level of 1% for non showering electrons in the barrel and 2.5% in the endcaps comparable to that achieved during the first running period of LHC. During 2016 the time evolution of the detector response was studied in great details, a method to measure a per-crystal α parameter was successfully implemented. The same study lead to the observation of an unexpected drift in the laser monitoring electronics which was corrected using electrons

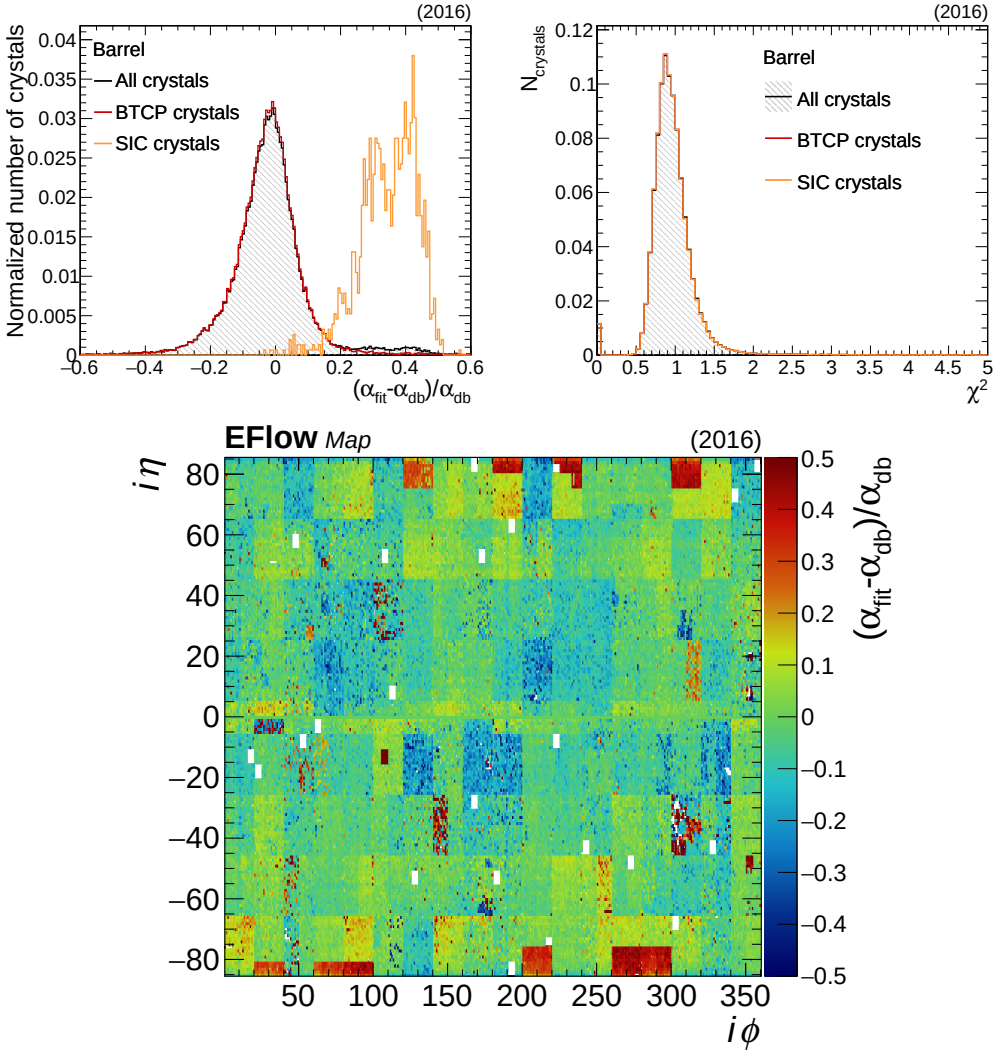

Figure 3.14: Measured $\Delta\alpha$ values for crystals in the barrel (top left) and fit χ^2 (top left), each distribution is normalized to its area. The $\Delta\alpha$ values are reported as relative variations from the α_{db} value of 1.52(1) used in the energy reconstruction for BTCP(SIC) crystals. The bottom plot shows the distribution of the relative $\Delta\alpha$ in the η-ϕ plane (where instead of the absolute η and ϕ coordinates the discrete crystal indices $i\eta$, $i\phi$ are used). The map highlights the SIC crystals (red region at high $|\eta|$) and the block structures described in the text.

from Z and W boson decays. The procedure defined in 2016 will serve as a road-map for future energy calibration of the ECAL.

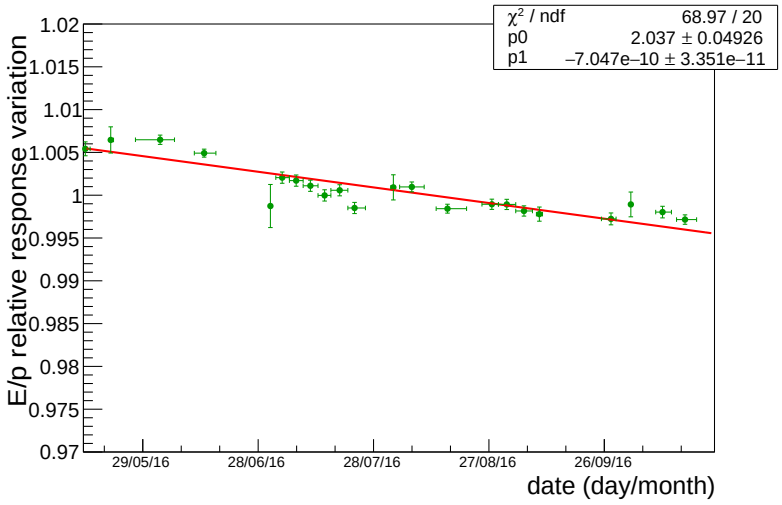

Figure 3.15: Example fit of a region of 200 crystals monitored by the same PN diode. The $p1$ parameter represented the slope of the linear fit and is equivalent to $0.18\%/30days$

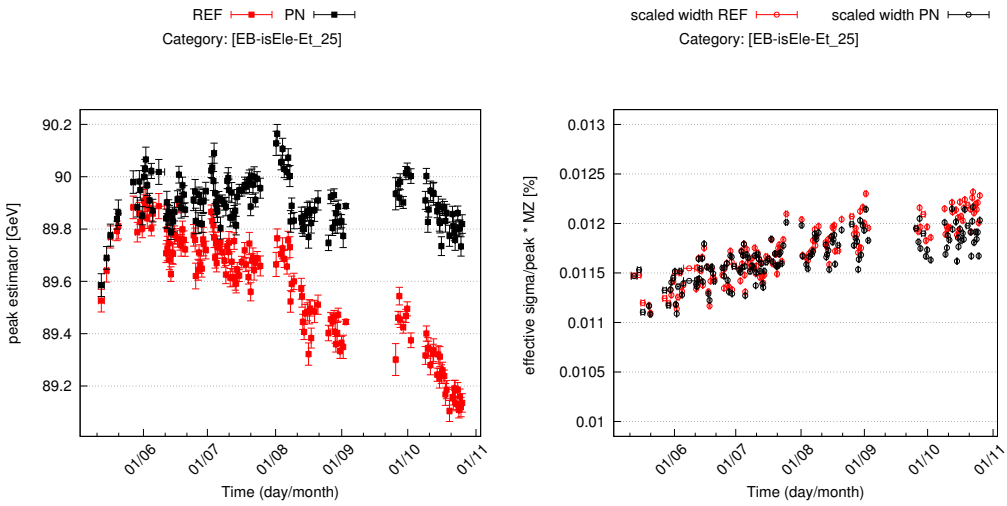

Figure 3.16: ECAL energy scale and resolution stability during the 2016 data-taking period. With the optimized calibration discussed in the text (black) and the calibration of 2015 (red). The energy scale (resolution) stability is displayed on the left (right) and is measured with Z $\rightarrow e^+e^-$ events in which both electrons are detected in the barrel. The peak estimator is the median of the Z invariant mass peak, while the resolution is estimated as the minimal symmetric interval including 68% of the events around the peak and is reported in the plot as the fraction of the estimated Z boson mass value in each period.

Chapter 4

The search for diphoton resonances

In this chapter the search for resonant BSM production of photons pairs is presented. First the analysis approach and the event selections optimization are described, then the statistical analysis is introduced and finally the results are also discussed.

The analysis has been optimized for searches performed on data collected from proton-proton collisions at a center of mass energy of 13 TeV and the results are obtained from the analysis of $35.9\,\text{fb}^{-1}$ of p-p collisions collected by the CMS experiment during 2016.

4.1 Analysis approach

The analysis is optimized to select a pure sample of diphoton events to fit the resulting invariant mass spectrum with a model describing both the background and the hypothetical signal coming from BSM resonances. Given the pure signature of the diphoton event the main background is the standard model production (see Section 1.5) with a marginal contributions from events in which one or both photons are mis-identified hadronic jets. The purity of the sample is found to be more than 90% but no attempt is made to separate the various background contribution and the overall background shape is modeled with a parametric function.

Both the signal model shape and normalization from simulation are corrected for detector effects using data-driven techniques which involves $\text{Z} \rightarrow e^+e^-$ events. The general assumption is that the CMS ECAL responses to electrons and photons are equivalent.

4.2 Data samples

The search is performed in data collected by the CMS experiment during the year 2016. The total integrated luminosity is $35.9\,\text{fb}^{-1}$. Data are reconstructed with a detector calibration optimized for the 2016 p-p collision data-taking period using data collected in 2015 with the method described in Section 3.3.2. The calibration described in Section 3.3.3 provides an improved ECAL energy scale stability which in turn leads through a better resolution to a higher sensitivity of the analysis to narrow resonances and also to an improved stability of some of the variables included in the photon identification. However the technique was developed well after the end of the data-taking and given the limited number of analyses that could potentially profit from the improved performance a reconstruction with the new calibration was delayed and will become available by the end

of 2017. The response variations observed in 2016 and described in details in Section 3.3.3 are corrected with another method described in Section 4.5, which does not correct for the PN diode blocks as the improved technique but only for global scale variations, separately for the ECAL barrel and endcaps.

The events were recorded with a trigger designed to select events containing a pair of energetic photons with $E_T > 60$ GeV. The energy of each photon candidate is computed as the sum of the energy measured by ECAL and HCAL and trigger selections require the energy measured in HCAL to be less than 10(15)% of that measured by ECAL for candidates in the calorimeter barrel(endcap) region. The trigger is found to be fully efficient for photons with $p_T > 75$ GeV and, so an offline selection is applied to select these events.

Together with the main analysis trigger another one is used to select electrons from $Z \to e^+e^-$ decays. The $Z \to e^+e^-$ is the primary control sample for the analysis and events compatible with this process are recorded with a single electron trigger that selects events with at least one electron of $p_T > 27$ GeV and $|\eta| < 2.5$. Tight isolation and identification criteria, corresponding to an efficiency of 70%, are applied at trigger level to maintain a rate compatible with the DAQ capabilities. $Z \to e^+e^-$ events are used to measure the final photon selection efficiency so the single electron trigger is preferred over a double electron one, since in this way an unbiased set of electrons can be constructed from those coming from $Z \to e^+e^-$ decays that did not triggered the event acquisition.

4.3 Monte Carlo simulated samples

The Monte Carlo simulation of the CMS detector and 13 TeV p-p collisions is used. The simulation takes into account both the pileup generated by concurrent interactions and the presence of signals in the detector coming from collisions in other bunch crossings. Events in the simulated samples are weighted to match the pileup energy density distribution measured in data.

4.3.1 Resonant signal simulation

RS gravitons are chosen as a reference for the spin-2 resonance search. SM-like Higgs bosons of high mass and fixed widths are used for the spin-0 case. A set of simulation samples is used to model the detector response to resonant production of two photons. Such samples are generated with PYTHIA8 [45] in the mass range $500 < m_{\gamma\gamma} < 7000$ GeV in steps of 250 GeV for masses below 4 TeV and 500 GeV above it for both spin hypothesis. An additional set of samples without simulation of the detector response are used to model the signal spectrum and the acceptance of the kinematic selections. Three relative width hypothesis $\Gamma/m_{\gamma\gamma}$ are taken as benchmarks: 0.014%, 1.4% and 5.6% which, in the case of RS gravitons, correspond to a k/M_{Pl} of 0.01, 0.1, 0.2 respectively. The trigger reconstruction and selections are simulated in these samples and the double photon trigger used in the analysis is found to be fully efficient for signal events at all masses (Figure 4.1).

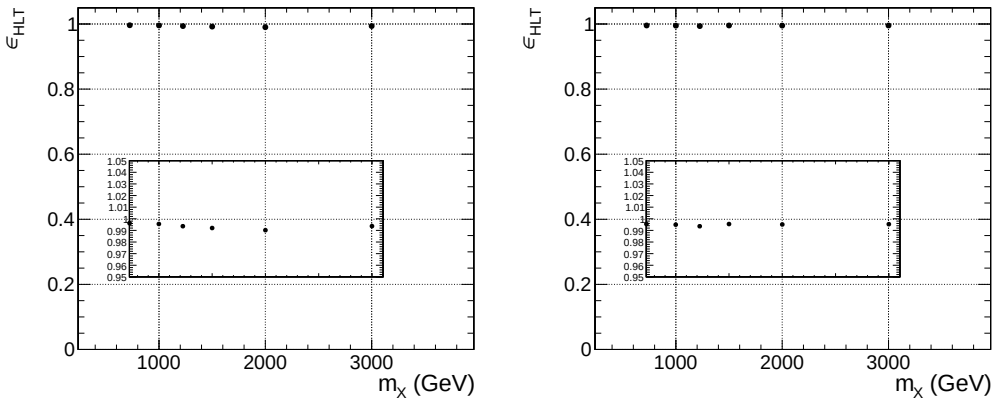

Figure 4.1: HLT trigger selection efficiency as a function of the simulated resonance mass. Only events where the two photons are in the detector acceptance are considered. The left (right) plot refers to events in the EBEB (EBEE) category (see Section 4.4.2). The inner pads are a zoom on the y-axis of the outer histograms.

4.3.2 Standard model diphoton production simulation

The continous background produced by the SM non-resonant diphoton production and the QCD induced $\gamma + jet$ and $jet + jet$ processes are measured with a parametric fit to the data (see Section 4.6.2). Thus no simulation of the background processes is used to derive the analysis results. However a set of QCD induced $\gamma + jet$ events generated with PYTHIA8 is used to optimize the photon identification selections. The events are produced in several invariant mass bins up to 6 TeV in order to have a significant amount of photons and jets over the whole p_T spectrum.

4.3.3 Drell-Yan production of electron-positron pairs

Finally a set of Drell-Yan events ($Z \to e^+e^-$) is generated with aMC@NLO [46] and is used to derive data to simulation scale factors for the selections efficiency. This sample is generated as a pure, unphysical, set of Z boson decays, neglecting the interference with the photon.

4.4 Events selection

Two measurements are needed to build the invariant mass of the diphoton system: the energy of the photons and the position of the primary interaction. The former is performed with the ECAL as described in Section 3.1 while the latter is reconstructed with tracks produced in the hard scattering against which the diphoton system recoils. Additional information from the tracker and the HCAL are used to discriminate genuine photon candidates from QCD jets. In the following paragraphs the vertex and photon identification algorithms are presented.

4.4.1 Vertex identification

The standard CMS reconstruction identifies the primary interaction vertex (PV) as the one that as the largest Σp_T^2 within each bunch crossing. Only charged particles with $p_T > 0.9$ GeV and used to determine the vertex position included in the sum. The method is not fully efficient for diphoton events since the two neutral particles carry a significant amount of the transverse energy. A dedicated boosted decision tree regression has been trained in the context of the search for the Higgs boson decaying into two photons [47]. Inputs to the regression are the Σp_T^2 and other quantities related to the p_T balance between the diphoton system and the charged particles. Using this method the interaction vertex is correctly assigned for about 90% of the signal events.

4.4.2 Kinematic selections and event categorization

Photons candidates are reconstructed from energy deposits in the ECAL with no associated track. A set of kinematic selections are applied to avoid detector inefficiencies and shaping of the mass spectrum due to trigger level selections:

- The transverse momentum of each candidate greater than 75 GeV.
- The absolute value of the pseudorapidity of the supercluster ($|\eta_{SC}|$) of both candidates is required to be below $|\eta_{SC}| < 2.5$ and not between $1.4442 < |\eta_{SC}| < 1.566$, due to the geometric acceptance of the ECAL. Photons in the region $2.5 < |\eta| < 3.0$ are still detected by the ECAL but the absence of tracker coverage limits the discrimination power between photons and jets. Furthermore signal photons are more likely to be produced in the central region of the detector.
- To avoid a distortion of the background shape due to the transverse momentum cut, the minimum invariant mass of the diphoton pair has to be 230 GeV, when both photons are detected in the ECAL barrel region (EB, $|\eta_{SC}| < 1.4442$). If one photon candidate is detected in the endcap region (EE, $|\eta_{SC}| > 1.566$), the minimum invariant mass has to be 330 GeV.

If more then one pair of photons satisfies the kinematic selection (1% of all the events) the one with the highest scalar sum of the photons transverse momenta ($p_T^{\gamma\gamma}$) is chosen.

The events are split into two categories accordingly to the topology of the photon system in relation to the ECAL segmentation:

- barrel-barrel (EBEB): both photons are detected in the ECAL barrel region $|\eta_{SC}| < 1.4442$.
- barrel-endcap (EBEE): one photon is detected in the ECAL barrel region $|\eta_{SC}| < 1.4442$ and the other in one of the endcaps $1.566 < |\eta_{SC}| < 2.5$.

The EEEE category (both photons detected in the endcaps regions) is not considered for the analysis since only few percent of the benchmark signal events fall in this category and conversely the SM background is considerably higher than in the other categories.

4.4.3 Photon identification

Energetic neutral pions contained in QCD jets have a signature similar to that of a photon since they decay into two collimated photons. A dedicated set of selections is applied to each photon candidate in the analysis to select a pure sample of diphoton events. These criteria were optimized for photons with transverse momentum in the range $100 - 3000$ GeV and based on the following variables:

- Iso_{Ch}: the scalar sum of the transverse momenta of the particle flow charged hadron candidates (see Section 2.3.5) , which are assigned to the chosen primary vertex. Only candidate within a radius of $\Delta\text{R} < 0.3$ from the photon in the η - ϕ plane, which is defined as:

$$\Delta\text{R} = \sqrt{(\eta_\gamma - \eta_{cand})^2 + (\phi_\gamma - \phi_{cand})^2}$$

  are considered.

- Iso_γ: the scalar sum of the transverse energies of the particle flow photon candidates for which $\Delta\text{R} < 0.3$.

- H/E: ratio of the energy measured in the HCAL and ECAL.

- $\sigma_{i\eta i\eta}$: the weighted spatial second order moment of the photon candidate in the η-direction, computed as:

$$\sigma_{i\eta i\eta} = \sqrt{\frac{\sum_{i\in 5\times 5} (\eta_i - \bar{\eta})^2 w_i}{\sum_{i\in 5\times 5} w_i}}, \qquad w_i = \max(0, 4.7 + \log(E_i/E_{5\times 5}))$$

- R_9: the ratio of the energy contained in a 3×3 matrix around the most energetic crystal over the energy of the supercluster:

$$R_9 = \frac{E_{3\times 3}}{E_{SC}}$$

- Conversion safe electron veto, to reject electrons. The algorithm checks the compatibility of the ECAL supercluster associated to the photon candidate and a track with at least two hits in the three tracker pixel layers and compatible with the primary interaction vertex. If no track with such characteristics is found the candidate is likely to be a photon. The algorithm also check for the presence of two tracks spatially compatible with the ECAL supercluster and originated from a displaced vertex inside the tracker volume. Candidates with these requirements are kept since compatible with a electron-positron system originate by a converted photon.

Particle flow charged particles or photons sharing part of their energy with the photon candidates are excluded from the Iso_{Ch} and Iso_γ sum.

The selection values are reported in the following table:

For very energetic photons the ECAL readout electronics can saturate. In such a case the shower shape variable $\sigma_{i\eta i\eta}$ is distorted, hence a different selection value is set for

photon category	Iso_{Ch} (GeV)	Iso_γ^{corr} (GeV)	H/E	$\sigma_{i\eta i\eta}$	R_9
$\eta_{SC} < 1.4442$ non-sat.	< 5	< 2.75	$< 5 \times 10^{-2}$	< 0.0105	> 0.8
$\eta_{SC} < 1.4442$ sat.	< 5	< 2.75	$< 5 \times 10^{-2}$	< 0.0112	> 0.8
$\eta_{SC} > 1.566$ non-sat.	< 5	< 2.0	$< 5 \times 10^{-2}$	< 0.028	> 0.8
$\eta_{SC} > 1.566$ sat.	< 5	< 2.0	$< 5 \times 10^{-2}$	< 0.030	> 0.8
conversion-safe electron veto applied for all categories					

Table 4.1: Photon identification criteria used in the analysis. Iso_γ^{corr} is the corrected Iso_γ value described at the end of this section.

this identification variable in case of saturation in order to mantain the same efficiency on signal photons and ensure a smooth description of the signal shape and normalization obtained from simulation (in which the saturation effect is fully simulated).

The thresholds of the identification variables were optimized to give an efficiency flat as a function of the mass of the diphoton pair, the chosen working point corresponds to an efficiency of 90(87)% for photons in the EB(EE). The Iso_γ distribution is found to depend on the event pile-up and the p_T of the photon candidate (Figure 4.2). The p_T dependency comes from inefficiency in the ECAL clustering algorithm: part of the photon energy is deposited in crystals which are not collected by the clustering. This effect is negligible compared to noise fluctuation for low energy photons while becomes relevant as energy increases These dependencies leads to a variation of the selection efficiency with time and also for different values of $m_{\gamma\gamma}$. In order to keep a flat efficiency an effective correction is used, its expression is:

$$\text{Iso}_\gamma^{corr} = \text{Iso}_\gamma - \kappa \cdot p_T - A \cdot \rho + \alpha$$

where p_T is the transverse momentum of the photon candidate, ρ is the event pile-up energy density. The pile-up energy density is the median of the $\Sigma p_T/(\Delta\eta \times \Delta\phi$ distribution computed in 324 $\eta - \phi$ bins between $-5.1 < \eta < 5.1$, the sum of the transverse momenta includes all particles reconstructed by the particle-flow algorithm with $p_T > 0.7$ GeV. The values of A and κ are chosen such to keep the 90% quantile of the distribution at a constant value as a function of ρ and p_T, while the α parameter is used to adjust the distribution such that the bulk of the corrected isolation distribution for signal photons peaks at zero. The use of a scale parameter is arbitrary and those not affect the performance of the analysis but provide a way to simply understand the the corrected distribution: photons with negative corrected isolation values are those recorded in events with a lower than average pileup while those with a positive vales are recorded in events with larger than average pileup (Figure 4.3).

The values of the correction parameters are reported in Table 4.2, A is derived in five bins of $|\eta|$ while two bins (barrel and endcaps) are sufficient for κ and α to fully correct the ρ and p_T dependency of Iso_γ.

region	α (GeV)	A	κ (1/GeV)
$\eta_{SC} < 0.9$	0.99	0.15	1.6×10^{-3}
$0.9 < \eta_{SC} < 1.4442$	0.99	0.13	1.6×10^{-3}
$1.566 < \eta_{SC} < 2.0$	1.52	0.093	0.75×10^{-3}
$2.0 < \eta_{SC} < 2.2$	1.52	0.15	0.75×10^{-3}
$2.2 < \eta_{SC} < 2.5$	1.52	0.21	0.75×10^{-3}

Table 4.2: Corrections factors for the Iso_γ variable.

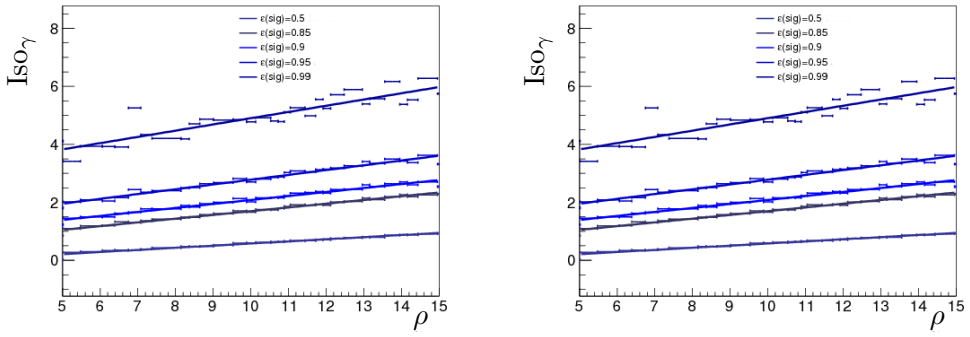

Figure 4.2: Iso$_\gamma$ quantile distribution as a function of the pile-up energy density for candidates in the EB (left) and EE (right). The lines are fit to the points and are used to derive the correction described in the text. The slope at the 0.9 quantile is steeper than the one of the median, thus the need of the scale parameter α

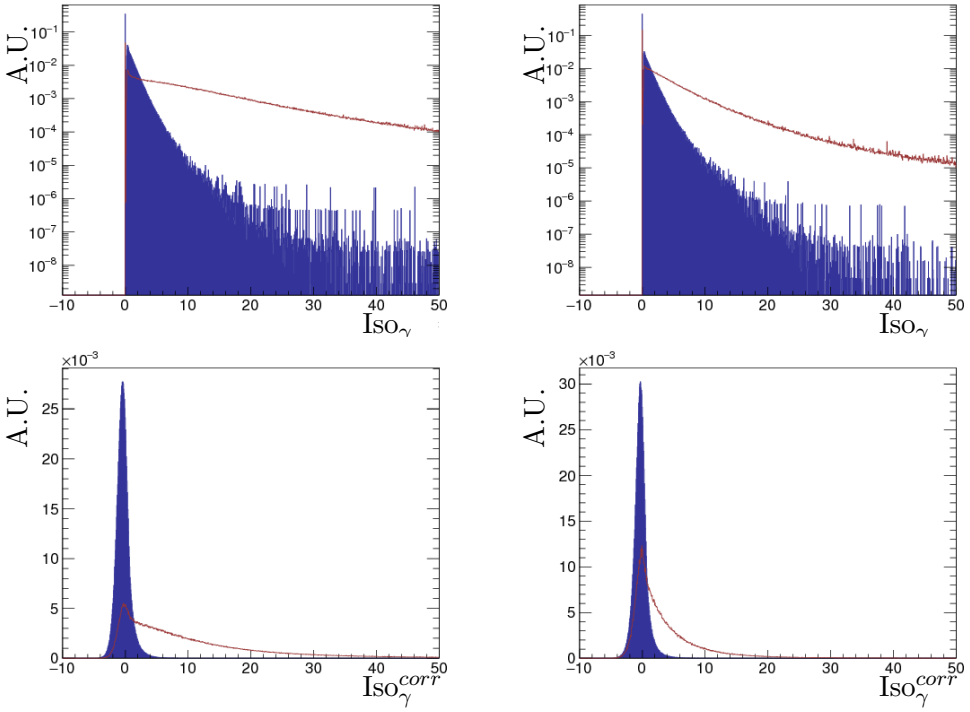

Figure 4.3: Iso$_\gamma$ distribtions for generator level matched photons (blue) and jets (red) before (top) and after (bottom) the correction described in the text. Candidates in the barrel are shown on the left while those in the endcap are shown on the right.

4.4.4 Selection efficiency measurement

The efficiency of the photon identification described in the previous chapter is measured in data using the Z $\to e^+e^-$ control sample. The measurement of the selection efficiency in data is then compared to the one measured in the simulation and in case of discrepancy the signal normalization derived from the simulation is corrected for the measured scale factor.

The efficiency is measured with a tag-and-probe technique exploiting the well known Z

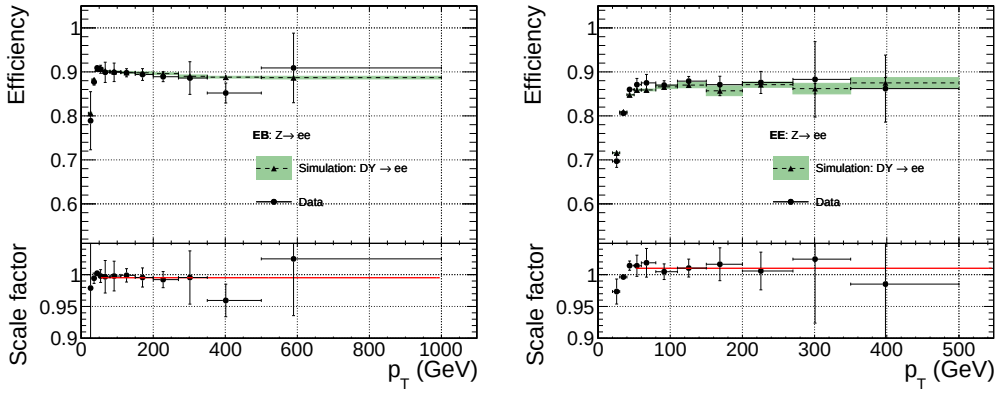

Figure 4.4: Efficiency measurement with Z $\rightarrow e^+e^-$ events for electrons in the EB (left) and in the EE (right). The error bars on the data points account for the uncertainty originated from the choice of the fit model as described in the text. The bottom panels show the ratio between the efficiencies measured in data and simulation, the scale factor is compatible with unity within the uncertainties.

decay to electrons. For this study the response of the ECAL and HCAL is assumed to be identical for electrons and photons. The tag-and-probe method is used both for the data and simulation measurement, the Z $\rightarrow e^+e^-$ control sample in data is selected using events recorded with a single electron trigger (as described in Section 4.2). Dielectron candidates are further filtered with an invariant mass selection ($70 < m_{e^-e^+} < 110$ GeV) centered around the Z mass peak, the invariant mass window is applied also to the simulated events.

The method then requires one of the two electrons (the "tag") coming from the Z boson to pass a very tight selection which has an efficiency of 70%. The second electron is required to pass a loose identification and is assumed to be unbiased with respect the variables being studied (the "probe"). The photon selection efficiency is studied using this unbiased sample inverting the electron veto request. The efficiency is studied as a function of the probe electron p_T.

The data events are fitted simultaneously for passing and failing probes with a signal plus background model. The signal is modeled by the Z lineshape convolved with a Gaussian, while the background is modeled by an exponential function. The Z linashape is obtained from the simulation without considering detector effects. As the choice of the fit model is one of the dominating systematics, different models were studied to assess it. A simple cut-and-count method is applied for the simulation sample since the non resonant $pp \rightarrow \gamma^* \rightarrow e^+e^-$ events can be discarded with MC truth information and are anyway not simulated in the sample used for this analysis.

The efficiency measurement is summarized in Figure 4.4: a good agreement between data and simulation is observed across the whole probe electron p_T spectrum and both for probes in the ECAL barrel and endcaps, thus no scale factor is applied to the predicted signal yield while a systematic uncertainty of 6% on the signal normalization is set for both the analysis categories to account for the error in the efficiency measurements.

4.5 Photon energy scale and resolution corrections

The detector response is simulated with fixed pile-up distribution, detector noise and transparency loss. The pile-up distribution is weighted to match the one in data. The detector noise and crystal transparency instead varies over the data-taking period and so a discrepancy in the energy response of the ECAL may arise between data and simulation since in the latter no time evolution of the detector conditions is simulated. The effect of this discrepancy translate in shift of the energy scale in data with respect to the MC simulation (as described in Section 3.3.3), furthermore any residual mis-calibration of the detector is not simulated and thus the energy resolution in data is worse than in the MC simulation. These two effects are corrected on one hand by scaling the photon energy in data events to correct the time dependent energy scale variations (see Section 3.3.3) and match the energy scale of the simulation and, on the other hand, by smearing the energy in simulated events to match the resolution observed in data.

The time-dependent scale corrections and the smearing are derived from the Z $\rightarrow e^+e^-$ control sample. Again since the energy for both photons and electrons is primarily reconstructed from the ECAL, electrons are used as a proxy of photons. The reader may notice that the energy reconstruction formula outlined in Equation 3.1 differs for electrons and photons in the supercluster energy correction term ($F_{e,\gamma}$). Electrons used to derive the corrections described in this section are reconstructed the electron F_e correction, while both electrons used in the final data to simulation comparison and photons selected for the analysis are reconstructed with the F_γ correction factor.

The corrections are derived in two steps: in the first, the energy scale is corrected by adjusting the scale in data to match the simulation prediction. The Z $\rightarrow e^+e^-$ invariant mass peak is fitted with a Breit-Wigner function convolved with a crystal ball (CB) function describing, respectively, the theoretical signal line shape of the Z-boson and the detector response. The parameters of the Breit-Wigner function for the Z boson are taken from the Particle Data Group (PDG) [4]: $m_Z = 91.1876$ GeV and $\Gamma_Z = 2.4952$ GeV. By fitting the distribution in data and MC simulation separately, the energy scale offset can be extracted.

Different systematic behaviors of the mean of the CB function (Δ_m) as a function of time and the pseudorapidity can be observed. As a result, run dependent energy corrections are necessary to correct for the energy scale variations during data-taking. The energy scale correction (ΔP) is defined as the relative shift in mass between data and MC prediction:

$$\Delta P = \frac{\Delta m_{data} - \Delta m_{simulation}}{m_Z}$$

After the ΔP correction is applied, a stable behavior of Δm over time within 0.1 GeV is observed.

In the second step, the residual difference between the observed and predicted electron energy is assessed by maximizing the likelihood between the smeared MC distribution and the data.

The smearing of the MC distribution is performed by multiplying E_{SC} distribution by a Gaussian distribution, centered at $1 + \Delta P$ and with resolution ΔC. The resolution ΔC denotes the additional constant term of the energy resolution which is added to the MC prediction.

The additional constant term needed to match the energy resolution measured with data varies as a function of η_{SC}, as the scale correction, but it also different between electrons that showers in the tracker volume and those that don't. The R_9 variable is

used to discriminate between showering and non-showering electrons: this variables is used instead of others since can also be applied to discriminate between converted and un-converted photons and so is suitable to maintain the analogy between the analysis object (photons) and the control sample ones (electrons). Thus, a maximum likelihood fit is performed in eight categories: four η_{SC} regions times two R_9 categories.

The comparison between the predicted and observed dielectron invariant mass spectra around the Z boson peak, for events passing the analysis selection (with inverted electron veto) and after all energy corrections have been applied is reported if Figure 4.5.

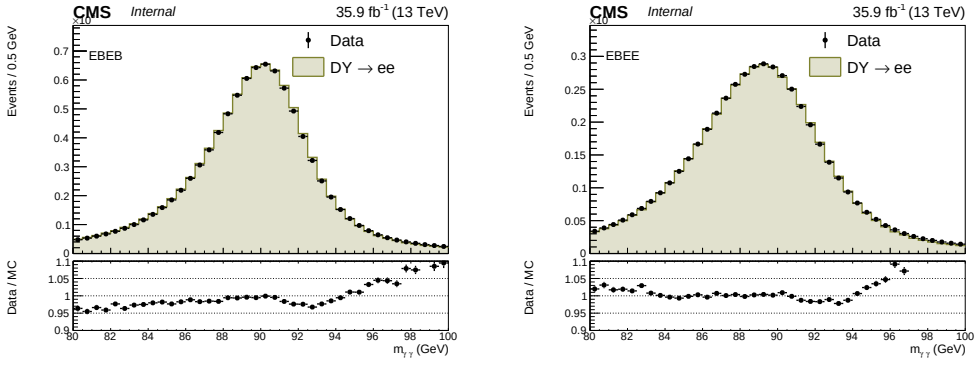

Figure 4.5: Comparison between predicted (shaded histogram) and observed (points) invariant mass distribution of electron pairs obtained after the application of energy scale and resolution corrections. The left figure refers to events where both electrons are detected in the ECAL barrel while the right one to events with one of the two electrons detected in the EB and the other in the EE. The simulation distribution is scaled to match the integrated luminosity of the data. The discrepancy in the right tail of both plots comes from the fact that the simulation does not include the non resonant Drell-Yan dielectron production and its interference with the Z boson.

Finally the linearity of the ECAL energy response is studied using Z bosons with high transverse momentum decaying to electrons. This technique allows to test the linearity for transverse energies up to 150(100) GeV in the EB(EE) region. The linearity of the response is assessed by comparing the peak position of the reconstructed Z mass measured in data and simulation as a function of $H_T = E_{T_1}^2 + E_{T_1}^2$, where $E_{T_{1,2}}^2$ are the transverse energies of the two electrons, a linear fit to the data is performed in order extrapolate the scale variation to the energy range of the analysis. The results are reported Figure 4.6, both the central value of the fit and the statistical uncertainty are shown for the four $\eta \times R_9$ categories. Only $Z \rightarrow e^+e^-$ events in which both electrons belongs to the same category are considered for the response linearity measurement.

For electrons detected in the barrel part of the detector, the corrected energy scale is found to be stable within 0.5% during the data-taking period. Electrons detected in the endcap region of the detector are found to provide a stability of better than 0.8%. These figures dominates at low masses while the ECAL response linearity is the main source of uncertainty on the mass measurement for $m_{\gamma\gamma} > 1$ TeV. Since all the uncertainty on the energy scale are below 1% up to $m_{\gamma\gamma} = 2$ TeV, the final uncertainty on the energy scale stability is estimated to be 1% for both barrel and endcap photons. The smearing terms applied to the simulation in order to match the resolution observed in data are reported in Table 4.3. The additional constant term on the energy resolution varies from 0.96% for non-showering electrons in the barrel to 2.61% for showering electrons in the forward region.

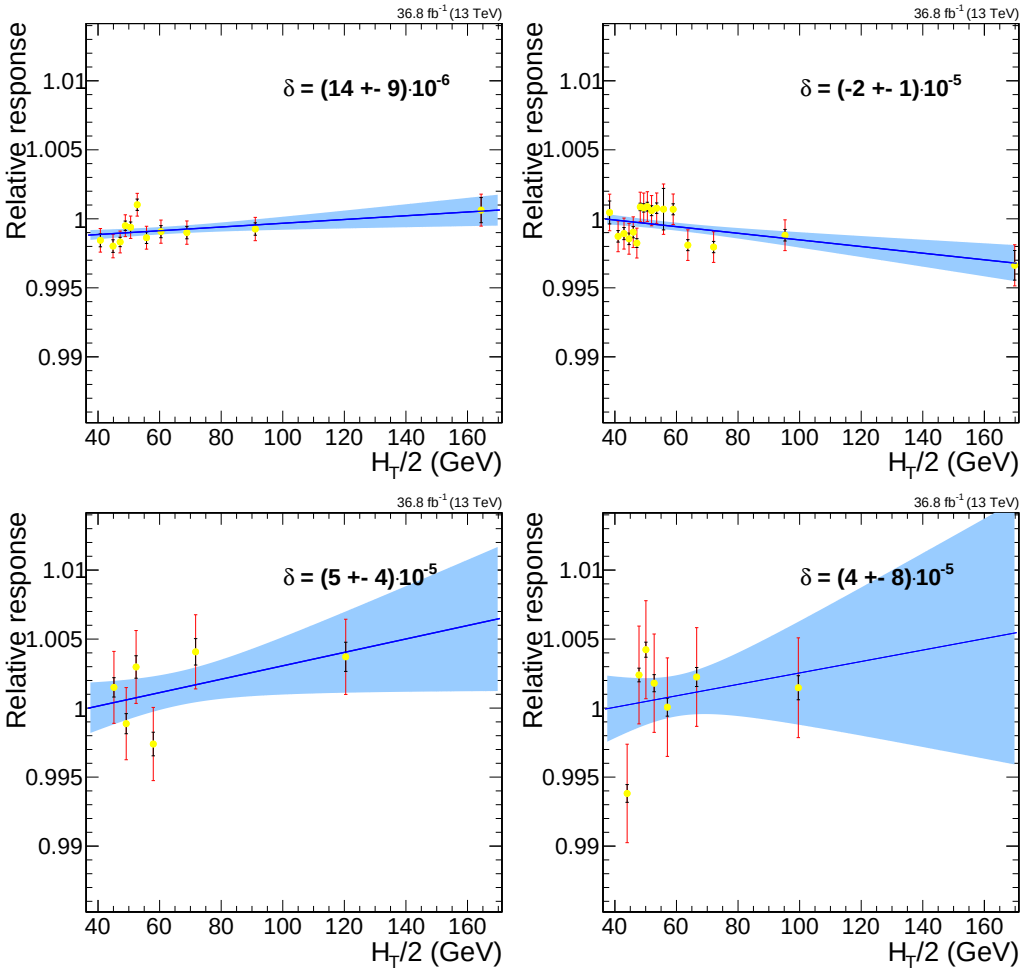

Figure 4.6: Linearity of the ECAL response measured with Z $\rightarrow e^+e^-$ events. The response stability is evaluated separatelly for barrel (top) and endcap (bottom) electrons and in the two R_9 bins discussed in the text ($R_9 < 0.94$ left, $R_9 > 0.94$ right).

Category	ΔC[%]	Δ_{stat}C[%]
$\|\eta\| < 1$ $R9 > 0.94$	0.96	0.07
$\|\eta\| < 1$ $R9 < 0.94$	1.03	0.11
$1 < \|\eta\| < 1.5$ $R9 > 0.94$	1.36	0.14
$1 < \|\eta\| < 1.5$ $R9 < 0.94$	1.82	0.05
$1.5 < \|\eta\| < 2$ $R9 > 0.94$	1.91	0.07
$1.5 < \|\eta\| < 2$ $R9 < 0.94$	2.20	0.13
$\|\eta\| > 2$ $R9 > 0.94$	2.53	0.13
$\|\eta\| > 2$ $R9 < 0.94$	2.61	0.10

Table 4.3: Smearing values with uncertainty applied to the simulation in order to match the resolution measured in data. The values are extracted with the procedure described in the text and the uncertainties are of statistical nature and comes from results of the fit.

4.6 Statistical interpretation of the observed $m_{\gamma\gamma}$ spectrum

This section presents the statistical technique used to interpret the analysis results. The goal of the statistical analysis is to define a compatibility between the observed dataset with the predicted standard model only and standard model background plus signal hypotheses. Where no deviation from the standard model prediction is found, the results are interpreted in terms of modified frequentist upper limits on the signal process cross-section.

First the signal plus background maximum likelihood fit to data is presented, then the signal and background model derivations are described. The last part of the chapter is dedicated to the presentation of the results of the hypothesis test.

4.6.1 Signal plus background maximum likelihood fit to data

A test statistic is built in order to test the different signal hypothesis, the underling likelihood is defined as:

$$L(\mu,\theta) = \prod_{i\in Events} \Big[\mu \cdot S(m^i_{\gamma\gamma}|\theta_S) + B(m^i_{\gamma\gamma}|\theta_B)\Big] \cdot Poisson(N_{events}|N_B + \mu \cdot N_S) \quad (4.1)$$

In this formula, S and B denote the signal and standard model background shape respectively. Both models are $p.d.f$ that depends on $m_{\gamma\gamma}$ and on nuisance parameters (θ) that represent the systematic uncertainties.

The selected events are split in two categories as described in Section 4.4.2. Thus two different likelihoods are built: each category has different nuisance parameters, signal and background shapes, while the signal strength μ is a common parameter. A simultaneous fit to the data in the two category is performed.

4.6.2 Background parametrization

The background parametrization is extracted from a fit to the data performed separately for the two analysis categories. The fit is performed assuming the absence of any signal, so the signal strength μ is set to zero in the likelihood 4.1. The choice of a data-driven technique to define the background shape eliminates the need of high order QCD calculation for simulated samples and also a precise knowledge of the ratio between the different components of the background.

A parametric form is chosen out of an arbitrary set of possible function. To ensure that the particular choice of the functional form does not introduce any biases in the background shape prediction, the accuracy of the chosen function is evaluated with the following procedure:

- An ansatz functional form, $g(m_{\gamma\gamma})$, is chosen for the background parametrization.
- The corresponding true underlying distribution, $h(m_{\gamma\gamma})$ is constructed fitting the data events with an alternative functional form.
- Unbinned toy experiments t_i, corresponding to number of events which are expected on data for 35.9 $\text{fb}^{-1}$are extracted from $h(m_{\gamma\gamma})$.
- An unbinned maximum likelihood fit is performed to each of the toy experiments using the chosen functional form $g(m_{\gamma\gamma})$, to obtain $\hat{g}_i(m_{\gamma\gamma})$.
- The number of events predicted by $\hat{g}_i(m_{\gamma\gamma})$ is compared with $h(m_{\gamma\gamma})$ in several mass windows w_j and the pull test statistics is constructed as:

$$p_i^j = \frac{N_{\hat{g}_i}^{w_j} - N_h^{w_j}}{\sigma(N_{\hat{g}_i}^{w_j})}$$

  where $\sigma(N_{\hat{g}_i}^{w_j})$ is the statistical uncertainty on $N_{\hat{g}_i}^{w_j}$ and accounts for both normalization and shape uncertainties on $\hat{g}_i$.
- The procedure is repeated with several alternative functional and for both EBEB and EBEE category separately.

The chosen background parametrization has the form:

$$g(m_{\gamma\gamma}) = m_{\gamma\gamma}^{a+b\cdot log(m_{\gamma\gamma})} \tag{4.2}$$

This parametrization is found to have the least bias among the whole invariant mass spectrum. The a and b coefficients maximized by a likelihood fit of $m_{\gamma\gamma}$ in data, for each event category and each dataset separately. The coefficients entered the hypotheses tests as unconstrained nuisance parameters and are of statistical nature. The background only fit to the data in the two event categories is shown in Figure 4.7.

A representative set of alternative functions, used to evaluate the accuracy of the chosen parametrization, is selected within the set of families shown in Table 4.4. First, for a given family, the lowest order function in that family is fit to a single category. Then, the next highest order function is fit to the data in the same category and the difference $2\Delta NLL_{N+1} = 2(NLL_{N+1} - NLL_N)$ indicates whether or not the data support the hypothesis of the higher order function. This is quantitatively expressed using the fact that $2\Delta NLL_{N+1}$ should be distributed as a χ^2 with M degrees of freedom where M

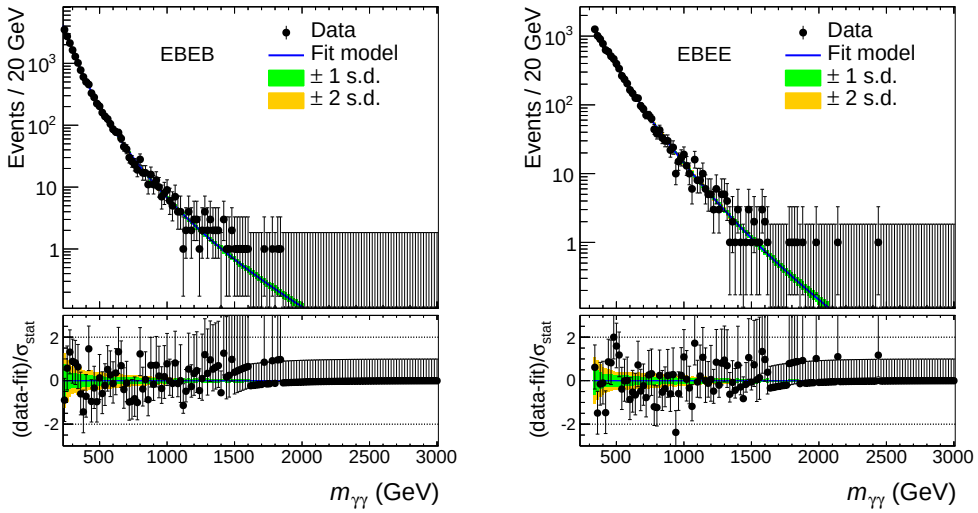

Figure 4.7: Observed mass spectrum in the EBEB (left) and EBEE (right) categories. The result of the parametric fit is superimposed to the points, together with bands representing the statistical uncertainties on the knowledge of the background shape.

is the difference in the number of free parameters in the N + 1 function and N function. For example, for exponentials, $M = 4 - 2 = 2$, while for the polynomials $M = 3 - 2 = 1$. A p-value is then calculated as

$$\text{p-value} = p(2\Delta NLL > 2\Delta NLL_{N+1} | \chi^2(M)).$$

Family label	Functional form	EBEB chosen order	EBEE chosen order
Pow	$p(m_{\gamma\gamma})^a$	4	4
Expow	$e^{p(m_{\gamma\gamma})} \times m_{\gamma\gamma}^a$	2	2
Invpow	$(1 - p(m_{\gamma\gamma}))^a$	1	2
Invpowlin	$(1 - m_{\gamma\gamma})^{p(m_{\gamma\gamma})}$	1	1
Moddijet	$m_{\gamma\gamma}^{a+b\cdot log(m_{\gamma\gamma})} \times p(1 - m_{\gamma\gamma})^c$	1	3

Table 4.4: List of truth models chosen for the bias determination and the order selected within the family for the two categories. $p(m_{\gamma\gamma})$ represents the polynomial and the order is the order of the $p(m_{\gamma\gamma})$ polynomial.

If the p-value is less than 0.05, the higher order function is supported by the data, meaning it is included in the list of functions, and the procedure continues, testing the next (N = 3) order function in the family. If however, the p-value is more than 0.05, the higher order function is assumed too flexible given the data and the procedure terminates having found the highest order suitable function. An additional constraint is applied to remove low order functions which do not fit the data well.

A set of intervals in $m_{\gamma\gamma}$, w_j, is chosen as test regions and the parametrization $g(m_{\gamma\gamma})$ is considered accurate if, for all the windows j, the following relation holds:

$$b^j = |median\left(p_i^j\right)| < 0.5 \tag{4.3}$$

Choosing a threshold of 0.5 for b^j is equivalent to allowing the uncertainty on the mean number of estimated background events to be underestimated by at most 10%.

If the criterion from Eq. 4.3 is not met for, the pull test statistics is modified as follows:

$$\tilde{p}_j^i = \frac{N_{\hat{g}_i}^{w_j} - N_h^{w_j}}{\sqrt{\sigma^2(N_{\hat{g}_i}^{w_j}) + \beta_I^2(w_j)}} \tag{4.4}$$

Where $\beta_I(w_j) = \int_{w_j} \beta(m_{\gamma\gamma})$ represent an additional uncertainty ("bias term") that is assigned additionally to the model. The bias criterion can then be modified exchanging p with $\tilde{p}$.

$$\tilde{b}^j = |median\left(\tilde{p}_i^j\right)| < 0.5 \tag{4.5}$$

The set of test regions used in the study is reported in Tab. 4.5

$m_{\gamma\gamma}$ min (GeV)	$m_{\gamma\gamma}$ max (GeV)	$m_{\gamma\gamma}$ min (GeV)	$m_{\gamma\gamma}$ max (GeV)
500	550	900	1000
550	600	1000	1200
600	650	1200	1800
650	700	1800	2500
700	750	2500	3500
750	800	3500	4500
800	900	4500	5500

Table 4.5: List of test regions considered for the bias determination.

The modified bias criterion is met for all $m_{\gamma\gamma}$ spectrum variations and all sets of test region using the β function reported in Table 4.6 and depicted in Figure 4.8.

category	$m_{\gamma\gamma}$ range	$\beta(m_{\gamma\gamma})/GeV)$
EBEB	$230 < m_{\gamma\gamma} < 650$ GeV	0.125
EBEB	$m_{\gamma\gamma} > 650$ GeV	$m_{\gamma\gamma}^{(2.0-0.36\times log(m_{\gamma\gamma}))}$
EBEE	$330 < m_{\gamma\gamma} < 750$ GeV	0.2
EBEE	$m_{\gamma\gamma} > 750$ GeV	$\left(\frac{m_{\gamma\gamma}}{600\text{GeV}}\right)^{-3.5-0.2\times log(x)} + 1.5 \times 10^{-4}$

Table 4.6: Bias parametrization, β, divided by the integrated luminosity for the two analysis categories.

The b and $\tilde{b}$ values of the default test region of Table 4.5 can be found in Figure 4.9 for the EBEB category and Figure 4.10 for the EBEE category, respectively.

The size of the background mismodeling enters the hypothesis test as the only systematic uncertainty on the background model. The shape of this additional bias is assumed to have a similar form as the signal PDF (S($m_{\gamma\gamma}$)) with a normalization constrained by a Gaussian of mean zero and width equal to the size of the bias ($Norm(\theta_\beta)$). It is added to the background description via the following equation in which $N_{bkg}(N_\beta)$ are the number of background (bias) events:

$$\tilde{B}(m_{\gamma\gamma}|\theta_\beta) \cdot Pdf(\theta_\beta) = \left(\frac{N_{bkg} - \theta_\beta N_\beta(m_{\gamma\gamma}, sig)}{N_{bkg}} B(m_{\gamma\gamma}) + \frac{\theta_\beta N_\beta(m_{\gamma\gamma}, sig)}{N_{bkg}} S(m_{\gamma\gamma})\right) \cdot Norm(\theta_\beta) \tag{4.6}$$

Where $N_\beta(m_{\gamma\gamma}, sig) = \int \beta(m_{\gamma\gamma}) \cdot S(m_{\gamma\gamma}) \sim \beta(m_G) \cdot FWHM(sig)$, $S(m_{\gamma\gamma})$ is the signal PDF and $Norm(x)$ is the normal distribution.

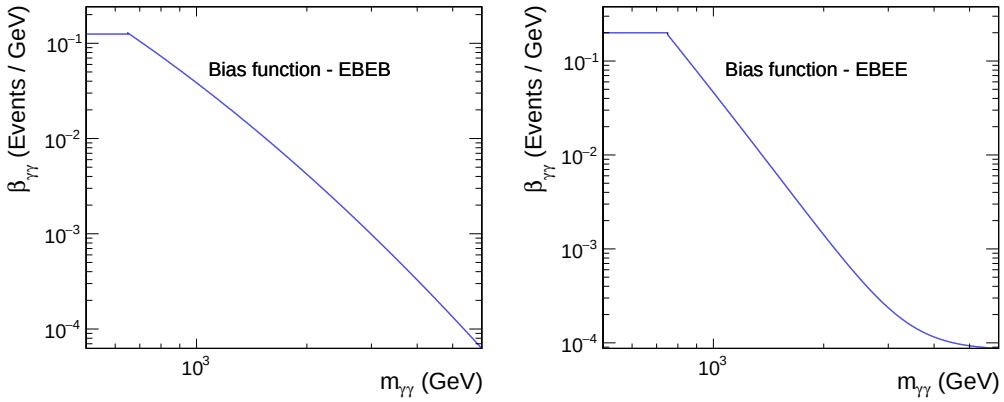

Figure 4.8: The bias parametrization, β Left and right plots show the EBEB and EBEE categories respectively.

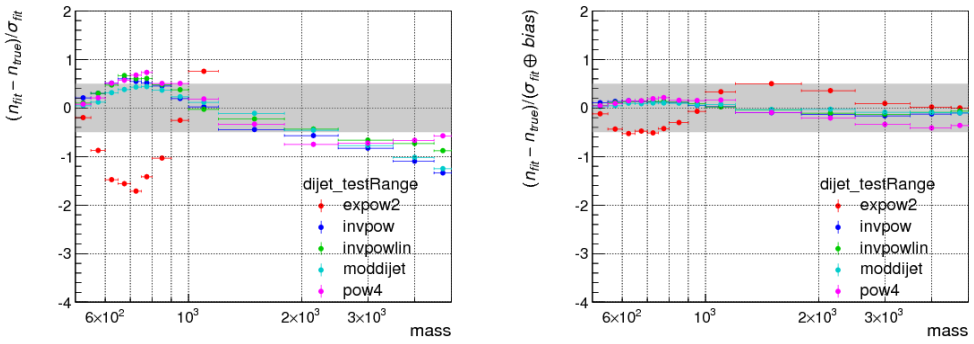

Figure 4.9: Median of the pull p and modified pull $\tilde{p}$ for all considered test regions according to Tab. 4.5 for EBEB. Different datasets correspond to different truth models as specified in the text.

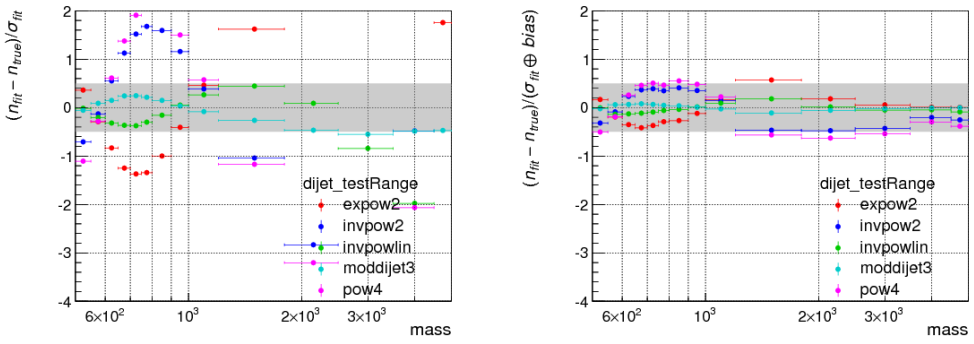

Figure 4.10: Median of the pull p and modified pull $\tilde{p}$ for all considered test regions according to Tab. 4.5 for EBEE. Different datasets correspond to different truth models as specified in the text.

4.6.3 Signal model

In order to statistically interpret the data, it is necessary to have a description of both the signal shape of the diphoton mass distribution and its normalization as a function of the predicted signal mass. The signal shapes, which are mainly dominated by the detector and reconstruction response in the ECAL, need to be well described in each of the two events categories.

Signal shape parametrization

This section describes the technique used to describe the shape of the resonant diphoton signal with a parametric model. The use of a parametric description of the shape allows to perform a fine scan of the investigated mass without the need of generating an infinite number of signal simulation samples.

The Monte Carlo simulation signal samples are used to build a model for the signal. The energy resolution smearing and efficiency scale factors described in Section 4.5 are applied. The strategy is to describe the simulated signal with an analytic function in which the hypothetical signal mass (m_X) represents a parameter which can vary continuously for any value in the range of interest of the search, while the width of the resonance is fixed to the three benchmarks values chosen for this analysis. The procedure is the following:

- The response distribution of the reduced mass (Δm) is computed for each mass point for which the full event simulation and reconstruction was performed. The reduced mass is computed as the difference between the reconstructed diphoton mass in the event (m_{reco}) and the true mass (m_{true}) of the event: $\Delta m = m_{reco} - m_{true}$

- In order to construct the parametric model the response distribution is fitted with an analytic function, namely a double-sided Crystal-Ball function with mean m_0, sigma σ and two asymmetric tails defined by two different different n and α parameters. The Crystal-Ball function (CB) $f_{CB}(x)$ combines a Gaussian core and a power-law tail with an exponent n to account for photon energy loss due to pair production. The parameter α defines the transition between the Gaussian and the power-law functions. In Figure 4.12 the fit to the reduced mass is shown for one of the signal mass point ($m_X = 1250$ GeV).

- The theoretical signal line shape of the X resonance is described by the functional form of a relativistic Breit-Wigner centered at m_X and with the expected natural width for a resonance of Γ_X. The Breit-Wigner distribution is fitted in this analysis with a double-sided crystal-ball. The results of the fit are shown in Figure 4.13 for $m_X = 1250$ GeV.

- The theoretical line-shape fit function is convolved with the response fit function to account for the experimental resolution of the ECAL. The convolved shape is compared with the reconstructed mass shape as a closure test of the fitting model. The closure test is shown in Figure 4.14 for $m_X = 1250$ GeV.

- The convolved model obtained in the previous step is used to throw an Asimov dataset which is fitted with a double-sided crystal-ball. This ultimate fitting model represents the final description of the mass resonance for a given mass and width. The closure test fit to the asimov dataset is shown in Figure 4.15 for $m_X = 1250$ GeV narrow width.

- The signal model derived in the previous steps depends continuously upon m_X through the parameters which describes the model itself: mean, $sigma$, $\alpha_{L/R}$, $n_{L/R}$. For each category and for each width hypothesis the trend of these parameters is studied and modelled with a polynomial function with m_X as the only independent variable. Figures 4.11 show an example fit to one of the double-sided crystal-ball parameters for the $\Gamma/m_{\gamma\gamma} = 1.4\%$ width hypothesis. The width of the Gaussian core is, among the model parameters, the one that affect the most the final results since a change in the width (i.e. better or worse resolution) directly impact the local signal over background ratio.

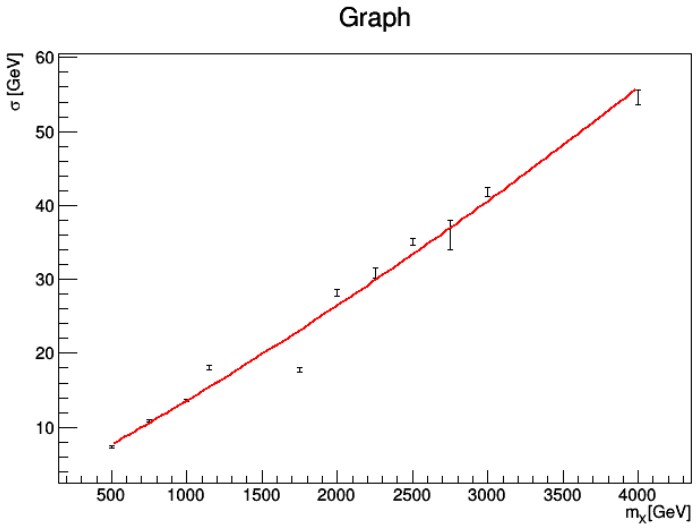

Figure 4.11: Double-sided crystal-ball σ parameter modelling as a function of m_X. The Fit is performed with a polynomial function. Only fits to the EBEB category for medium width hypothesis are shown here.

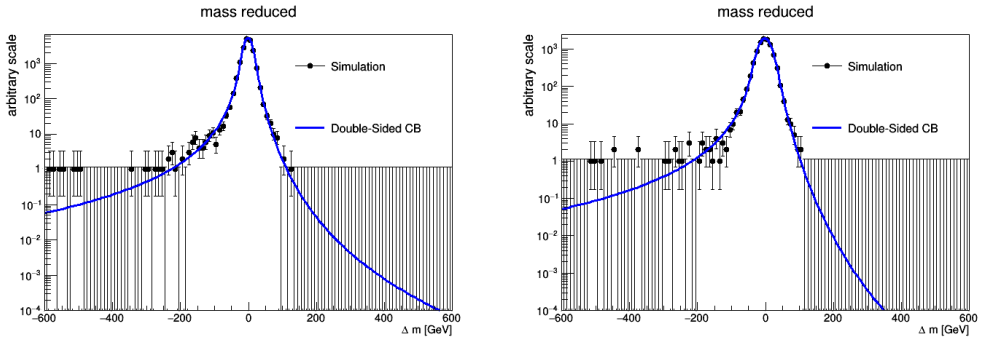

Figure 4.12: Double-sided Crystal-Ball fit (blue line) to the response distributions for $m_X = 1250$ GeV. EBEB category on the left and EBEE category on the right

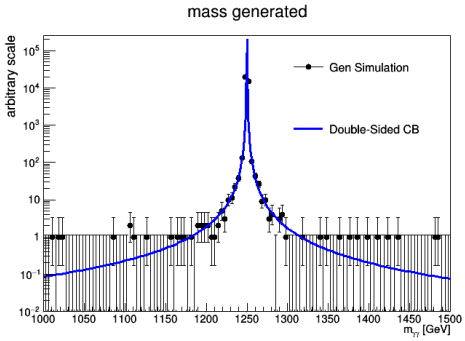

Figure 4.13: Double-sided Crystal-Ball fit (blue line) to the generator-level distributions for $m_X = 1250$ GeV narrow width hypothesis.

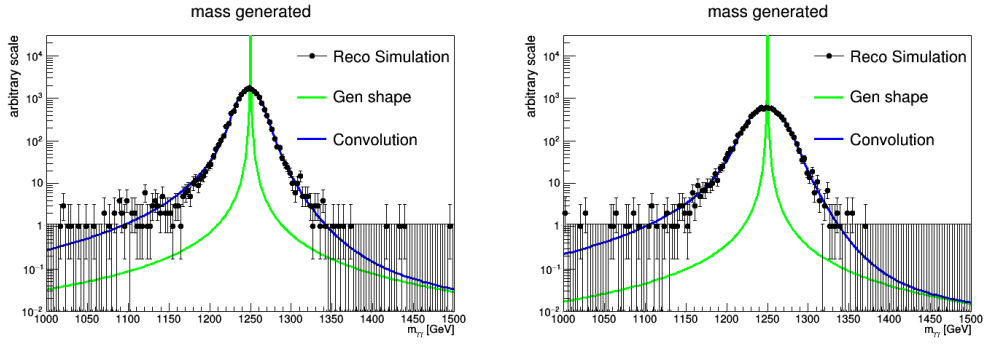

Figure 4.14: Convolved model (blue line) of the response function and the generator-level function (green line) compared to the reconstructed mass distribution for $m_X = 1250$ GeV. EBEB category on the left and EBEE category on the right.

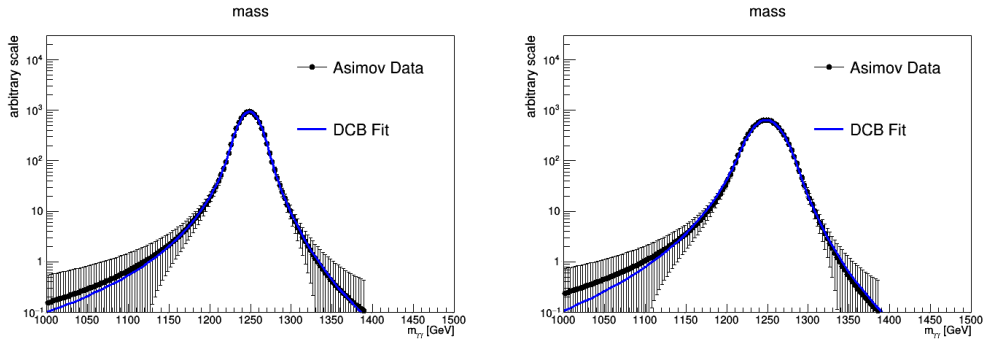

Figure 4.15: Convolved model (blue line) of the response function and the generator-level function (green line) compared to the reconstructed mass distribution for $m_X = 1250$ GeV. EBEB category on the left and EBEE category on the right.

Signal normalization

In order to determine the signal normalization, the event selection efficiency described in Section 4.4.4 is combined with the kinematic acceptance. The total combined efficiency

and acceptance ($\epsilon \times A$) for the three signal width and two spin hypotheses varies between 0.5 and 0.7 and is shown in Figure 4.17. The EBEB category has a higher sensitivity than the EBEE category and contributes to the overall $\epsilon \times A$ with more than 50% for lower m_X values and up to 85% for high m_X values. Since the diphoton selection efficiency stays flat over the $m_{\gamma\gamma}$ spectrum (Figure 4.16), any visible trends are mainly driven by the signal acceptance.

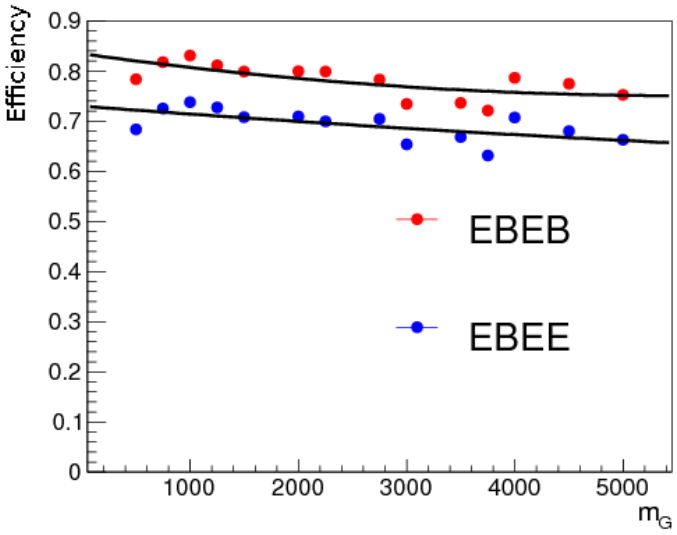

Figure 4.16: diphoton identification selection efficiency as a function of the generated resonance mass. The efficiency used in the signal model normalization is parametrized with a second order polynomial (black curve) separately for the EBEB (red) and EBEE (blue) categories.

The acceptance of the spin-0 signal model is mostly flat over the m_X spectrum, whereas for the spin-2 RS-Graviton signal it rises with larger m_X values. The angular distribution of the decay products of a spin-0 resonance is isotropic whereas that of those coming from a spin-2 one is not and one of the two photon is more likely to be produced along the beam direction. For this reason the geometric acceptance for a spin-0 signal is larger than that of a spin-2 almost at any m_X value. Only a high masses (above 4 TeV) the spin-2 is larger than that of spin-0. Spin-0 resonances can only be produced through gluon-fusion mechanism in p-p collisions while spin-2 ones can also be produced through quark-antiquark annihilation; since the gluon p.d.f decreases rapidly with the fraction of the proton momentum carried by the gluon while the quark p.d.f peaks at large momentum fraction values, for m_X values larger than 4 TeV a significant part of the spin-0 signal is produced off-shell and is rejected by kinematic selections while for spin-2 the effect is compensated by a larger production through quark-antiquark annihilation.

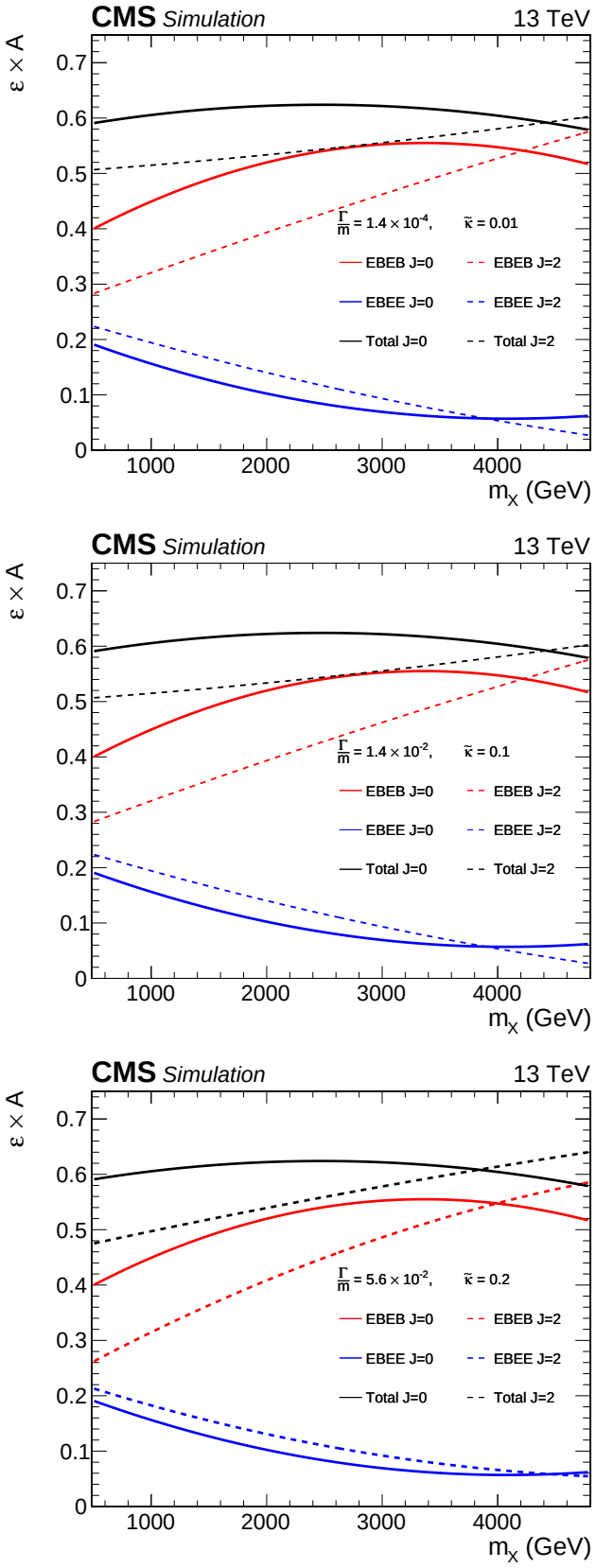

Figure 4.17: Fraction of events selected by the analysis categories for $0.5 < m_X < 4.5$ TeV for the $\Gamma_X/m_X = 1.4\times10^{-4}$ (left), $\Gamma_X/m_X = 1.4\times10^{-2}$ (center) and $\Gamma_X/m_X = 5.2\times10^{-2}$ (right) width hypotheses. Curves for both spin-0 and RS-graviton resonances are shown.

4.6.4 Sources of systematic uncertainties

Although the dominant uncertainty of the analysis is of statistical origin, various sources of systematic uncertainty are considered.

All normalization uncertainties are assigned to the signal yield and are reported in the following list:

- **Luminosity uncertainty:** 2.5% on the signal normalization was assigned to reflect the uncertainty on the knowledge of the total integrated luminosity.
- **Selection efficiency uncertainties:** a 6% uncertainty on the signal normalization was included to reflect the uncertainty on the knowledge of the data/simulation scale factors. This value is equivalent to two times the total uncertainty of the last p_T bin of Figure 4.4. Although the chosen value is very conservative the effect on the final results is very small given their relative larger statistical uncertainty.
- **Parton distribution functions:** a 6% uncertainty on the signal normalization was assigned in order to account for the variation in the kinematic acceptance of the analysis coming from the use of alternative PDF sets.
- **Photon energy scale uncertainty:** a 1% energy scale uncertainty was assumed. This number was derived to take into account the knowledge of the energy scale uncertainty at the Z peak as well as the knowledge on the extrapolation to high mass.
- **Photon resolution uncertainty** The uncertainty introduced by the extra smearing on the photon energy was evaluated summing and subtracting 0.2% in quadrature from the estimated constant term measured at the Z peak. This figure represent the envelop of the uncertainties on the extra smearing measurement reported in Section 4.5.

The parametric background model has no associated systematic uncertainties, except for the bias term uncertainty described in Section 4.6.2. The shape coefficients are treated as unconstrained nuisance parameters and contribute to the statistical uncertainties.

4.7 Results on the search for BSM resonant diphoton production

The standard LHC test statistic $q(\mu)$ is used to provide a statistical interpretation of the results:

$$q(\mu) = -log\lambda(\mu) := -log\frac{L(\mu \cdot S + B|\hat{\underline{\theta}}_{\mu})}{L(\hat{\mu} \cdot S + B|\hat{\underline{\theta}})} \tag{4.7}$$

Where the likelihood is the one described in Section 4.6, S and B are the pdf's for the signal and SM processes respectively, μ is the "signal strength" parameter and $\underline{\theta}$ are the nuisance parameters of the model. The $\hat{}$ notation indicate best-fit value of the parameters.

The value of λ is bounded between 0 and 1, where the latter denotes a good agreement between the observed data and the hypothesized value of μ. Consequently, the higher the value of the test statistic $q(\mu)$, the higher the incompatibility between the observed data and the hypothesized signal model with signal strength μ. The discovery of a new diphoton resonance would appear as a localized excess of events. The SM background only hypothesis is the null hypothesis in the test and correspond to $\mu = 0$.

Since no significant deviation from the SM prediction is observed in data in the search region ($m_{\gamma\gamma} > 500$ GeV) Upper exclusion limits on the resonant diphoton production rate under different signal hypotheses are set using the modified frequentist method, which is a standard method among searches for BSM physics at LHC. It is also known as the CL_s method [164, 165]. The signal plus background hypothesis (H_1) is tested against the alternative, background-only hypothesis (H_0). For upper limits, the test statistic $q(\mu)$ of Equation 4.7 is defined as [163]:

$$\tilde{q}(\mu) = \begin{cases} -2\ ln(\lambda(\mu)), & 0 \leq \hat{\mu} \leq \mu. \\ 0 & \hat{\mu} > \mu. \end{cases} \tag{4.8}$$

the lower bound $\hat{\mu} \geq 0$ is dictated by physics (signal rate is positive), while the upper constraint $\hat{\mu} \leq \mu$ is imposed by hand in order to guarantee a one-sided confidence interval which in turn ensures that upward fluctuations in data are not considered as evidence against the signal plus background hypothesis.

Two probabilities are defined, one for the signal plus background hypothesis ($CL_{s+b} = P(\tilde{q}_{\mu} \geq \tilde{q}_{\mu,obs}|H_1)$) and one for the background-only hypothesis ($CL_b = P(\tilde{q}_{\mu} \geq \tilde{q}_{\mu,obs}|H_0)$). The CL_s is defined as the ratio of the two probabilities and depends on the tested signal strength μ:

$$CL_s = \frac{CL_{s+b}}{CL_b}$$

The CL_s value needs to be smaller than a threshold α to exclude the tested signal model (H_1 hypothesis) with signal strength μ at a confidence level (CL) of $(1 - \alpha)$. This chosen threshold is 0.05, corresponding to a 95% CL_s limit. The above probabilities CL_b and $CLs + b$ are calculated for different values of μ. All possible q_{μ} are tested until a signal strength that gives a CL_s value lower than $\alpha = 0.05$ is found.

Throughout the calculations the asymptotic formulas described in [48] are used.

4.7.1 Exclusion limits on the production of spin-0 and spin-1 resonances

As previously stated two models are considered as benchmarks in this search for resonances decaying to two photos:

- RS gravitons (spin-2).
- spin-0 resonances produced via gluon-fusion.

For each of the hypotheses, three different width Γ/M are considered: 0.014%, 1.4% and 5.6%. In the case of the RS graviton resonances, the width is parametrized as $\Gamma/M = 1.4k^2$ and thus k=0.01,0.1,0.2. The three values are representative of three different scenario: the narrowest reflect the case of an intrinsic width negligible with respect to the detector resolution (i.e. the ECAL energy resolution), the second reflect the case of a resonance width comparable to the detector resolution and the third the case of a resonance with a intrinsic width larger than the mass resolution.

The median expected and observed exclusion limits for different signal hypotheses are shown in Figure 4.18 for RS graviton and gluon-fusion-produced spin-0 resonances of different widths.

4.7.2 Exclusion limits on the fiducial cross-section for resonant diphoton production

The same set of events can be interpreted setting a limit on the resonant diphoton production cross-section. This approach allows one to compare the experimental results with the prediction from any model; the only assumption are dictated by the width of the resonance and the shape of the signal, which is assumed to be the same double-sided crystal ball function described in Section 4.6.3.

The limits are set independently for the EBEB and EBEE categories and the fiducial volume is defined by a set of selections applied to the simulated signal sample on generator level quantities reported below:

- The generator level transverse momentum of each of the two photons grater than 75 GeV.
- Generetor level isolation (Iso_γ^{gen}) less than 10 GeV. Where Iso_γ^{gen} is defined as:

  $$Iso_\gamma^{gen} = \sum p_T$$

  The sum runs over all the generator level particles, regardless of the type, included within a cone of radius $\Delta R = 0.3$ around the direction of the photon in the η-ϕ plane.
- Detector acceptance: $|\eta_{\gamma 1,2}^{gen}| < 1.442$ for the EBEB category and $|\eta_{\gamma 1}^{gen}| < 1.442$, $1.556 < |\eta_{\gamma 2}^{gen}| < 2.5$ for the EBEE one.

The signal normalization is determined by the selection efficiency reported in Figure 4.16. The background estimation and systematic uncertainties on the signal yield are the same as for the benchmark model results (Section 4.6.4) except for the uncertainty introduced by the variation of the parton density functions, which is irrelevant in this case.

The median expected and observed exclusion limits for the model independent diphoton resonant production are shown in Figure 4.18 for the two event categories and the three relative width considered in the analysis

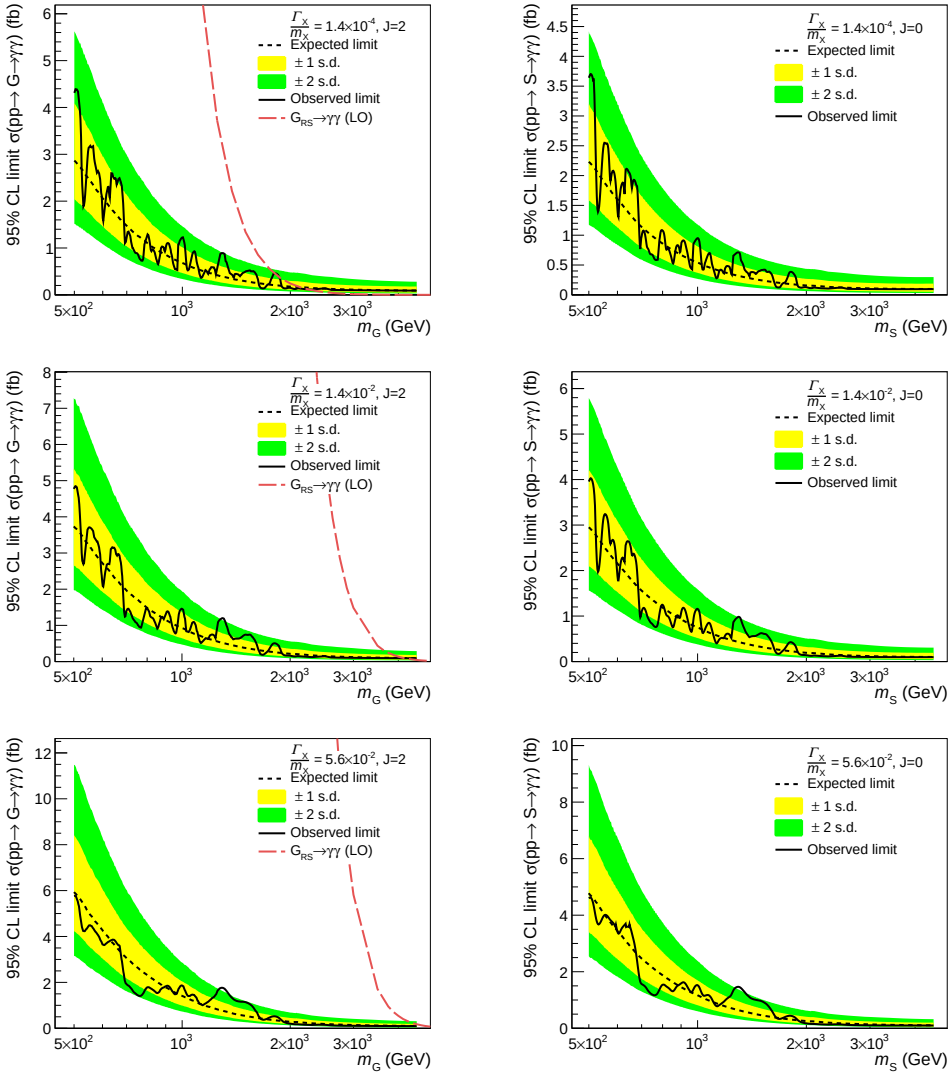

Figure 4.18: Expected and observed upper limit for RS graviton (left) and gluon-fusion-produced spin-0 (right) resonances of different widths decaying to two photons: narrower (top) to wider (bottom). For RS graviton the expected cross-section times branching fraction for the decay to two photons is shown by the dashed red curve. The limits are shown as a function of the reconstructed diphoton invariant mass.

4.8 Summary

The search for local excesses in the diphoton spectrum compatible with the prediction of wrapped extra dimension models for the production of a massive spin-2 boson and spin-0 Higgs-like boson predicted by MSSM models has been performed using data collected by the CMS experiment during 2016.

The observed data are compatible with the standard model prediction through all the analyzed part of the diphoton spectrum. In particular the results exclude the existence of a RS-graviton with masses below 2.1 TeV and $\kappa = 0.01$. The excluded region extends more than $\sim$ 4 TeV for wider resonances with $\kappa = 0.1$ and 0.2. The results are compatible with those presented by a similar search performed by the ATLAS collaboration with data collected during the same period [49]. These results extend the sensitivity of those

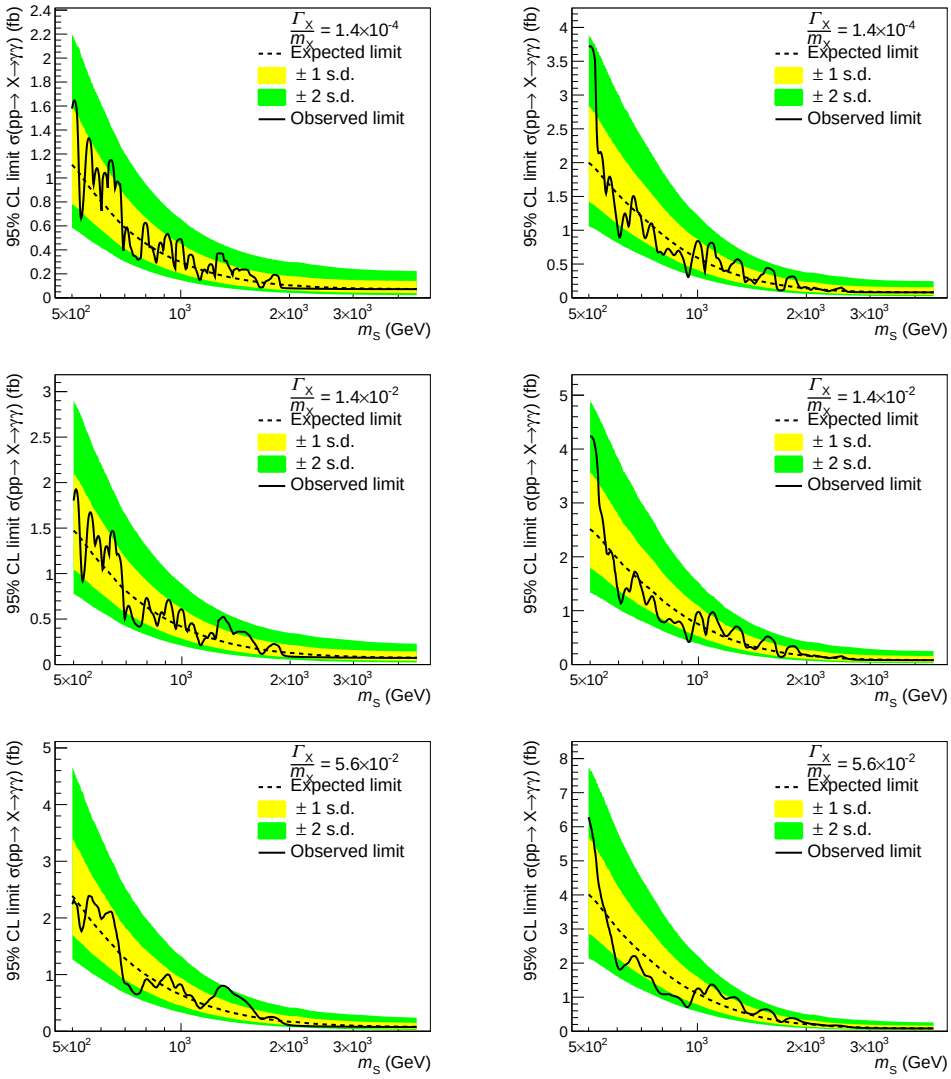

Figure 4.19: Expected and observed upper limit for the EBEB (left) and EBEE (right) categories for a generic resonant production of diphoton pairs as a function of the reconstructed diphoton invariant mass. Three different relative resonance width hypothesis are considered: $\Gamma/m = 0.014\%$(top), 1.4%(middle) and 5.6%(bottom).

previously published by CMS with data collected at both 8 and 13 TeV LHC center of mass energies [50, 19, 51].

No combination of the results with those collected at 8 TeV is done since with an integrated luminosity of 35.9 fb^{-1} the sensitivity of the analysis performed with data at 13 TeV dominates over the 8 TeV one.

Chapter 5

The HL-LHC upgrade of CMS

In this chapter the upgrade of the LHC complex is briefly introduced in Section 5.1 underlining the physics goals and the expected performance of the machine. The CMS experiment is already planning a series of upgrades, most of which will be installed during LS3 (Figure 2.1). The overall upgrade project of the CMS detector is outlined in Section 5.2, with further details on the foreseen inclusion of time information in the event reconstruction given throughout the rest of the chapter.

5.1 High Luminosity LHC

The main objective of the High Luminosity LHC (HL-LHC) upgrade [52] of the LHC accelerator complex is to make precise measurements of the Higgs boson couplings, other rare standard model processes (like the vector boson scattering) and provide a very large dataset ($3000\,\mathrm{fb}^{-1}$) for new physics searches. The design includes a substantial upgrade of the accelerator complex with the goal of reaching a peak luminosity of $7.5 \times 10^{34}\mathrm{cm}^{-2}\mathrm{s}^{-1}$ (roughly four times as much as the current value). The integrated luminosity will be about ten times the expected luminosity of the first twelve years of the LHC. The timeline of LHC and HL-LHC operation is sketched in Figure 2.1, showing the planned evolution of proton beam intensity through the remaining LHC operating periods (Run 2 and Run 3) and the HL-LHC operating period following the upgrade of the accelerator complex in LS3.

The peak luminosity will be achieved by increasing the beams intensities and by squeezing by a factor two more the two beams at the interaction points where ATLAS and CMS are located. This will lead to a higher number of collisions occurring within the same bunch crossing, the average number of collisions will increase from 40-60 of LHC to 140-200 at HL-LHC. The ability of the detectors (ATLAS and CMS) in assigning particles to the correct collision within the same bunch crossing will worsen with the increased instantaneous luminosity. In order to take advantage of the increased dataset both experiments are planning to upgrade their detectors to improve the event reconstruction and also improve the radiation resistance of the detectors components.

5.2 HL-LHC upgrade of CMS

The CMS detector will be upgraded to match the operation environment of HL-LHC in order to fully exploit the larger dataset delivered by the accelerator complex. The major points is the complete replacement of the current tracker [53]. The new system will maintain the same concept of an all silicon detector with four pixel layers for the precise vertex reconstruction surrounded by silicon strips devoted to the measurement of the charged particle momentum, but the new detector will have a finer granularity and an extend pseudorapidity coverage (from the current $|\eta| = 2.5$ to 4). The finer granularity will mitigate the increased tracks overlap while the extended coverage will provide a larger acceptance for analyses of interest in the context of HL-LHC. Contrary to the current system. The new tracker will provide information to the Level-1 trigger system, the information will be exploited to compute isolation quantities and to improve the energy resolution on jets and E_T^{miss}. This improvements are expected to provide a way to control the trigger rate by improving the event selection already at the Level-1 trigger even with energy thresholds lower than the ones currently in use, resulting again in an acceptance gain especially for precision measurements of rare standard model processes.

The Level-1 itself will also be upgraded with a completely new dedicated electronics, the trigger rate will increase from 100 kHz of LHC to 750 kHz of HL-LHC. The upgrade of the trigger will be matched with upgrades in most of the sub-detectors electronics to provide information with the higher rate.

The current calorimeter system present in the endcaps will not survive till the end of HL-LHC due to radiation damage (more than $1.5 \times 10^{15} n_{eq}/cm^2$ in the parts closer to the beam line) affecting the active components of ECAL ($PbWO_4$ crystals) and HCAL (scintillating tiles and photo-detectors). The two calorimeters will be replaced with a silicon based high granularity sampling calorimeter (HGCAL) [54] with tungsten absorbers in the electromagnetic part and lead absorbers in the hadronic one. The longitudinal segmentation will provide discrimination between overlapping energy deposits.

The muon system acceptance will also be extended up to $|\eta| = 2.8$ [55] with the insertion in the magnet return yoke of GEM based detectors. This will be beneficial for precision measurements of the Higgs boson properties through its decay in four muons ($H \to ZZ \to 4\mu$).

The CMS experiment is also investigating the possible benefits arising from the inclusion of the particles time of flight information into the event reconstruction. The gain is related to the fact that collisions overlaps in space within the luminous region but can be separated in time to reduce the number of concurrent collision at the LHC level provided a resolution of the order of 10 ps (Figure 5.1). From the knowledge of the production time at the interaction point and that of the energy deposits from in the calorimeters or dedicat timing layer the particles are assigned to the correct collision exploiting the time information. The improvements is thus bounded to to measurements: the reconstruction of the time of flight of charged particles to reconstruct the time of the interaction vertex and the time of energy deposits in the calorimeters. For this reason a new detector has been proposed to measure the time of flight of charged particles while the upgrade of the ECAL barrel and the design of the new endcap calorimeter are being optimized to provide a time measurement with a precision of 30 ps for electrons and photons with an energy greater than 20 GeV.

Description of the detector technologies and measurements of their time performance are reported in Sections 5.3, while examples of performance improvements obtained with simulation studies are described in Section 5.5.

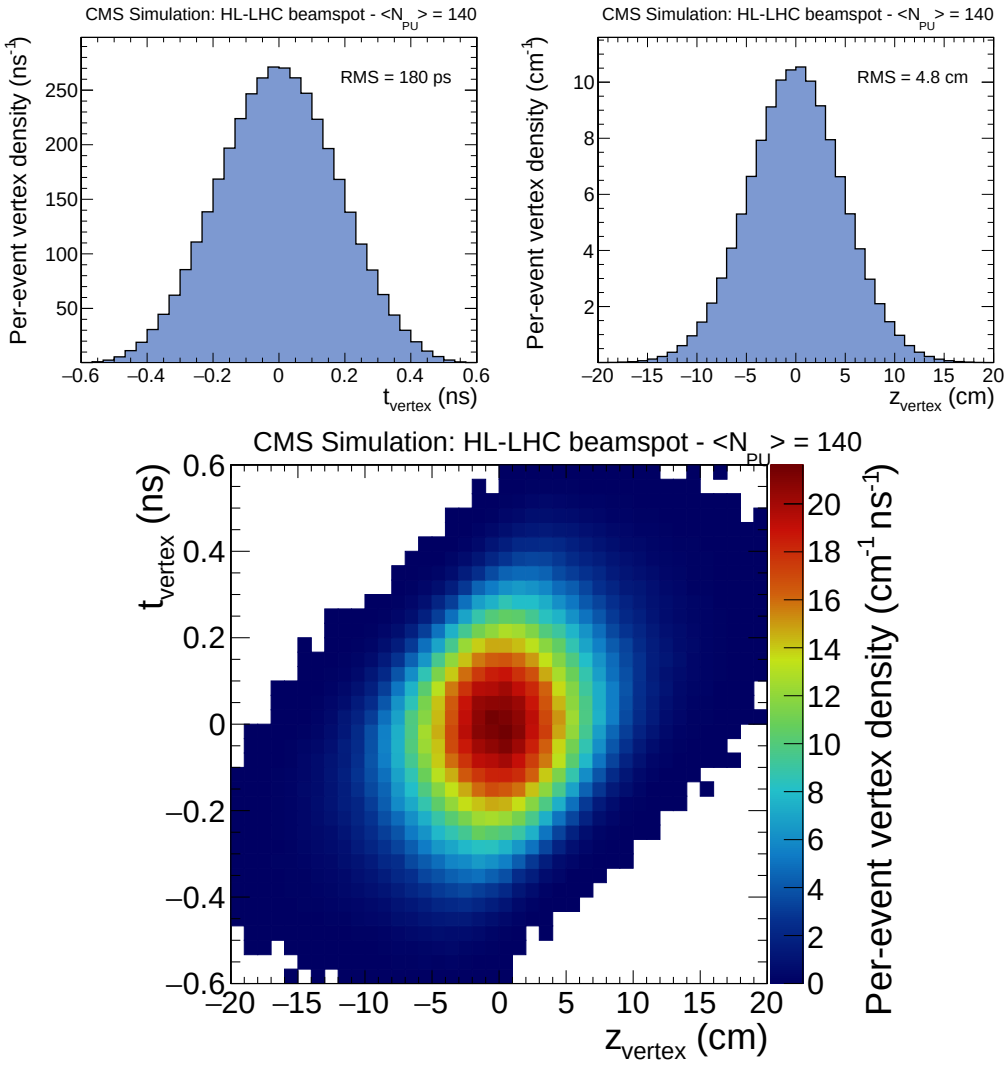

Figure 5.1: Collision vertex density in the HL-LHC luminous region for one of the possible beam optics configuration. The vertex time distribution is shown in the top left plot, the time of the vertex is measured with respect the nominal bunch crossing time provided by the LHC clock. The histogram bin width is 40 ps so, given the y-axis normalization, the peak of the distribution corresponds to 10 vertices occuring within a window of 40 ps. The spatial distribution along the beam axis is shown in the top right figure while the two dimensional distribution is shown in the bottom plot. The distribution are representative of peak instantaneous luminosity of $5 \times 10^{34} cm^{-2} s^{-1}$ implying an average number of collision per bunch crossing of 140. The ultimate HL-LHC performance will reach an average of 200 concurrent collisions, which will translate in a peak line density of 1.9mm^{-1} challenging the ability of the tracker to correctly assign charged particles to the correct vertex.

5.3 Detector R&D for precise time measurement in CMS

Sub nanosecond precision has already been achieved in high energy physics experiments and at LHC. The current best performances are from the ALICE Time Of Flight system [56], the LHCb TORCH detector [57] and the CMS ECAL as described in the following section. The ALICE TOF is based on Multi-gap Resistive Plate Chambers capable of a resolution of 80 ps. The LHCb TORCH can reach a precision of 50 ps using Micro Channel Plate (MCP) photo-detectors. Both systems are designed for low energy particles discrimination at low luminosity collider experiments, thus both technologies although already operational at LHC cannot survive the higher irradiation level of CMS during HL-LHC. The CMS ECAL on the other end is currently limited by clock distribution as explained in Section 5.4.1 but is capable of an intrinsic time performance of better than 30 ps (see 5.4.1).

A series of beam tests were conducted during 2015 and 2016 to establish the time performances of detector technologies suitable to be operated in CMS during the HL-LHC phase. These detectors includes silicon pads for the HGCAL, devices optimized for time measurement of minimum ionizing particles (MIP) and also the study of the ECAL $PbWO_4$ crystals and its HL-LHC readout electronics time performance. Most of the test were performed at the CERN SPS North area at the H2 and H4 beam lines (more details are given in Section 5.4.1) with a data acquisition system (DAQ), reconstruction and analysis software developed specifically for the needs of these tests. The reconstruction software is optimized for signals digitized at high frequency (5 GHz), different algorithms are implemented to extract the amplitude and time information from the peculiar signal shapes of each of the tested detectors (see Section 5.4.1).

During beam tests conducted during 2015 the time performance of silicon sensors suitable to be installed in the future CMS endcap calorimeter have been measured [58]. Several sensors of different thickness were tested, all of which were p-type ($n-on-p$) 5×5 mm^2 in effective area. The results (Figure 5.2) shows an excellent time resolution for showering electrons with an energy of 50 GeV. The resolution is found to be better than 20 ps for signals with a $S/\sigma_n > 20$, where S is the signal amplitude and σ_n is the noise RMS. This figure in the final HGCAL will be achieved for energy depositions equivalent to 10 MIP. The HGCAL time measurement will also profit from the longitudinal segmentation that will allow to combine more than one time measurement. Simulation studies shows that a resolution at the level of 20 ps is achieved for electromagnetic showers with energies above 2 GeV and for hadrons above 20 GeV.

The study on the ECAL time performance is reported in details in the next sections. The results show that, given a clock distribution precision better than 10 ps, a time resolution of 30 ps is achieved at energies of at least 25 GeV at the beginning of HL-LHC.

These results show the case for the installation of a dedicated detector for the time measurement of charged particles: none of the existing or foreseen detectors is capable of provide timing information for MIP particles with an acceptance covering up to $|\eta| \sim 3$ and $p_T > 0.7$ GeV (barrel) or $p > 0.7$ GeV (endcaps).

Given the different irradiation levels and installation schedule constrains, two different technologies will be adopted for the barrel and endcap timing detectors. In the endcaps (ETL) two planes of Low-Gain Avalanche Detectors (LGAD) silicon sensors have been proposed since this is the only technology to survive a dose of $2\times10^{15} n_{eq}/cm^2$ (corresponding to the irradiation level reached after 4000 fb^{-1}at $|\eta| = 3.0$) while still providing a 50 ps single sensor time resolution [59]. The detector will have a pseudorapidity acceptance from about $|\eta| = 1.6$ to $|\eta| = 2.9$.

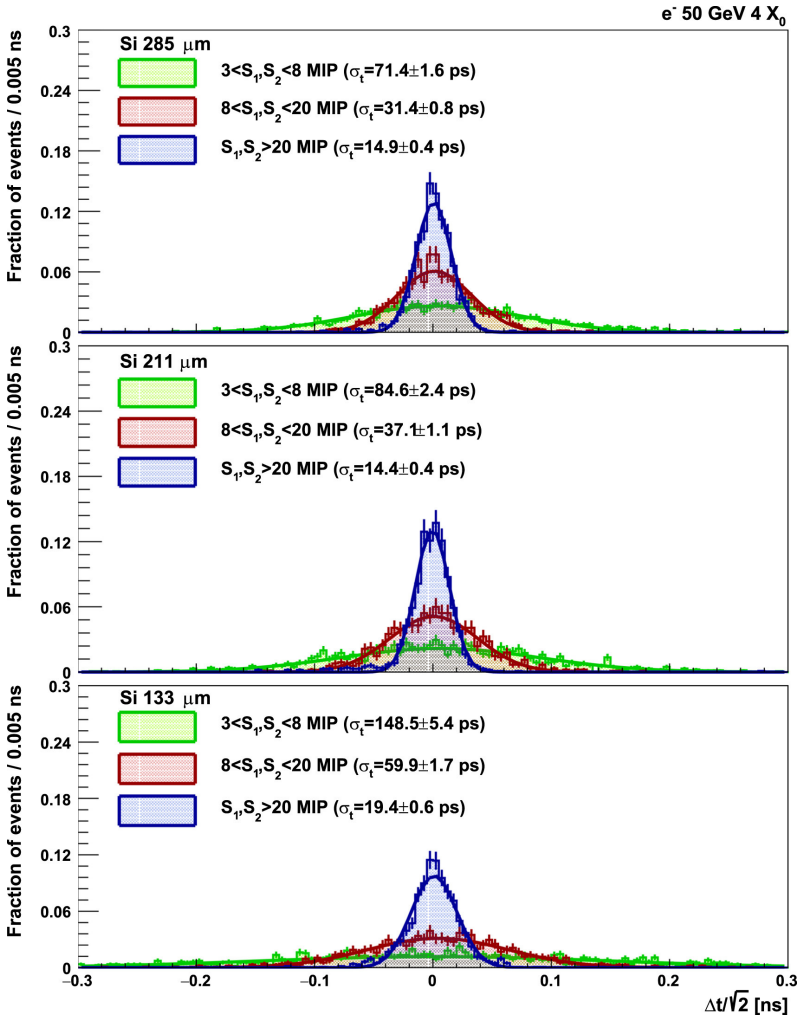

Figure 5.2: The distribution of the time difference between the signals from a pair of silicon sensors ($\Delta t = t_1 - t_2$), 133-μm (bottom), 211-μm (middle), and 285-μm (top) thick, as a function of three different signal ranges as indicated on the upper left corner of each plot. The solid lines represent Gaussian fits to the data points. The sensors were placed behind a $4X_9$ lead absorber and the electron beam energy was 50 GeV. [58]

In the barrel region the timing detector (BTL) proposed location is between the silicon tracker and the ECAL, inside the tracker support structure. This location poses severe constrains on the development and construction of the timing detector since it will be mounted in the support structure before the tracker sensors. This imposes to complete the development, construction and installation of the detector by 2021, at the beginning of LS3 and 2 year before the ETL. For this reason a different technology has been chosen for the barrel sensors. LYSO crystals with Ce doping with a surface of $12 \times 12\text{mm}^2$ and a variable thickness between 3 and 4 mm coupled to Silicon photon multipliers (SiPM) will form the basic cell of the barrel timing detector. This technology has already been extensively tested for medical applications (PET), the challenging environment of HL-LHC anyway will require a different optimization of the geometry. The radiation dose accumulated during HL-LHC will be a order of magnitude lower in the barrel than in the endcaps making the choice of LYSO crystals and SiPM viable for the BTL but not for the ETL. Beam test results shows (Figure 5.3) that a time resolution of 30 ps is achieved

with a sensor that matches the power consumption and radiation hardness constrains of HL-LHC operation. The test beam were conducted using the same setup described for the ECAL tests, in particular the same time reference detector (MCP) and SiPM readout chip was used. This chip does not provide sufficient radiation tolerance to be operated at HL-LHC. The final readout chip will be adapted from an existing chip for medical applications. The time measurement in the barrel sensors is found to depend on the MIP impact position, as shown in Figure 5.3 the effect can be corrected to reach a 30 ps time resolution with a spatial precision of 1 mm on the impact point. Such precision is achieved only for tracks with $p_T > 2$ GeV thus alternative geometries are being investigated.

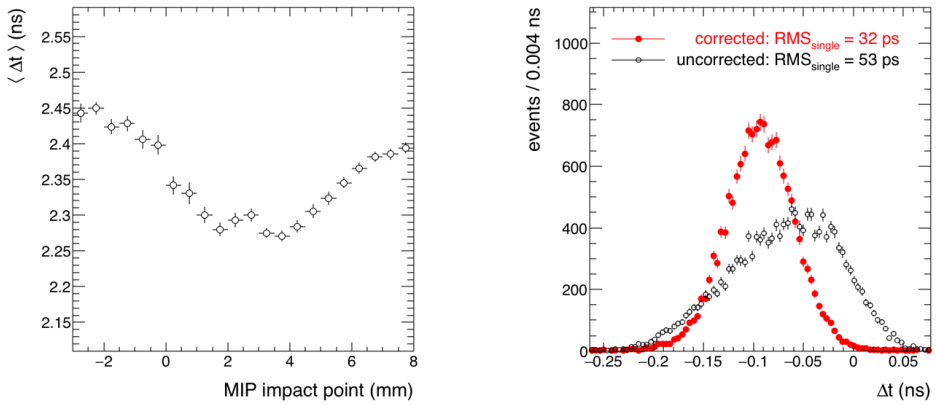

Figure 5.3: Difference between the time measurements in LYSO+SiPM cell and in a reference MCP as a function of the MIP impact point on the crystal surface (left). Time resolution before and after the application of a position dependent correction (right).

5.4 The ECAL barrel upgrade

The primary technical motivation for the ECAL barrel (EB) upgrade is the trigger requirement for an increase of the trigger latency from about 4μs in the current system to a maximum of 12.5μs, and a Level-1 trigger rate of up to 750 kHz compared to the current 100 kHz. The EB electronics Front End (FE) card and all the read-out electronics will be replaced to meet these requirements. The current configuration provides trigger information to the Level-1 with a granularity of five-by-five crystals, the upgraded system will have a single crystal granularity enhancing event selection based on isolation information at trigger level which will in turn allow to set lower thresholds on the transverse energy of the candidate particles.

The foreseen upgraded FE electronics will also provide a shape discrimination between signal compatible with an electromagnetic shower and those originated from hadronic interaction ("spikes") in the photo-detector (APD) which have a narrower shape. The increased Level-1 granularity of a single crystals will also improve the rejection of such events at trigger level. The shape discrimination is made possible by a shorter signal shaping performed by the new trans-impedance amplifier (TIA) and by an ADC with sampling frequency of 160 MHz (four times the current one). The TIA and the increased sampling frequency are also the key upgrade to provide a time measurement at the 30 ps level. More information about the ECAL HL-LHC upgrade can be found in [60]

5.4.1 The current ECAL timing performances

The time of an electromagnetic shower in the ECAL is defined as the time at which the signal generated in the APDs reaches its maximum amplitude. The method to extract this information from the digitized signal shape is described in [61]. The time of the maximum T_{max} is estimated with each available pair of samples (up to nine) as:

$$T_{max,i} = T_i - T(R_i)$$

where i is the $i-th$ sample, T_i is acquisition time of the $i-th$ sample and $T(R_i)$ is the time corresponding to the amplitude ratio $R_i = A_i/A_{i+1}$ and is extracted from a parametrization whose parameters were measured in a test beam prior the installation of CMS. The error (σ_i) on each $T_{max,i}$ is estimated as the product of the derivative of the $T(R)$ function and the uncertainty on R_i which is the sum in quadrature of three components: noise fluctuations in each sample, uncertainty on the pedestal value subtracted from the measured amplitude and truncation occurring during the 12 bit digitization of the amplitude. For signal synchronized with the LHC bunch crossing only the largest five of the nine possible amplitude ratios are used. The unique signal time is computed as the weighted average of the $T_{max,i}$:

$$T_{max} = \frac{\sum_i T_{max,i}/\sigma_i^2}{\sum 1/\sigma_i^2}$$

and the its error as:

$$\frac{1}{\sigma^2_{T_{max}}} = \sum_i \frac{1}{\sigma_i^2}$$

The time resolution can be parametrized as:

$$\sigma^2(t) = \left(\frac{N \cdot \sigma_n}{A}\right)^2 + \left(\frac{S}{\sqrt{A}}\right)^2 + C^2 \tag{5.1}$$

where A is the measured signal amplitude, σ_n is the RMS of the noise for each sample and N, S, C represent the noise, stochastic, and constant term coefficients, respectively. The stochastic term S is related to fluctuations in the collection times of scintillation photons due to the finite time of their emission.

The time performance of the ECAL has been estimated both during the pre-installation test beam [61] and with data collected during the 8 TeV operation of LHC [62]. In the test beam measurement the resolution was extracted from the time difference between the two most energetic crystals of the same electromagnetic shower, in this configuration the stochastic term that appears in Equation 5.4.1 can be neglected since shower fluctuation effects cancels out in the difference, Equation 5.4.1 thus becomes:

$$\sigma^2(t_1 - t_2) = \left(\frac{N \cdot \sigma_n}{A_{eff}}\right)^2 + 2 \cdot C^2 \tag{5.2}$$

Where $A_{eff} = A_1 A_2 / \sqrt{A_1^2 + A_2^2}$ and $t_{1,2}$, $A_{1,2}$ refers to the times and amplitudes measured by the two crystals. The time resolution $\sigma(t_1 - t_2)$ was estimated with a Gaussian fit to the time difference. The results obtained in the analysis report a constant term of 20 ± 4 ps which, together with a noise term $N = 35.1 \pm 0.2$ ns, gives and expected time resolution better than 100 ps for energy deposits greater than 20 GeV in the barrel.

The prediction was tested with data collected during 2011 and 2012 from CMS. With collisions events it is possible to test the performance of the whole system including the clock distribution. $Z \rightarrow e^+e^-$ events were used in [62] the results show a good performance when measuring the time difference for channels belonging to the same readout unit while an increasingly poorer performance for channels in different readout units but same shower and channels belonging to the two different super-clusters in $Z \rightarrow e^+e^-$ events (Figure 5.4).

These results were interpreted to be due to time jitter introduced by the clock distribution system and not corrected by the calibration performed with low energy deposits. The clock stability has been measured in 2016 using laser monitoring data and while the time resolution constant term is found to be below 40 ps even for crystals belonging to different readout unit, instabilities of the clock synchronization at the level of 100 ps were observed over the course of few days. The observed effect is in agreement with the constant term measured using $Z \rightarrow e^+e^-$ events that are collected over a long period of time.

Beam test setup

During 2015 and 2016 a series of tests with electron beams were performed to evaluate the time performance of the $PbWO_4$ crystal plus APDs photo-detectors system and that of the proposed HL-LHC ECAL electronics. The tests differ from the one conducted before the CMS installation since the time of the electron measured by the crystal is compared to an external reference provided by a multi-channel-plate based detector (MCP) instead of an adjacent crystal hit by the some shower.

The tests were conducted at the CERN SPS north area with a configurable beam of electrons with energies between 20 and 250 GeV. The electron beam is a secondary beam created from the primary proton beam, extracted from the SPS, using a converter. The primary beam hits a metallic target producing a variety of particles that are selected through a system of magnets, collimators and additional targets. The beam line used for the tests can reach a electron purity of 99% and can also be configured to provide a equally pure pion beam to study "spikes" in the APDs. The beam in the SPS is composed

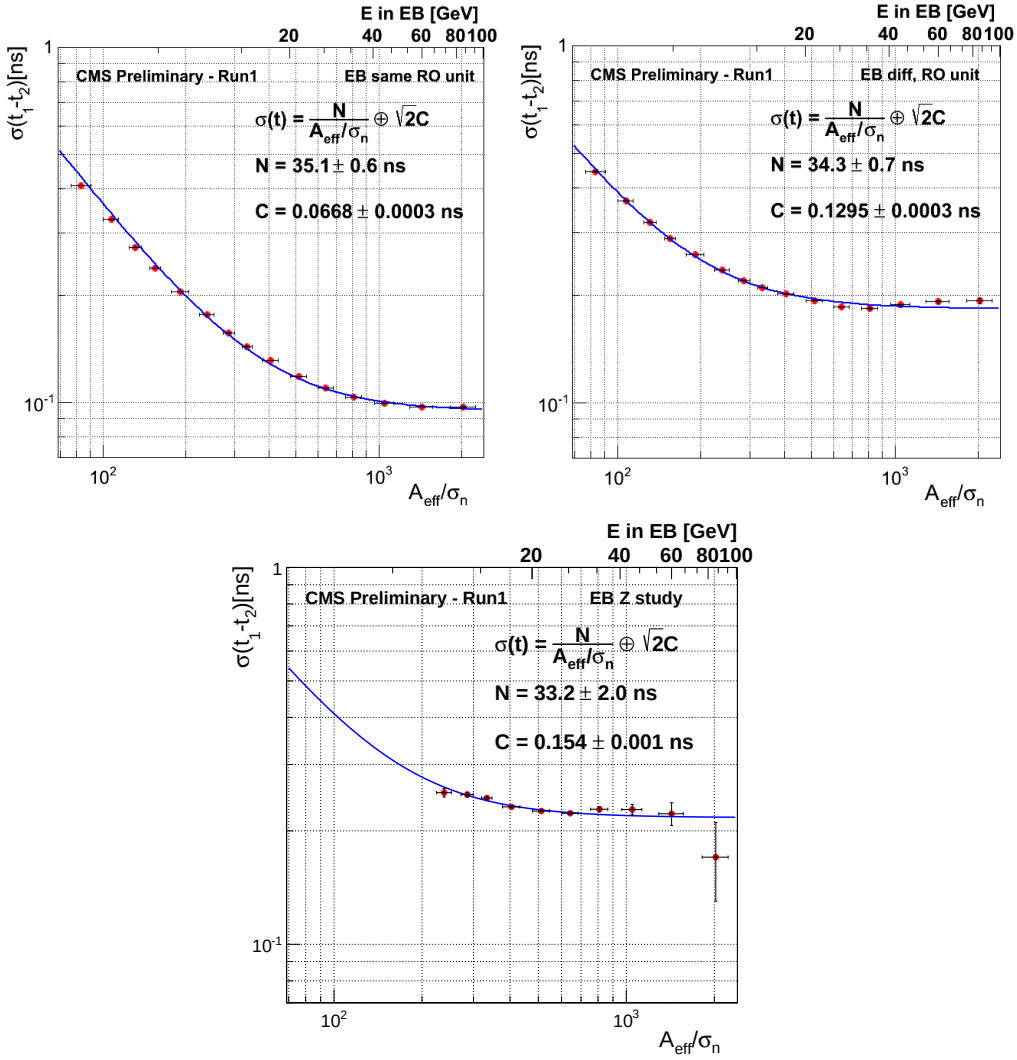

Figure 5.4: Resolution of time difference between the two most energetic crystals of an ECAL cluster as a function of the effective amplitude A_{eff}, normalized to the noise in the ECAL Barrel for 2011+2012 data, for crystals belonging to the same readout unit (top left), different readout unit (top right) and the two most energetic crystals in each of the super-clusters generated by electron from Z $\rightarrow e^+e^-$ decays (bottom). In the last case the time of each crystals belonging to the two electrons super-clusters is corrected for the time of flight from the common interaction vertex.

of several bunches that are extracted in an interval of 4-5 s every 14-48 s depending on the SPS cycle configuration. The extraction line is configured in a way to destroy the bunch scheme of the SPS beam in order to provide a uniform and less intense beam to the test area. The energy of the secondary beams of electrons, positron, muons and charged pions can be selected within the 10 to 250 GeV range.

The experimental setup included a 5×5 $PbWO_4$ crystal matrix identical to those installed in the ECAL barrel, with two APDs glued at the back (a schematic view of the setup is shown in Figure 5.5). In a first beam test, the APDs signals were amplified with the same $CR-RC$ circuit installed in the current ECAL supermodules, the shaping time for some of the channels was set to 21.5 ns (half of the current one) to match the one

proposed for the HL-LHC upgrade. The amplified signal was digitized with a 5 GSample/s commercial digitizer (CAEN V1742 VME board) instead of the final design DAC with 160 MHz sampling frequency. In order to estimate the impact of fluctuation in the light production depth on the time resolution, two of SiPM arrays were glued to the front face of the central crystal. The CAEN digitizer was used to readout also the signals of the two SiPM. In a second test a prototype of the HL-LHC readout electronic was installed in place of the CR-RC amplification. The signal from the TIA amplifier was digitized with the same VME board and the 160 MHz sampling ADC simulated at the analysis level by sampling the signal shape acquired at 5 GHz by the CAEN digitizer. This second setup included also two identical MCP to directly estimate their time resolution.

The crystal matrix and readout electronics was kept at 18° inside a box to avoid light induced noise in the photo-detectors. The reference MCP detector was placed in front of the box. Incoming charged particles produce Cerenkov radiation in a quartz window coupled to a photo-cathode, the photo-electrons produced by the Cerenkov light hitting the photo-cathode are amplified by two layers of MCP and collected to the anode. The MCP device used in the test was characterized in different tests [63, 64] and its time resolution measured to be 25 ± 5 ps. The signal from the MCP was also digitized with the same CAEN board.

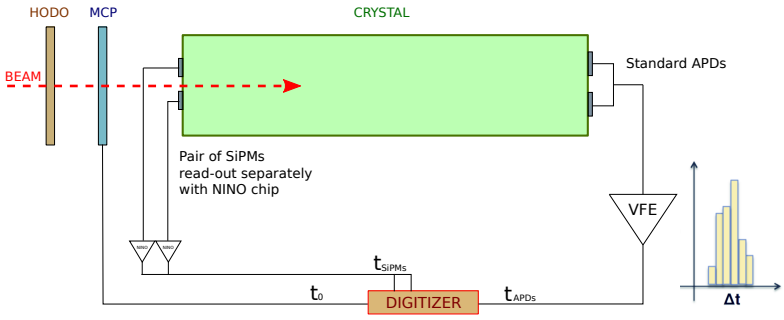

Figure 5.5: Schematic of the beam test setup (not to scale), the electron beam comes from the left side. The $PbWO_4$ crystal is drawn in green and the shape is simplified with respect the real trapezoidal one. The plastic scintillators described in the text are not drawn and were placed upstream of the hodoscope (to the left of HODO in the picture). As in the standard ECAL crystals the signals from the two APDs glued on the rear face are merged before the pre-amplifier (VFE in the scheme).

The setup was complemented by a set of wire chambers and scintillating fibers hodoscopes to measure the position in the plane transverse to the beam direction (x-y plane) of particles hitting the experimental setup. Each hodoscope is composed by a set of 64 fibers and has a spatial resolution of 0.5 mm and was placed 3 meter upstream of the crystals box and the MCP. The beam divergence is negligible and thus the impact point on the crystals face corresponds to the particle transverse position measured by the hodoscopes (Figure 5.6).

Incoming particles were also detected by three plastic scintillators placed few meters upstream of the crystals position, the three scintillation signals are discriminated and a trigger for the acquisition system is build as a coincidence of the three signals. The three scintillators dimensions are 6×6 cm^2, 3×3 cm^2, 1×1 cm^2, the smallest one selects event impinging at the center of the 2×2 cm^2 crystal front face.

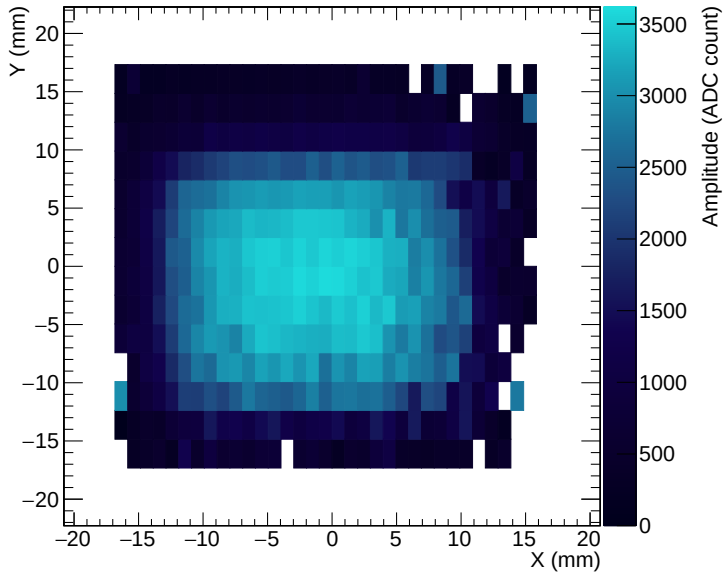

Figure 5.6: Distribution of the signal amplitude of a single crystals as a function of the transverse impact position measured with the hodoscope for a 50 GeV electron beam. For alignment purposes the events shown in the picture were acquired requiring only the coincidence between the 6×6 cm^2 and 3×3 cm^2 scintillators. The crystal front face is a square with 22 mm sides, the area covered by the crystal is clearly visible in the amplitude profile as the light area at the center.

Amplitude and time reconstruction at the beam test

The CAEN digitizer has 32 channels and for each event and channel acquires 1024 samples (one every 200 ps). The digital conversion is performed by a 12-bit DAC, the dynamic range of the DAC is 1 V. The channels are synchronized at a level better than 5 ps. The samples were shipped to a commercial PC through the VME bus and an optical interface, the event synchronization between the digitizer, hodoscopes and wire chamber data was performed by software running on the acquisition PC.

The MCP signal is very fast, lasting 4 ns, its amplitude is estimated with a second order polynomial fit to the seven samples around the maximum one while the time extracted with a constant fraction method to avoid amplitude walk effects.

The signal from the SiPM is readout through a custom board that provides the measurement of both the signal amplitude and time, the latter using a NINO chip [65]. The signal time is extracted with a precision under 10 ps as the time at which the signal pass a threshold that can be configured. This method is very sensible to the amplitude walk effect and the measured time is therefore corrected during the analysis.

The amplitude and time of the APD signal are estimated with a template fit to the signal shape where the signal amplitude and time of the maximum are free to float. The template shape is build as the average of 1×10^5 signals aligned using the time of the MCP signal in the same event and scaled by the amplitude estimated with the same approach used for the MCP signal. A different template shape is constructed in this way for each crystal. Two template examples are shown in Figure 5.7 for channel with different shaping times. The template fit gives the best time performance for APD signals

which has a smaller dV/dt compared to the MCP one.

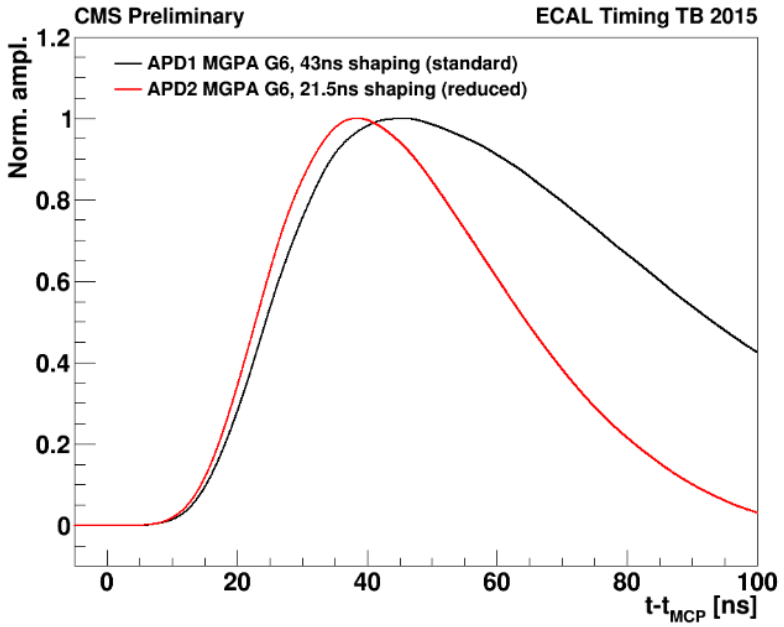

Figure 5.7: APD signal average shape for 21.5 ns and 43 ns shaping times.

Beam test results

The resolution of the $PbWO_4$ crystals plus APDs system is extracted from the distribution of the time difference between the time measured by the MCP (t_{MCP}) and the crystal (t_{APD}) hit by the electron. A Gaussian function is fit to the distribution and the standard deviation extracted from the fit is quoted as the time resolution. The operation is performed at different energies and for two channels with different amplifier shaping times. Only events in which the electron entered the crystal within 1.5 mm from the center of the front face where selected.

Figure 5.8 shows the results for the two different shaping times. The resolution as a function of A/σ_n is parametrized by the same Formula 5.4.1 used in the pre-installation test beam adjusting the constant term to take into account the known MCP resolution:

$$\sigma^2(t_{APD} - t_{MCP}) = \left(\frac{N \cdot \sigma_n}{A}\right)^2 + C^2 + C_{MCP}^2$$

where A and σ_n are the average amplitude and noise of the APD signal at a given energy, $C_{MCP} = 25$ ps is the MCP time resolution and N, C are the noise and constant term of the ECAL channel which are free to float in the fit. As expected, for the same beam energy, the shorter 21.5 ns shaping has a larger amplitude than the 43 ns shaping one, however in the fit data from both configurations are used.

The measured constant term is 27 ± 5 ps compatible with the 20 ± 4 ps value measured at the pre-installation test beam comparing the time of two crystals inside the some electromagnetic shower. The uncertainty on the constant term measured in the 2015 beam test takes into account the 5 ps uncertainty on the MCP resolution.

The test with the HL-LHC electronics prototype again proves a time resolution with a constant term better than 20 ps (17.9 ± 0.1 ps, Figure 5.9) with also an improved noise

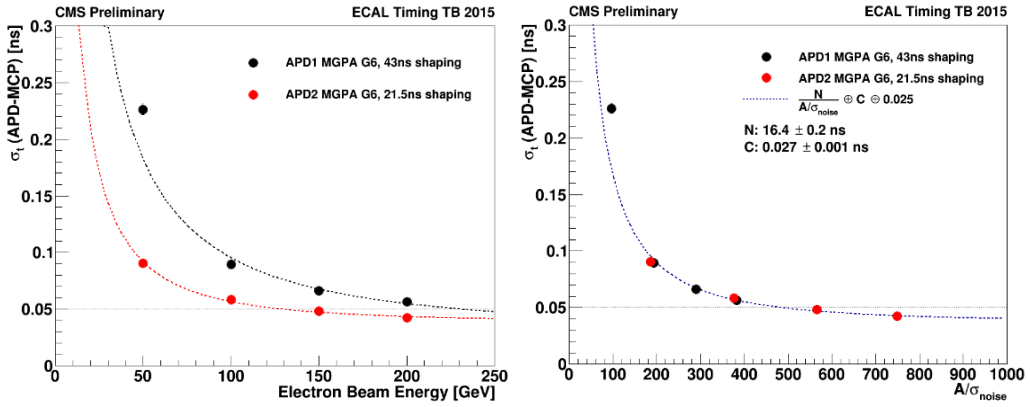

Figure 5.8: Time resolution on $t_{APD} - t_{MCP}$ as a function of the beam energy (left) and the average signal A/σ_n (right). In the left plot the lines are drawn to guide the eye while in the left plot the curve is the result of the fit described in the text.

term, as expected from the TIA. As explained above the TIA output signal was digitized at 5 GHz and the lower sampling frequency were emulated at the analysis level. In Figure 5.9 the different sampling frequency performance are compared: the 160 MHz sampling is identical to the one obtained with 5 GHz while at 80 MHz the time resolution depends on the sampling phase as expected given the typical APD signal frequency spectrum.

The impact of fluctuation in the light production depth on the time performance is estimated comparing the time performance of the SiPM with that of the APDs. As illustrated in Figure 5.10, the electromagnetic shower propagates faster than the scintillation light in the crystal by a factor equal to the $PbWO_4$ refractive index ($n = 2.2$). The different propagation velocity can spoil the time resolution and the effect is maximized when collecting the scintillation light on the front face since light produced later, deeper in the crystal also travels a longer minimum path to reach the photo-detector on the front face than the one on the rear face.

The intrinsic time resolution of the SiPM arrays is estimated comparing the time measured by the two different arrays using the same procedure described for APD and MCP comparison. In this comparison shower depth fluctuations cancels since are common to both SiPM arrays. The result and the fit are shown in Figure 5.11, the fitted time resolution constant term is 25 ps comparable to that of the APDs. The time resolution is worse when comparing the time measured by one of the SiPM arrays to the one recorded by the MCP, showing that fluctuation in the light emission depth impact the time resolution adding $\sim$ 80 ps in quadrature regardless of the shower energy. The effect is not seen in the APD performance, proving that the light collection from the rear crystal face gives the best timing performance.

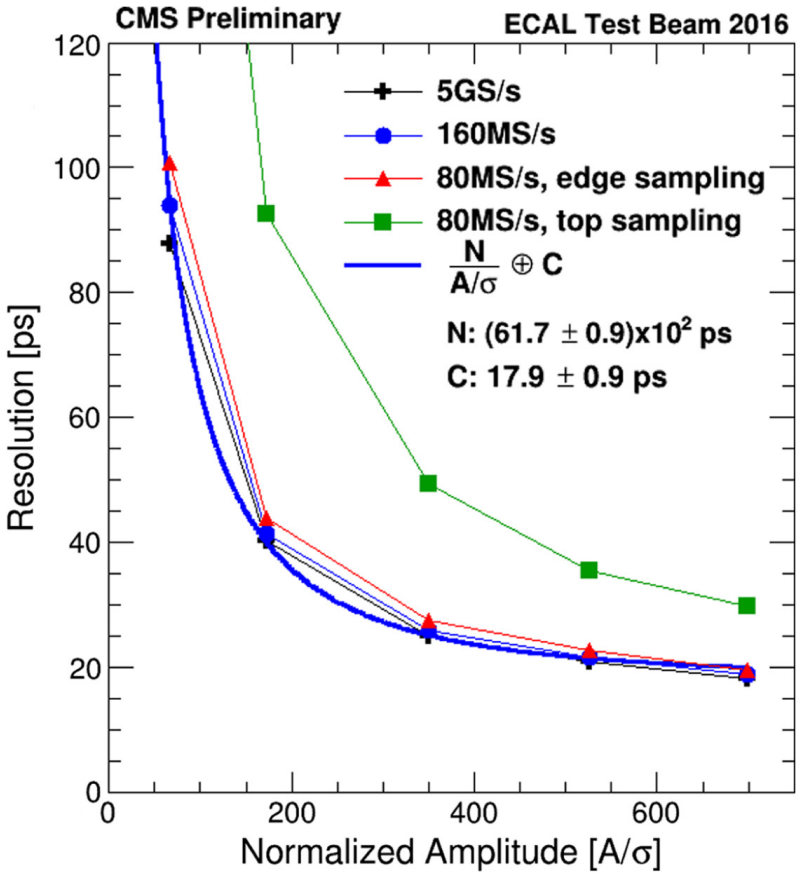

Figure 5.9: Time resolution performance of HL-LHC ECAL readout electronics for different sampling frequency. The baseline 160 MHz sampling frequency does not limit the time performance while the 80 MHz sampling performance depends on the phase between the electronics clock and the APD signal.

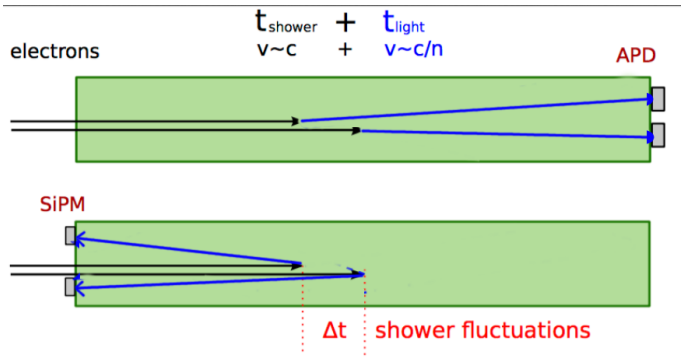

Figure 5.10: Illustration of light collection on the front and back face of the $PbWO_4$ crystal.

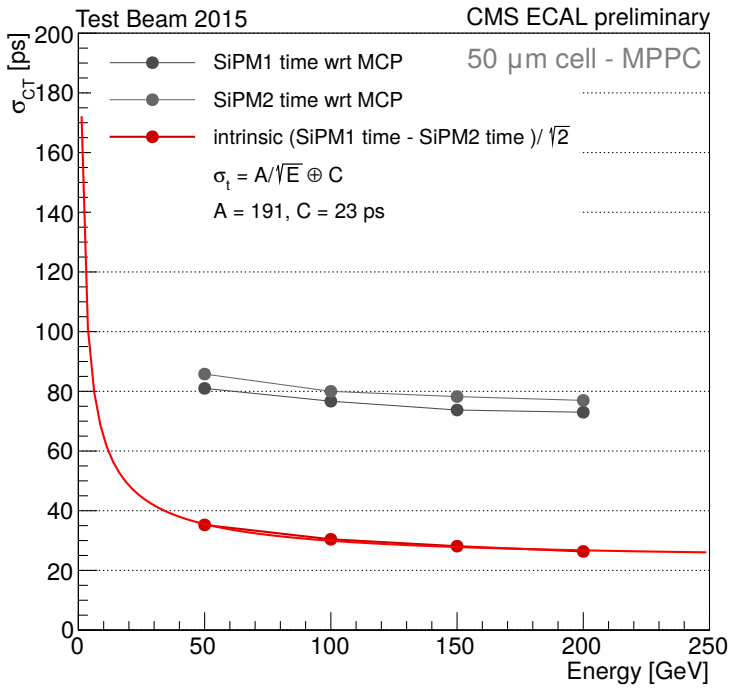

Figure 5.11: Front face light collection time performance. The times measured with the two SiPM arrays is compared to the MCP time (grey curves) and one to the other (red curve). SiPM time performance is comparable to the APDs one (red) but is affected by light emission fluctuations when comparing to an external reference (i.e. MCP).

5.5 Impact of timing on physics analysis at HL-LHC

The inclusion of per-particle time measurement provides benefits for various physics analyses that are part of the HL-LHC physics scope.

The time information, as explained at the beginning of the chapter, will improve the vertex reconstruction as well as the particle to vertex association, in particular the MIP time detector (MTD) will reduce the number of tracks wrongly assigned to the primary vertex (PV) of each bunch-crossing. In the context of the CMS technical proposal for HL-LHC the impact of timing on the objects reconstruction and identification has been studied together with the resulting gain for analysis that are part of the physics scope of HL-LHC. Improvements are found in many areas:

- pileup jet suppression: the number of pileup jets is reduced by 20% in the barrel and 40% in the endcaps while retaining full efficiency on signal jets like those produced in VBS events.
- Improved jet and E_T^{miss} resolution: the rate of events with $E_T^{miss} > 130$ GeV is reduced by 40% providing less background for SUSY and Dark matter searches.
- Thanks to a better primary and secondary vertex reconstruction standard b-tagging algorithms reach a performance comparable to that of zero pileup. The b-tagging improved performance translates into a direct gain for the measurement of the Higgs boson self coupling since the most sensitive channels are $HH \to b\bar{b}b\bar{b}$ and $HH \to b\bar{b}\gamma\gamma$.
- Lepton identification through a better resolution on the charged isolation defined as:
$$Iso_{ch} = \Sigma p_T$$
where the sum runs over all the tracks with $p_T > 0.7$ GeV and within a cone of radius $R = 0.3$ (Section 5.5.2).
- Reconstruction of the diphoton interaction vertex in $H \to \gamma\gamma$ events thanks to both the photon time provided by the ECAL and the vertex time from charged particles detected in the MTD. Search for long lived particles decaying in a photon and undetected particle will also profit from the precise identification of the primary and secondary vertex position.

In the following sections two of the reconstruction improvements outlined above are described in details: the muon charged isolation and diphoton vertexing. The time-aware event reconstruction and the implementation of the simulation used are first introduced in the next section.

5.5.1 MTD simulation and time-aware event reconstruction

The simulation used to assess the performance gain brought to the CMS HL-LHC physics program includes a modelling of the future CMS detector with the tracker acceptance extend to $|\eta| = 4$ and a muon system coverage up to $|\eta| = 2.8$. Although the MTD detector is simulated, the time of the charged particles is computed by applying a smearing of 30 ps to the simulation time recorded in the last tracker layer and by correcting for the time of flight known from the simulation. A time is associated to each track within the acceptance of the BTL and ETL, while for all other tracks the time is set to zero and an uncertainty of 150 ps is assigned to it (equal to time spread of the beamspot). The

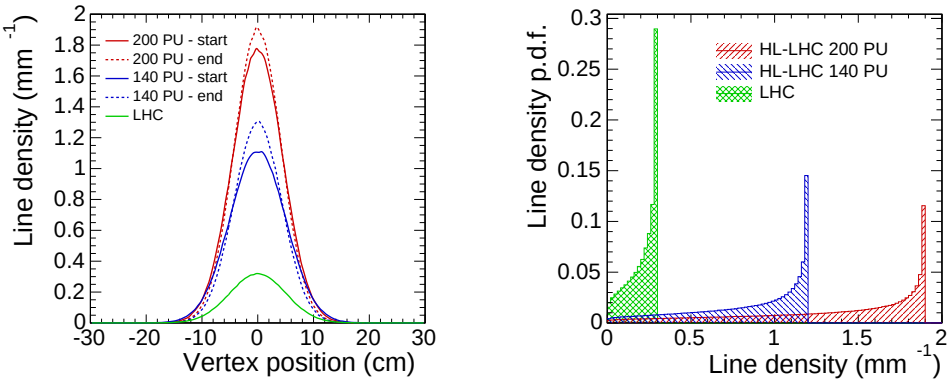

Figure 5.12: Spread of the vertices along the beam direction at LHC and HL-LHC with 140 and 200 pileup events. The solid (dashed) line refers to the start (end) of the LHC fill (left). Probability density function of the vertex density along the beam axis: the modes and the means of the three distributions are 0.3, 1.3, and 1.9 mm^{-1} and 0.2, 0.9, and 1.4 mm^{-1} (right).

vertex reconstruction in the tz-plane, i.e. in time and position along the beam line, is done using a time-aware extension of the deterministic annealing technique adopted in vertex reconstruction by the CMS experiment [66].

The method used to assign tracks to a primary vertex (PV) is based on the distance between the two. This is a common method within CMS, a typical selection requires $|\Delta z(track, PV)| < 1$ mm, which means that for collision closer than 1 mm the reconstructed tracks are considered as if they were originating from the same interaction. The time selection is introduced in a similar fashion by requiring $|\Delta t(track, PV)| < N \times \sigma_t$, where $\sigma_t = \sqrt{\sigma_t^{track2} + \sigma_t^{vertex2}}$ and $N = 3$ is chosen for the current study.

One of the benefits of the time-aware event reconstruction is to separate in time events not resolved by the tracker. Since the probability of vertex merging strongly depends on the density along the beam z-axis the results are presented as a function of the vertex line density. The vertex line density distributions for the current LHC beamspot and two possible HL-LHC scenarios are shown in Figure 5.12, the ultimate performance of the HL-LHC is expected to give a maximum line density of 1.9mm^{-1}. This scenario is the one simulated for the studies presented in the following sections, the beamspot distribution has a Gaussian shape both in z and t directions, with standard deviations of 4.2 cm and 150 ps.

5.5.2 Muon isolation with precision timing

As explained at the beginning of the chapter one of the goals of the HL-LHC is the precise measurement of the Higgs boson properties. The four muons final state is the purest decay mode from the experimental point of view as already demonstrated by the analysis that contributed to the first observation of the Higgs boson. Furthermore the direct decay of the Higgs boson in two muons is the only decay to second generation leptons that can be observed at HL-LHC.

The vertex merging occurring with Δz-based association criterion described in the previous section directly affects the discrimination power of isolation variables since tracks from an unrelated vertex are not excluded from the isolation cone of a particle coming

from the real hard interaction. This study focuses only on the charged component of the isolation since charged particles comprise the largest fraction of hadronic activity in $p-p$ collisions and therefore are the most important contribution to isolation sums in the context of identifying isolated leptons.

Signal muons are selected within a sample of prompt muons originated by a Z boson decay by geometrically matching the reconstructed muon to a generator-level muon. Non-prompt muons from semileptonic decays of heavy flavour hadrons in $t\bar{t}$ events are considered representative of non-isolated, background muons. Muons coming from the decay of the W boson produced by the top quark decay are rejected based on generator-level information and only muons matching a generator-level hadronic jet are retained.

The algorithm for the choice of the PV currently in use in CMS is inefficient at 200 pileup, for this reason the PV is chosen as reconstructed vertex closer to the simulated position of the hard interaction, this procedure is done independently for the collection of vertices reconstructed with and without the time information. This choice provide a fair comparison by decoupling the track-vertex association from the correct choice of the PV.

Muons are selected with a set of criteria based on the current CMS muon reconstruction and identification, with selection optimized for the HL-LHC conditions. Both prompt and non-prompt muons are required to have $|\eta| < 2.8$ (muon system acceptance), $p_T > 20$ GeV and a point-of-closest-approach to the primary vertex that is within 1 mm in the z-direction. In the case of the time-aware reconstruction an additional $|\Delta t(muon, vertex)| < 3 \times \sigma_t|$ is imposed. The $|\Delta t(muon, vertex)|$ is corrected for the muon time of flight.

The charged isolation (Ch_{iso}) is computed as the sum of the p_T of all tracks within a cone of radius $R = 0.3$ centered around the muon direction excluding the muon track itself. Only tracks with $p_T > 0.7$ GeV are considered in the sum. The isolation selection requirement is set on the relative charged isolation value Ch_{iso}/p_T^{muon}.

The Δz selection value is optimized by comparing the ROC curves for different selection values. The ROC (receiver operating characteristic) curve is obtained by plotting the efficiency for non-prompt muons ($\epsilon_{non-prompt}$) versus prompt muons (ϵ_{prompt}) for a spectrum of possible Ch_{iso}/p_T^{muon} thresholds. The 1 mm and 2 mm values are found to provide the best performances, as shown in Figure 5.13, both for barrel and endcap muons. The 1 mm selection is chosen as baseline for the study since it also provide the best performances for jets and E_T^{miss} studies. For Δz values below 1 mm the performance the selections are too tight and tracks coming from the PV are removed from the isolation computation, thus the rate of fake photons increases while the rate of prompt, isolated, photons is unchanged. Conversely wider Δz cuts (> 1 mm) increase the probability of including tracks from pile-up vertices in the isolation sum, leading to a worse discrimination power. The time information is included, as for the muon association to the PV, by applying a selection on the time difference between the vertex time (estimated by the 4D vertexing algorithm) and the track time measured by the timing detector $|\Delta t(track, vertex)|$ (corrected for the time of flight). The selection $|\Delta t(track, vertex)|3 \times \sigma_t|$ as for the muon track.

The comparison between the timing and no-timing scenario is shown in Figures 5.14 and highlight a clear benefit from the use of timing for working points with $\epsilon_{prompt} > 80\%$. The performance gain can be expressed either in terms of reduced non-prompt rate a constant prompt efficiency (bottom panels of Figures 5.14) or equivalently as prompt efficiency gain at constant non-prompt efficiency (right panels of Figures 5.14).

The results as a function of the vertex line density are reported in Figure 5.15 and show, as expected, a higher impact of the MTD for the high density bins. The use of

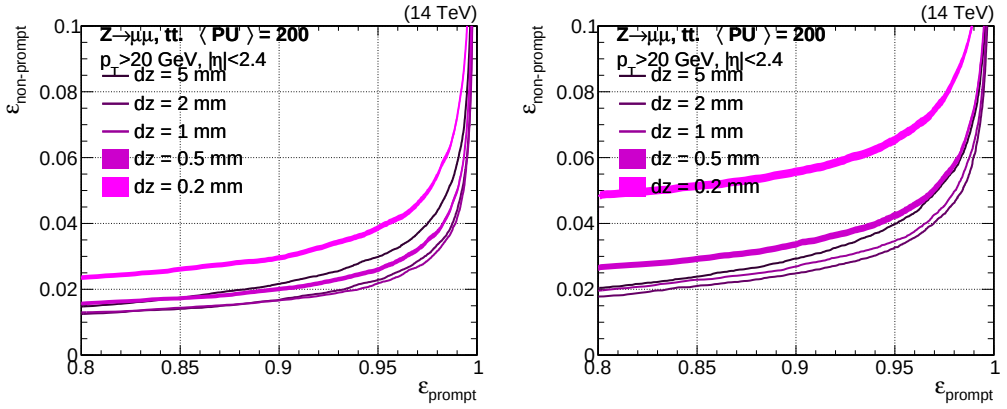

Figure 5.13: ROC curve comparison for different Δz selections. In both BTL (left) and ETL (right) acceptance regions the 1 and 2 mm selections provide the best performance

time in the Ch_{iso}/p_T^{muon} computation gives a 10% increase in the ϵ_{prompt} with a marginal deterioration of the non-prompt rejection.

Different MTD time resolution performances are compared in Figure 5.16: the gain on ϵ_{prompt} is retained even for a degraded detector performance of 50-70 ps, comparable to that expected at the end of the HL-LHC era.

The improvement on the charged isolation selection efficiency is projected onto the $H \to 4\mu$ analysis in terms of an increased signal acceptance and thus increased of equivalent integrated luminosity at a constant background rate. Both the BTL and ETL contribute significantly to the signal gain shown in Figure 5.17. The projection are for a charged isolation working point that provides $\epsilon_{prompt} = 90\%$ in the no-MTD case. The gain introduced by the use of timing is equivalent to a 20% increase in the signal over square-root of the background ratio.

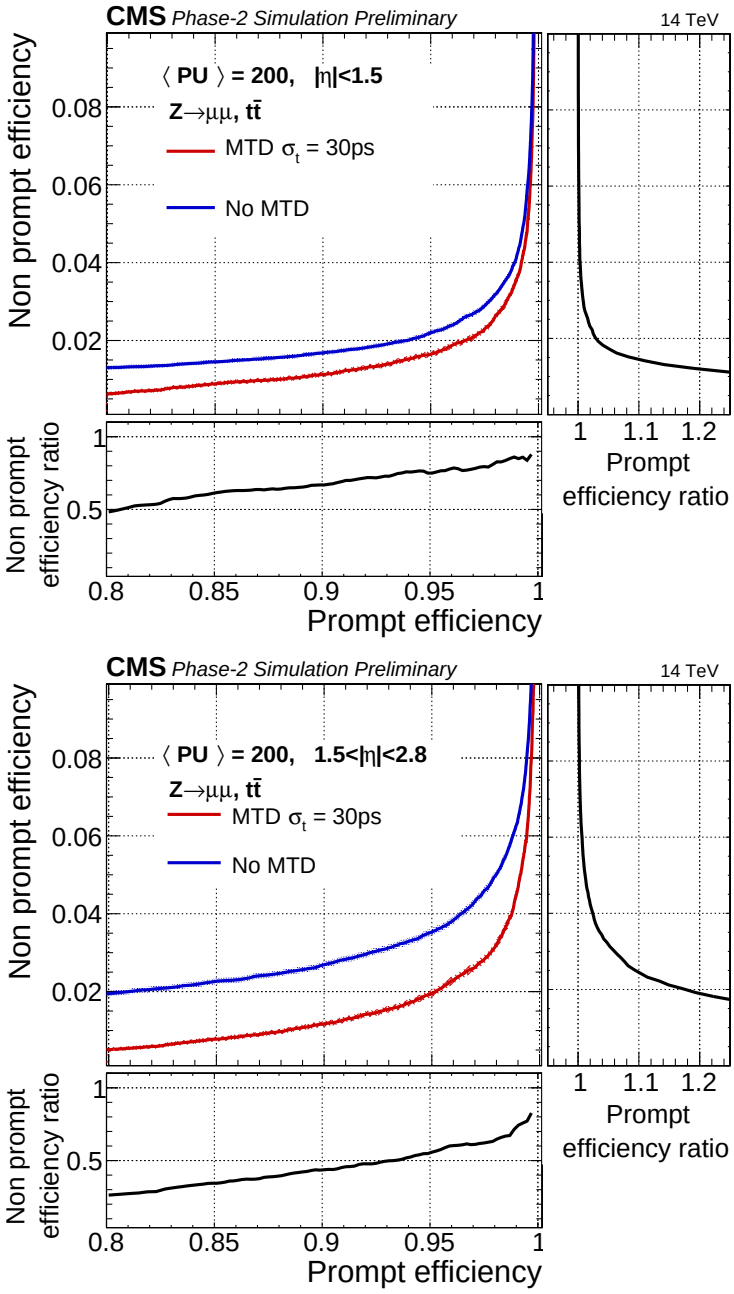

Figure 5.14: ROC curves calculated for a cut-off scan in relative charged isolation for muon candidates in the BTL (top) and ETL (bottom) acceptance.

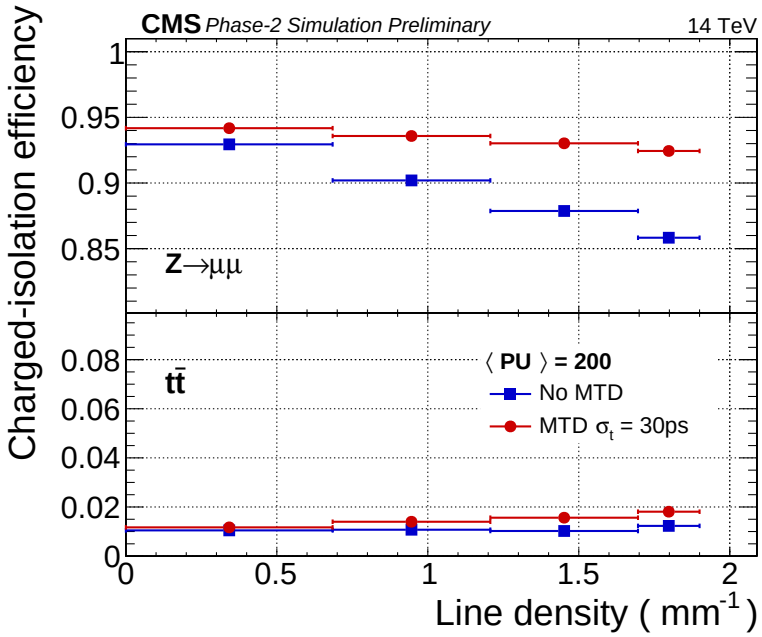

Figure 5.15: The efficiency for prompt and non-prompt muons as a function of the vertex density for a representative operating point selection value common to the MTD and no-MTD scenarios.

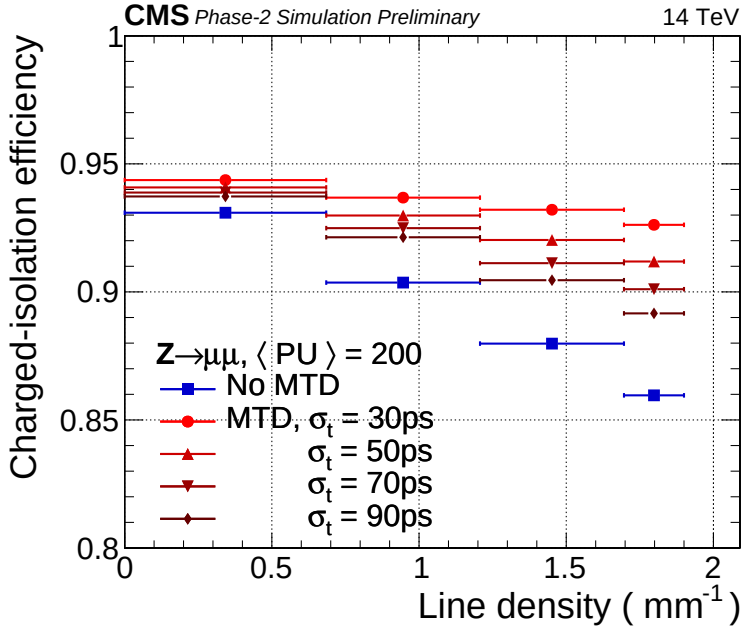

Figure 5.16: Muon efficiency for relative charged isolation cut-off of 0.05 for different time resolution assumptions, as a function of line density. The fake rate is approximately constant in all scenarios.

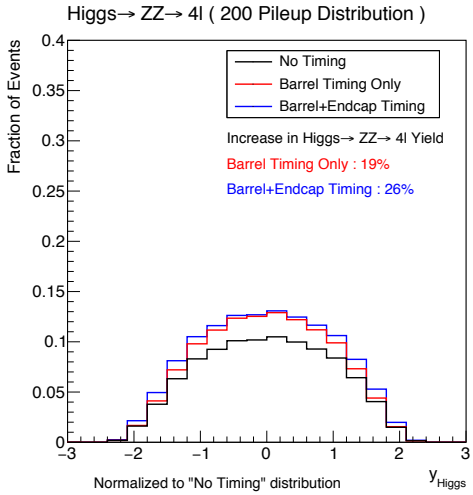

Figure 5.17: Projections for yield enhancement in $H \to ZZ \to 4\mu$ as a function of the Higgs boson rapidity. The distributions are normalized to the no-timing case.

5.5.3 Diphoton vertex identification

The clean diphoton signature is a prime tool to study the Higgs boson properties. The sensitivity of the measurement depends on the invariant mass resolution of the diphoton pair and on the quality of the photon identification. The mass resolution, as explained in Chapter 4, in the equivalent context of the search for BSM resonances, is subordinated to the precision on two measurements: the energy resolution of the ECAL and the precision on the angle between the two photons which in turn is related to the identification of the diphoton production vertex. If the longitudinal position of the diphoton vertex is known to better than about 10 mm, the opening angle resolution contributes negligibly to the diphoton mass resolution [47]. For the reasons detailed in the previous sections this channel will benefit from the improved acceptance for isolated objects and improved vertex identification capability provided by track and photon timing information.

In low pileup conditions such as those of the current LHC the diphoton vertex identification exploits the kinematic properties of the tracks associated with the reconstructed vertices and their correlation with the diphoton kinematics as explained in Section 4.4. For the H $\rightarrow\gamma\gamma$ decay vertex the identification efficiency if this method is less 80% at 30 pileup events, as shown in Figure 5.18.

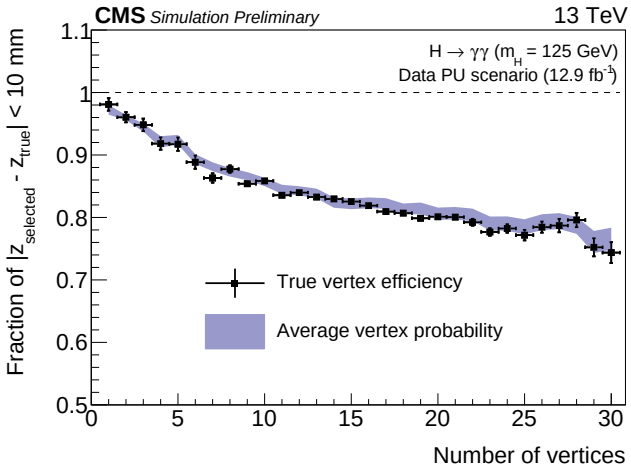

Figure 5.18: Efficiency for correct vertex assignment as a function of the number of reconstructed vertices in H $\rightarrow\gamma\gamma$ decays at a centre-of-mass energy of 13 TeV and for vertex multiplicities corresponding to LHC operations in 2016.

According to simulation, at 140 pileup events, the efficiency drops below 40% for H $\rightarrow\gamma\gamma$ events produced through gluon fusion (the main contribution to the total Higgs boson cross-section), and it degrades to about 30% at 200 pileup events. This efficiency loss can be mitigated by means of a precise measurement of the time of both photons, which enables the vertex position along the beam direction to be determined via triangulation. The vertex position is located with a precision better than 1 cm only for events in which the opening angle between the two photons is such that the η separation is more than 0.8. For events in which $|\Delta\eta| < 0.8$ the position resolution achieved through triangulation only is comparable to the beamspot size (Figure 5.19). For this sample, photon timing alone does not provide sufficient information to locate the H $\rightarrow\gamma\gamma$ decay vertex. The ability to correctly identify the vertex in events with a small pseudorapidity gap between the two photons is recovered by additionally requiring a triple coincidence between the photon time calculated at the location of each track-reconstructed vertex and

the vertex time.

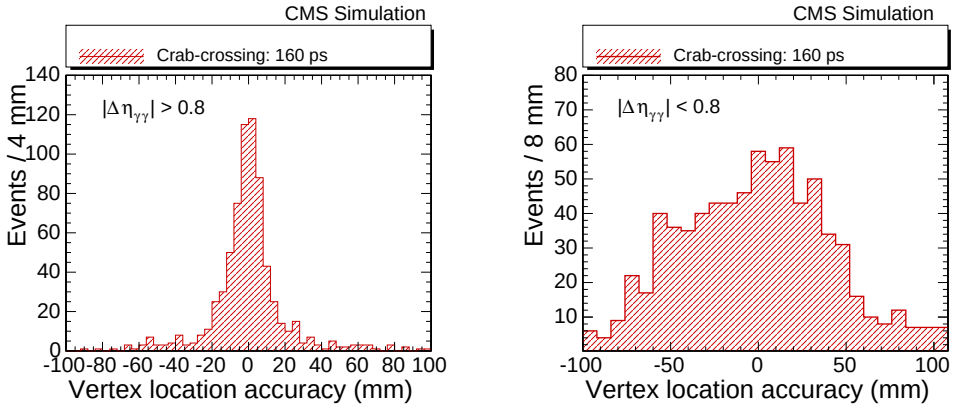

Figure 5.19: Distribution of the distance between the vertex reconstructed with time aware triangulation and the true vertex position along the beam direction, in H $\rightarrow\gamma\gamma$ events. Decay into photons with pseudorapidity gap of $|\Delta\eta| > 0.8$ and $|\Delta\eta| < 0.8$ are shown in the left and right panel respectively.

A quantitative measure of the compatibility of the photon pair with the space-time position of each reconstructed vertex is obtained from a χ^2 statistics defined as:

$$\chi^2(t_0, z_0) = \frac{(t_0 - t_{\gamma_1,vtx})^2}{\sigma^2_{t,\gamma_1} + \sigma^2_{t,vtx}} + \frac{(t_0 - t_{\gamma_2,vtx})^2}{\sigma^2_{t,\gamma_2} + \sigma^2_{t,vtx}} + \frac{z_0^2}{\sigma^2_{BS,z}} + \frac{2\rho \cdot (t_0 - t_{\gamma_1,vtx})(t_0 - t_{\gamma_2,vtx})}{\sigma^2_t + \sigma^2_{t,vtx}}$$

The simulation parameters differs slightly from the one described in the previous section: a 20 ps vertex time resolution is simulated by smearing the generator-level time instead of performing the full space-time vertex reconstruction described above. This is however comparable to the resolution achieved with the full simulation of the track timing. The ECAL time resolution is assumed to be 30 ps for every photon regardless of their p_T. This is in agreement with the beam test results reported in Section 5.4.1 given that only events in which the two photons have $p_T > 30$ GeV are considered in the analysis. The beamspot configuration is also different with a spread in time of 160 ps (RMS) and 5 cm along the z-axis and a mean number of pileup events of 140 instead of 200.

The χ^2 distributions for the true diphoton vertex, known from simulation, and for all the other vertices are shown in the left panel of Figure 5.20 (left). Only events with a $|\Delta\eta| < 0.8$ gap between the two photons are considered for the plot. The overlap of the distributions at low χ^2 indicates that there is a finite probability for a random pileup vertex to have a χ^2 lower than the true diphoton vertex. However by ranking the vertices accordingly to their respective χ^2 as in Figure 5.20 (right) it becomes clear that, in the 95% of the events, the real diphoton vertex lies among the first 10 for $|\Delta\eta| > 0.8$ and in the first 20 for $|\Delta\eta| < 0.8$. This effectively reduces the pileup to a level even lower than the current data-taking for which the kinematic based vertex selection has an 80% efficiency.

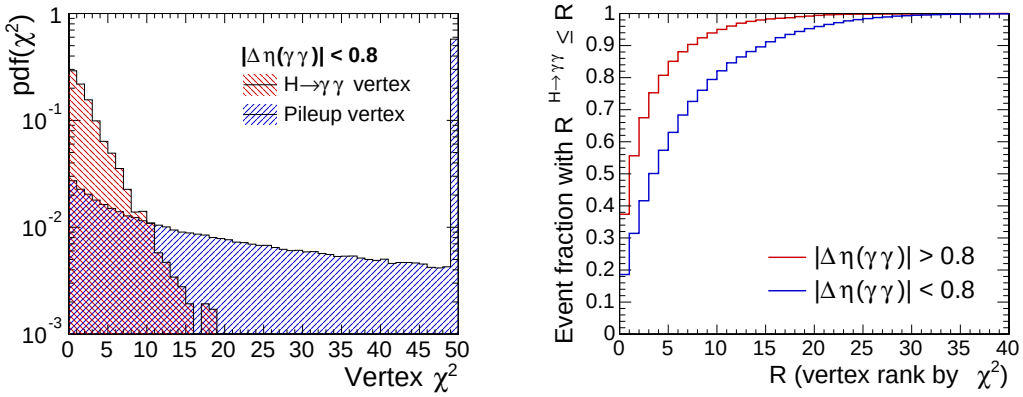

Figure 5.20: Distribution of the χ^2 (left) of the true H $\rightarrow\gamma\gamma$ (red) and pileup vertices (blue) for 30 ps time resolution in the calorimeters, 20 ps resolution in vertex timing, and a $|\Delta\eta| < 0.8$ between the two photons. Fraction of events in which the diphoton vertex has a rank equal or lower than the rank in the horizontal axis, for 140 pileup events (right).

5.6 Summary

The HL-LHC era will provide an unprecedented amount of data to the ATLAS and CMS experiments through a record instantaneous luminosity four times higher than the current LHC maximum. CMS is preparing an upgrade of its detector to match the radiation hardness requirements of HL-LHC and to fully exploit the larger dataset to perform precision measurements of rare standard model (SM) processes and extend the searches for new phenomena described by models beyond the SM.

The inclusion of the time information in the event reconstruction has been proved, through simulation studies, to provide a unique way to mitigate the deterioration of performance due to pileup and also open the possibility to measure observables otherwise inaccessible (mass of long lived SUSY particles). The same simulation studies underline the importance of an hermetic timing measurement charged particles.

During the past two years a series of beam tests have proven the timing capabilities of the existing ECAL barrel sensors and also those proposed for the implementation of the MTD (LYSO crystal with SiPM photo-detectors for the barrel and silicon sensors for the endcaps). All the technologies are capable of a resolution better than 30 ps and when combined into the CMS reconstruction they provide time measurement for charged particles, high energy photons and neutral hadrons (endcaps only).

Both the tests described above and examples of performance gain have been discussed in this chapter.

Chapter 6

Conclusions

The research activity of my three years long Ph.D. activity was carried out within the CMS experiment collaboration. The primary focus has been the search for BSM signatures in diphoton events with data of proton-proton collisions at 13 TeV of center-of-mass energy collected by the CMS experiment. The results obtained from the search for exotic spin-0 and spin-2 resonances improves the previous results from LHC experiments and set limits on the production of RS graviton excluding resonances up to 2 to 4 TeV depending on theory parameters.

An excellent photon energy resolution is required to achieved the best sensitivity to narrow resonances. Part of my work was devoted to the energy calibration of the CMS ECAL, the crucial component for measurement involving photons. The first energy calibration performed after the long LHC shutdown for the preparation of the 13 TeV run restored the same energy resolution achieved during the 8 TeV operation. I optimized one of the intercalibration methods which turned out to provide the best intercalibration precision among the three methods used. The same method was further developed during 2016 to establish a monitoring of the energy response evolution that combined with the laser monitoring system provides the stability needed for precise measurement in the context of the Higgs boson physics in the diphoton final state.

Final states with photons will remain a powerful tool to explore the Higgs sector through precise measurement of its properties and physics beyond the standard model also during the high luminosity phase of LHC (HL-LHC). The instantaneous luminosity of the HL-LHC will pose severe challenges to the performances of the physics analysis of CMS, due to the increased number of pileup events several observable (from diphoton vertex reconstruction to b-tagging and isolation) will provide less discrimination power between signal and background than they currently does.

CMS is planning a substantial upgrade of the detector for the HL-LHC phase including a new tracker system with extended coverage, a high granularity sampling calorimeter for the endcaps, extended muons acceptance and a Level-1 trigger system capable of recording events at 750 MHz (7.5 times the current rate). The addition of time information to the event reconstruction has been also considered lately as a way to mitigate the performance deterioration. From the simulation work presented in this document a clear benefit is brought to the muon identification and the diphoton vertex reconstruction, other improvements have been demonstrated and were briefly presented. All the studies underlines that only with time measurement for all charged particles it is possible to reconstruct the time of the hard interaction and thus fully exploit the time-aware reconstruction combining also the time measurement performed by the calorimeters. This requires the installation of a new detector with a resolution of about 30 ps for charged

particles with $p_T > 0.7$ GeV. I took part in several beam test aimed to establish the best technology for the implementation of such detector given the installation and operation constrains of the future CMS detector. The LYSO crystal coupled to SiPM proved to be an already mature technology with bout 30 ps time resolution on MIP suitable to be installed in the CMS barrel timing detector. Regarding the calorimetry timing beam test results shows that the $PbWO_4$ plus APD sensor already installed in CMS is capable of an excellent time resolution that with the future electronic will provide a precision of 20 ps for electrons and photons with energy above 20 GeV.

Bibliography

[1] Measurements of the Higgs boson production and decay rates and constraints on its couplings from a combined ATLAS and CMS analysis of the LHC pp collision data at $\sqrt{s} = 7$ and 8 TeV. Technical Report CMS-PAS-HIG-15-002. ATLAS-CONF-2015-044, CERN, Geneva, 2015. URL https://cds.cern.ch/record/2053103.

[2] tagkey1965471. 65 - on the angular momentum of a system of two photons. In D. TER HAAR, editor, *Collected Papers of L.D. Landau*, pages 471 – 473. Pergamon, 1965. ISBN 978-0-08-010586-4. doi: https://doi.org/10.1016/B978-0-08-010586-4.50070-5. URL https://www.sciencedirect.com/science/article/pii/B9780080105864500705.

[3] C. N. Yang. Selection rules for the dematerialization of a particle into two photons. *Phys. Rev.*, 77:242–245, Jan 1950. doi: 10.1103/PhysRev.77.242. URL https://link.aps.org/doi/10.1103/PhysRev.77.242.

[4] C. Patrignani and Particle Data Group. Review of particle physics. *Chinese Physics C*, 40(10):100001, 2016. URL http://stacks.iop.org/1674-1137/40/i=10/a=100001.

[5] F. Englert and R. Brout. Broken symmetry and the mass of gauge vector mesons. *Phys. Rev. Lett.*, 13:321–323, Aug 1964. doi: 10.1103/PhysRevLett.13.321. URL https://link.aps.org/doi/10.1103/PhysRevLett.13.321.

[6] Peter W. Higgs. Spontaneous symmetry breakdown without massless bosons. *Phys. Rev.*, 145:1156–1163, May 1966. doi: 10.1103/PhysRev.145.1156. URL https://link.aps.org/doi/10.1103/PhysRev.145.1156.

[7] H. Abramowicz et al. Combination of measurements of inclusive deep inelastic $e^{\pm}p$ scattering cross sections and QCD analysis of HERA data. *Eur. Phys. J.*, C75(12): 580, 2015. doi: 10.1140/epjc/s10052-015-3710-4.

[8] G. Altarelli and G. Parisi. Asymptotic freedom in parton language. *Nuclear Physics B*, 126(2):298 – 318, 1977. ISSN 0550-3213. doi: https://doi.org/10.1016/0550-3213(77)90384-4. URL http://www.sciencedirect.com/science/article/pii/0550321377903844.

[9] Vladimir Naumovich Gribov and L N Lipatov. Deep inelastic ep scattering in perturbation theory. *Sov. J. Nucl. Phys.*, 15(4):438–450, 1972. URL https://cds.cern.ch/record/427157.

[10] Yuri L. Dokshitzer. Calculation of the Structure Functions for Deep Inelastic Scattering and e+ e- Annihilation by Perturbation Theory in Quantum Chromodynamics. *Sov. Phys. JETP*, 46:641–653, 1977. [Zh. Eksp. Teor. Fiz.73,1216(1977)].

[11] Richard D. Ball, Valerio Bertone, Stefano Carrazza, Christopher S. Deans, Luigi Del Debbio, Stefano Forte, Alberto Guffanti, Nathan P. Hartland, José I. Latorre, Juan Rojo, and Maria Ubiali. Parton distributions for the lhc run ii. *Journal of High Energy Physics*, 2015(4):40, Apr 2015.

[12] Theodor Kaluza. On the Problem of Unity in Physics. *Sitzungsber. Preuss. Akad. Wiss. Berlin (Math. Phys.)*, 1921:966–972, 1921.

[13] Nima Arkani–Hamed, Savas Dimopoulos, and Gia Dvali. The hierarchy problem and new dimensions at a millimeter. *Physics Letters B*, 429(3):263 – 272, 1998. ISSN 0370-2693. doi: https://doi.org/10.1016/S0370-2693(98)00466-3. URL `http://www.sciencedirect.com/science/article/pii/S0370269398004663`.

[14] Lisa Randall and Raman Sundrum. Large mass hierarchy from a small extra dimension. *Phys. Rev. Lett.*, 83:3370–3373, Oct 1999. doi: 10.1103/PhysRevLett.83.3370. URL `https://link.aps.org/doi/10.1103/PhysRevLett.83.3370`.

[15] Alexandra Oliveira. Gravity particles from Warped Extra Dimensions, predictions for LHC. 2014.

[16] T. Aaltonen et al. Search for New Dielectron Resonances and Randall-Sundrum Gravitons at the Collider Detector at Fermilab. *Phys. Rev. Lett.*, 107:051801, 2011. doi: 10.1103/PhysRevLett.107.051801.

[17] Victor Mukhamedovich Abazov et al. Search for Randall-Sundrum gravitons in the dielectron and diphoton final states with 5.4 fb-1 of data from $p\bar{p}$ collisions at sqrt(s)=1.96 TeV. *Phys. Rev. Lett.*, 104:241802, 2010. doi: 10.1103/PhysRevLett.104.241802.

[18] Georges Aad et al. Search for high-mass diphoton resonances in pp collisions at $\sqrt{s} = 8$ TeV with the ATLAS detector. *Phys. Rev.*, D92(3):032004, 2015. doi: 10.1103/PhysRevD.92.032004.

[19] Search for High-Mass Diphoton Resonances in pp Collisions at sqrt(s)=8 TeV with the CMS Detector. Technical Report CMS-PAS-EXO-12-045, CERN, Geneva, 2015. URL `http://cds.cern.ch/record/2017806`.

[20] P S Bhupal Dev and Apostolos Pilaftsis. Maximally Symmetric Two Higgs Doublet Model with Natural Standard Model Alignment. *JHEP*, 12(arXiv:1408.3405. MAN-HEP-2014-10. CERN-PH-TH-2014-150):024. 26 p, Aug 2014. URL `http://cds.cern.ch/record/1750101`. Comments: 36 pages, 12 figures; corrected typos in Appendix B.

[21] Nathaniel Craig, Jamison Galloway, and Scott Thomas. Searching for Signs of the Second Higgs Doublet. 2013.

[22] T. Binoth, J.Ph. Guillet, E. Pilon, and M. Werlen. A full next-to-leading order study of direct photon pair production in hadronic collisions. *The European Physical Journal C - Particles and Fields*, 16(2):311–330, Aug 2000. ISSN 1434-6052. doi: 10.1007/s100520050024. URL `https://doi.org/10.1007/s100520050024`.

[23] *ATLAS: technical proposal for a general-purpose pp experiment at the Large Hadron Collider at CERN*. LHC Tech. Proposal. CERN, Geneva, 1994. URL `https://cds.cern.ch/record/290968`.

[24] *Technical proposal*. LHC Tech. Proposal. CERN, Geneva, 1994. URL `https://cds.cern.ch/record/290969`. Cover title : CMS, the Compact Muon Solenoid : technical proposal.

[25] *LHCb : Technical Proposal*. Tech. Proposal. CERN, Geneva, 1998. URL `https://cds.cern.ch/record/622031`.

[26] *ALICE: Technical proposal for a Large Ion collider Experiment at the CERN LHC*. LHC Tech. Proposal. CERN, Geneva, 1995. URL `https://cds.cern.ch/record/293391`.

[27] Tai Sakuma and Thomas McCauley. Detector and event visualization with sketchup at the cms experiment. *Journal of Physics: Conference Series*, 513(2):022032, 2014. URL `http://stacks.iop.org/1742-6596/513/i=2/a=022032`.

[28] The CMS Collaboration. Description and performance of track and primary-vertex reconstruction with the cms tracker. *Journal of Instrumentation*, 9(10):P10009, 2014. URL `http://stacks.iop.org/1748-0221/9/i=10/a=P10009`.

[29] CMS Collaboration. ECAL Technical Design Report (TDR) Figures from Chapter 1. CMS Collection., Dec 1997. URL `http://cds.cern.ch/record/1327662`.

[30] Jet energy scale and resolution performances with 13TeV data. Jun 2016. URL `https://cds.cern.ch/record/2160347`.

[31] *The CMS muon project: Technical Design Report*. Technical Design Report CMS. CERN, Geneva, 1997. URL `https://cds.cern.ch/record/343814`.

[32] Vardan Khachatryan et al. Performance of the CMS missing transverse momentum reconstruction in pp data at $\sqrt{s} = 8$ TeV. *JINST*, 10(02):P02006, 2015. doi: 10.1088/1748-0221/10/02/P02006.

[33] CMS Collaboration. Particle-flow reconstruction and global event description with the cms detector. *Journal of Instrumentation*, 12(10):P10003, 2017. URL `http://stacks.iop.org/1748-0221/12/i=10/a=P10003`.

[34] Vardan Khachatryan et al. Performance of Electron Reconstruction and Selection with the CMS Detector in Proton-Proton Collisions at $\sqrt{\text{s}} = 8$ TeV. *JINST*, 10(06):P06005, 2015. doi: 10.1088/1748-0221/10/06/P06005.

[35] Vardan Khachatryan et al. Performance of Photon Reconstruction and Identification with the CMS Detector in Proton-Proton Collisions at sqrt(s) = 8 TeV. *JINST*, 10 (08):P08010, 2015. doi: 10.1088/1748-0221/10/08/P08010.

[36] Serguei Chatrchyan et al. Energy Calibration and Resolution of the CMS Electromagnetic Calorimeter in *pp* Collisions at $\sqrt{s} = 7$ TeV. *JINST*, 8:P09009, 2013. doi: 10.1088/1748-0221/8/09/P09009. [JINST8,9009(2013)].

[37] *The CMS electromagnetic calorimeter project: Technical Design Report*. Technical Design Report CMS. CERN, Geneva, 1997. URL `https://cds.cern.ch/record/349375`.

[38] Emanuele Di Marco. CMS electromagnetic calorimeter calibration and timing performance during LHC Run I and future prospects. Technical Report CMS-CR-2014-410, CERN, Geneva, Nov 2014. URL `http://cds.cern.ch/record/1975982`.

[39] *The CMS electromagnetic calorimeter project: Technical Design Report.* Technical Design Report CMS. CERN, Geneva, 1997. URL `https://cds.cern.ch/record/349375`.

[40] ECAL Laser monitoring till end of 2016 and ECAL phi-symmetry. Feb 2017. URL `https://cds.cern.ch/record/2252725`.

[41] 2012 ECAL detector performance plots. Mar 2013. URL `http://cds.cern.ch/record/1528235`.

[42] CMS ECAL energy inter-calibration precision with 2015 data. May 2016. URL `https://cds.cern.ch/record/2114735`.

[43] 2015 ECAL detector performance plots. Dec 2015. URL `https://cds.cern.ch/record/2114735`.

[44] Performance of photon reconstruction and identification with the cms detector in proton-proton collisions at $\sqrt{}$ s = 8 tev. *Journal of Instrumentation*, 10(08):P08010, 2015. URL `http://stacks.iop.org/1748-0221/10/i=08/a=P08010`.

[45] Torbjörn Sjöstrand, Stefan Ask, Jesper R. Christiansen, Richard Corke, Nishita Desai, Philip Ilten, Stephen Mrenna, Stefan Prestel, Christine O. Rasmussen, and Peter Z. Skands. An Introduction to PYTHIA 8.2. *Comput. Phys. Commun.*, 191: 159–177, 2015. doi: 10.1016/j.cpc.2015.01.024.

[46]

[47] Observation of the diphoton decay of the Higgs boson and measurement of its properties. *Eur. Phys. J. C*, 74:3076, 2014. doi: 10.1140/epjc/s10052-014-3076-z.

[48] Glen Cowan, Kyle Cranmer, Eilam Gross, and Ofer Vitells. Asymptotic formulae for likelihood-based tests of new physics. *Eur.Phys.J.*, C71:1554, 2011. doi: 10.1140/epjc/s10052-011-1554-0,10.1140/epjc/s10052-013-2501-z.

[49] Morad Aaboud et al. Search for new phenomena in high-mass diphoton final states using 37 fb^{-1} of proton–proton collisions collected at $\sqrt{s} = 13$ TeV with the ATLAS detector. *Phys. Lett.*, B775:105–125, 2017. doi: 10.1016/j.physletb.2017.10.039.

[50] Vardan Khachatryan et al. Search for Resonant Production of High-Mass Photon Pairs in Proton-Proton Collisions at $\sqrt{s}$ =8 and 13 TeV. *Phys. Rev. Lett.*, 117(5): 051802, 2016. doi: 10.1103/PhysRevLett.117.051802.

[51] Vardan Khachatryan et al. Search for diphoton resonances in the mass range from 150 to 850 GeV in pp collisions at $\sqrt{s} = 8$ TeV. *Phys. Lett.*, B750:494–519, 2015. doi: 10.1016/j.physletb.2015.09.062.

[52] J Butler, D Contardo, M Klute, J Mans, L Silvestris, and Collaboration on behalf of the CMS. CMS Phase II Upgrade Scope Document. Technical Report CERN-LHCC-2015-019. LHCC-G-165, CERN, Geneva, Sep 2015. URL `https://cds.cern.ch/record/2055167`.

[53] K Klein. The Phase-2 Upgrade of the CMS Tracker. Technical Report CERN-LHCC-2017-009. CMS-TDR-014, CERN, Geneva, Jun 2017. URL `https://cds.cern.ch/record/2272264`.

[54] A. M. Magnan. HGCAL: a High-Granularity Calorimeter for the endcaps of CMS at HL-LHC. *JINST*, 12(01):C01042, 2017. doi: 10.1088/1748-0221/12/01/C01042.

[55] Carlos Lourenco. The Phase-2 Upgrade of the CMS Muon Detectors. Technical Report CERN-LHCC-2017-012. CMS-TDR-016, CERN, Geneva, Sep 2017. URL `https://cds.cern.ch/record/2283189`. This is a dummy submission, just to get the LHCC reference number.

[56] A. Alici. *Nuclear Instruments and Methods in Physics Research Section A: Accelerators, Spectrometers, Detectors and Associated Equipment*, 766(Supplement C):288 – 291, 2014. ISSN 0168-9002. doi: https://doi.org/10.1016/j.nima.2014.05.059. URL `http://www.sciencedirect.com/science/article/pii/S0168900214005993`. RICH2013 Proceedings of the Eighth International Workshop on Ring Imaging Cherenkov Detectors Shonan, Kanagawa, Japan, December 2-6, 2013.

[57] Klaus Fohl. TORCH — an Innovative High-Precision Time-of-Flight PID Detector for the LHCb Upgrade. (LHCb-PROC-2015-001. CERN-LHCb-PROC-2015-001): 7431227. 5 p, Jan 2015. URL `https://cds.cern.ch/record/1981563`.

[58] N. Akchurin et al. On the timing performance of thin planar silicon sensors. *Nucl. Instrum. Meth.*, A859:31–36, 2017. doi: 10.1016/j.nima.2017.03.065.

[59] N. Cartiglia, R. Arcidiacono, M. Baselga, R. Bellan, M. Boscardin, F. Cenna, G.F. Dalla Betta, P. Fernndez-Martnez, M. Ferrero, D. Flores, Z. Galloway, V. Greco, S. Hidalgo, F. Marchetto, V. Monaco, M. Obertino, L. Pancheri, G. Paternoster, A. Picerno, G. Pellegrini, D. Quirion, F. Ravera, R. Sacchi, H.F.-W. Sadrozinski, A. Seiden, A. Solano, and N. Spencer. Design optimization of ultra-fast silicon detectors. *Nuclear Instruments and Methods in Physics Research Section A: Accelerators, Spectrometers, Detectors and Associated Equipment*, 796(Supplement C):141 – 148, 2015. ISSN 0168-9002. doi: https://doi.org/10.1016/j.nima.2015.04.025. URL `http://www.sciencedirect.com/science/article/pii/S0168900215004982`. Proceedings of the 10th International Conference on Radiation Effects on Semiconductor Materials Detectors and Devices.

[60] Carlos Lourenco. The Phase-2 Upgrade of the CMS Barrel Calorimeters Technical Design Report. Technical Report CERN-LHCC-2017-011. CMS-TDR-015, CERN, Geneva, Sep 2017. URL `http://cds.cern.ch/record/2283187`. This is a dummy submission so that we get the LHCC reference number to be added in the cover page of the document. We will then proceed with the real submission. It would be good to have the submission workflow changed so as to avoid this extra complication.

[61] CMS Collaboration. Time reconstruction and performance of the cms electromagnetic calorimeter. *Journal of Instrumentation*, 5(03):T03011, 2010. URL `http://stacks.iop.org/1748-0221/5/i=03/a=T03011`.

[62] Daniele del Re. Timing performance of the CMS ECAL and prospects for the future. *J. Phys.: Conf. Ser.*, 587(1):012003. 6 p, 2015. URL `https://cds.cern.ch/record/2158942`.

[63] L. Brianza et al. Response of microchannel plates to single particles and to electromagnetic showers. *Nucl. Instrum. Meth.*, A797:216–221, 2015. doi: 10.1016/j.nima.2015.06.057.

[64] A. Yu Barnyakov et al. Response of microchannel plates in ionization mode to single particles and electromagnetic showers. *Nucl. Instrum. Meth.*, A879:6–12, 2018. doi: 10.1016/j.nima.2017.10.002.

[65] F Anghinolfi, P Jarron, A N Martemyanov, E Usenko, Horst Wenninger, M C S Williams, and A Zichichi. NINO: An ultra-fast and low-power front-end amplifier/discriminator ASIC designed for the multigap resistive plate chamber. *Nucl. Instrum. Methods Phys. Res., A*, 533:183–187, 2004. URL `http://cds.cern.ch/record/818554`.

[66] Serguei Chatrchyan et al. Description and performance of track and primary-vertex reconstruction with the CMS tracker. *JINST*, 9:P10009, 2014. doi: 10.1088/1748-0221/9/10/P10009.